DCB ESTIMATION WITH NEQUICK IONOSPHERIC MODELS FOR GNSS

PEDRO MIGUEL DA SILVA PINTO

MESTRADO EM DETEÇÃO REMOTA

DEPARTAMENTO DE GEOCIÊNCIAS E ORDENAMENTO DO TERRITÓRIO

Orientador

DALMIRO MAIA, Doutor, Faculdade de Ciências da Universidade do Porto

Coorientador

LUÍSA BASTOS, Doutora, Faculdade de Ciências da Universidade do Porto

Todas as correções determinadas

pelo júri, e só essas, foram efetuadas.

O Presidente do Júri,

Porto, _____/_____/_____

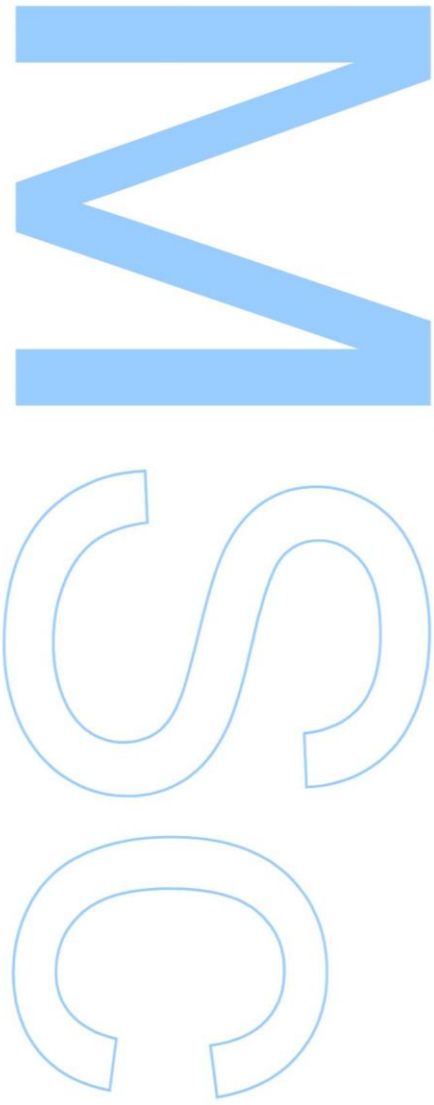

RESUMO

Os sistemas globais de navegação por satélite (*GNSS*) tem desempenhado ao longo das duas últimas décadas um papel preponderante nos estudos relacionados com a ionosfera. No entanto, para se obterem observações fiáveis com base nos *GNSS* é necessário estimar com algum rigor os atrasos instrumentais (*DCBs*) que afetam aquelas observações. Esses atrasos, ou, enviesamentos diferencias de código (*DCBs*), como geralmente são conhecidos, são erros sistemáticos, ou enviesamentos das observações geradas por dois códigos em frequências distintas (ou frequências iguais, mas com códigos diferentes), que impedem a medição explícita do conteúdo total de eletrões (*TEC*) presentes na ionosfera.

Formalmente, os *DCBs,* são atrasos temporais decorrentes da própria instrumentação dos satélites e recetores que necessitam de ser medidos e subtraídos às observações para efeitos de deteção, monitorização e mesmo previsão da ionosfera. Portanto, conhecer bem os *DCBs* que afetam satélites e recetores é vital para a medição rigorosa da ionosfera, apesar de, no caso dos satélites, isso não ser de difícil acesso (uma vez que são regularmente transmitidos na mensagem de navegação), já nos recetores, necessitam regularmente de ser estimados, pois, em geral, não são conhecidos, salvo em algumas estações de referência.

Ou seja, se alguém pretende conhecer com algum grau de exatidão o *DCB* do seu recetor, necessita de aplicar um modelo matemático complexo, ou, ainda, comparar diretamente o seu recetor com um recetor de referência, bem calibrado colocado lado-a-lado. A última opção, porém, é relativamente onerosa, uma vez que exige equipamento e mão-de-obra especializada normalmente indisponíveis, enquanto, na primeira, será sempre de difícil execução, mesmo para o utilizador mais dedicado.

Assim sendo, na tentativa de encontrar uma abordagem relativamente simples para esta matéria, desenvolveu-se uma ferramenta para a estimativa dos *DCBs* dos recetores, com recurso a modelos de previsão da ionosfera (*NeQuick-G*) de última geração, os quais combinados com observações de dupla frequência da portadora e código, permitem a estimativa simultânea da ionosfera e do *DCB* de um recetor que depois será usado como offset de referência, a deduzir na estimativa dos *DCBs* de outros recetores, que seguiram a mesma estratégia de ajustamento.

Em suma, tendo por base os resultados alcançados para a metodologia desenvolvida, foi possível obter um erro de calibração médio para os *DCB* dos recetores, nas frequências GPS L_1 e L_2 de -1.07 ± 0.075 *TECU* (-0.37 ± 0.026 ns).

ABSTRACT

During the last two decades, *GNSS* has become a very important tool for ionospheric studies. However, it is necessary to perform a careful estimation of the instrumental delays affecting *GNSS* observations (*DCBs*) to acquire reliable ionospheric data. Differential Code Biases (*DCBs*) are systematic errors, or biases, between two *GNSS* code observations at different frequencies (or at the same), that prevent explicit measurement of the ionospheric Total Electron Content (*TEC*).

Formally *DCBs* are time delays occurring within the satellite and receiver instrumental hardware, that must be accurately measured and deducted from the observations for detection, monitoring and even prediction of ionospheric effects. Hence, to precisely measure ionospheric activity it is vital to know *DCBs* from the receiver and satellites, which is usually not a problem, in the latter case (since they are routinely broadcast in the navigation message), while in the former, these values generally need to be estimated, since they are not available with exception of some reference stations.

Typically, if one wants to know his receiver *DCB* with some degree of accuracy, it must employ a complex mathematical model, or, even, to directly compare his receiver against a well-calibrated reference receiver positioned side-by-side. The latter strategy is rather costly, since it demands the availability of specialized equipment and human resources, usually not available, while the former, is hard to implement even for most dedicated user.

In this way, by attempting the exploration of a simpler solution to address this matter, a tool for receiver *DCB* estimation was developed, resorting to state-of-the-art empirical models for ionosphere prediction (*NeQuick-G*), that combined with dual frequency carrier and code observations for simultaneous estimation of ionosphere and receiver *DCB* reference offset, can be used for calibration of other receiver *DCBs*, by adopting the same adjustment strategy deducted off the reference offset.

Hence, according to results achieved by the developed methodology, it was possible to obtain a mean calibration error for receiver *DCB* estimation at *GPS* legacy L_1 and L_2 frequencies of -1.07 ± 0.075 TECU (-0.37 ± 0.026 ns).

KEY WORDS

Differential Code Bias;

Receiver Calibration;

Receiver DCB;

NeQuick-G;

Ionospheric Models;

Ionospheric Maps;

Total Electron Content;

GNSS;

TABLE OF CONTENTS

LIST OF TABLES

LIST OF FIGURES

ABREVIATIONS LIST

Az	Effective Ionisation Level	**K_{ji}**	Interfrequency bias between code instrumental delays at frequencies i and j
B	Geomagnetic Field	**LEO**	Low Earth Observation
BI	Ionospheric Ambiguity term	**L_f**	Carrier Phase of frequency f
bi	Ionospheric Bias	**LT**	Local Time
C/A	Coarse/acquisition	**MEO**	Middle Earth Orbit
CAS	Chinese Academy of Sciences, Beijing, CHN;	**MF**	Mapping function
CCL	Carrier to Code Levelling	**n**	Ionospheric Index of Refraction
CDMA	Code Division Multiple Access	**Ne**	Electron Density
CME	Coronal Mass Ejection	**NRCan**	Natural Resources Canada, Ottawa, CAN;
CODE	Center for Orbit Determination in Europe, Bern, CHE;	**P**	Pseudorange
DCB	Differential Code Bias	**POLY**	Polynomial Function
E	Elevation	**PPP**	Precise Point Positioning
eI	Electrons	**PRN**	Pseudo-Random Noise
ESA / ESOC	European Space Agency / European Space Operations Centre, Darmstadt, DEU;	**rcv-sat**	receiver to satellite
f_0	Critical Frequency	**rDCB**	Receiver Differential Code Bias
$F_{10.7}$	Ottawa 10.7 cm Solar Radio Flux	**RMSE**	Root Mean Square Error
FDMA	Frequency Division Multiple Access	**Rz**	Zurich Sunspot Number
FOC	Full operational capability	**sDCB**	Satellite Differential Code Bias
GCS	Ground Control Segment	**sfu**	Solar Flux Units
GEO	Geostationary Orbit	**SH**	Spherical Harmonic
GEONET	*GPS Earth Observation Network*	**SLM**	Single Layer Model
GIM	Global Ionospheric Map	**SOW**	Seconds Of the Week
GLONASS	*Global'naya Navigatsionnaya Sputnikovaya Sistema),*	**SS**	Space Segment
GNSS	Global Navigation Satellite System	**STD**	Standard Deviation
GPS	Global Positioning System	**STEC**	Slant Total Electron Content
GTSF	Generalized Trigonometric Series Function	**TEC**	Total Electron Content
I	Ionospheric Delay	**TECU**	Total Electron Content Unit
IAACs	Ionospheric Associate Analysis Centers	**UPC**	Universitat Politècnica de Catalunya, Barcelona, ESP;
ICA	Ionospheric Delay Correction Algorithm	**Usg**	User Segment
IGRF	International Geomagnetic Reference Field	**UTC**	Coordinated Universal Time
IGS	The International GNSS Service (IGS)	**VTEC**	Vertical Total Electron Content
IGSO	Inclined Geosynchronous Orbit	**WHU**	Wuhan University, Wuhan, CHN.
Iono-Mod	Ionospheric Model	**XUV**	X-rays to Extreme Ultraviolet
Iono-WG	Working Group on Ionosphere (Iono-WG)	**θ**	Geodetic Latitude
IPP	Ionospheric Pierce Point	**Θ**	Geomagnetic latitude
IR	Infrared	**θs**	Solar-geomagnetic latitude
IRI	International Reference Ionosphere	**λ**	wavelength
JPL	Jet Propulsion Laboratory,NASA, Washington, DC, USA;	**ϕ**	Geodetic Longitude
K	Code instrumental delay	**ϕs**	Solar-geomagnetic longitude

1. INTRODUCTION

Ionospheric space weather effects can adversely degrade the performance of radio systems in communication, space-based navigation, and remote sensing. Hence, navigation signals transmitted by Global Navigation Satellite Systems (*GNSS*) - such as *GPS* or the European system *Galileo* - travelling through the ionosphere are delayed, refracted, and diffracted by highly variable ionospheric plasma (ESA, 2021). Thus, to mitigate the ionospheric impact in several systems (safety of life, positioning, navigation, and timing applications) and infrastructures (electrical power grids, communications, earth observation, etc.), *GNSS* signals can effectively be used to detect, monitor, and predict ionospheric effects and variability. The downside, however, is that besides dual frequency *GNSS* measurements, today easily available in highly accurate and low cost *GNSS* receivers, it is vital to know the differential instrumental delay biases (*DCBs*) of both satellites and receivers before any accurate estimate of the absolute ionospheric *TEC* can be acquired.

Differential Code Biases (*DCBs*) are systematic errors, or biases, between two *GNSS* code observations at the same or different frequencies. They occur within the satellite and receiver instrumental hardware and need to be accounted for, since the time of the satellite clock, is not equal to the signal emission time, (to be measured at the satellite antenna phase center and thus including the time for signal generation, demodulation, up conversion, and transmission to the satellite antenna phase center), and neither the time of the received signal, is equal to the reception time, linked to the internal receiver clock, since the travel time or time delay, from the receiver antenna phase center to signal acquisition, demodulation and tracking (at receivers clock) must be deducted from the reception time.

Thus, DCBs are a non–negligible error source for all precise *GNSS* applications and ionospheric studies using code observation data and, are strictly dependent on frequencies, signal type, receiver tracking technologies and on the *GNSS* tracked by the receiver (Dach et al., 2018).

1.1. MOTIVATION

The most accurate method to determine receiver Differential Code Bias (*rDCB)* in Global Navigation Satellite Systems (*GNSS)* is to directly measure the hardware delays using a *GNSS* signal simulator. With this method the *DCB* estimation accuracy can reach 0.1 TECU (Dyrud et al., 2008). However, it requires special equipment to frequently calibrate every receiver in the network, which is not convenient for routing *GNSS* ionosphere monitoring (Kao et al., 2013), as *DCBs* change systematically (Yasyukevich et al., 2015) and affect the determination of the absolute *TEC*. Consequently, *rDCB* estimation is still an open topic, for accurate and continuous ionospheric data retrieval.

In this sense, intending to improve the management of cost and time consuming allocations of equipment and human resources for *rDCB* calibrations and thus ionosphere monitoring, a remote assessing tool based on reference receiver offset estimation, according to an adjustment strategy of simultaneous *TEC* and *DCB* retrieval, using *NeQuick-G* ionospheric models, is presented and proposed.

1.2. OBJECTIVE

The objective is to find if the methodology given by the difference of several *rDCB* results against a reference *rDCB,* estimated using the same adjustment strategy, can effectively be used to calibrate other receivers and monitor their changes. If the calibration results turn out to be satisfactory, then further studies with a wider range of stations and ionospheric conditions, should be considered to prove its adequacy or not. In case of adequacy, ionosphere researchers or common users, with dual frequency receivers and several operational conditions (as season of the year, solar cycle and latitudinal region), can easily calibrate their receivers (as long they have access to a well-know and calibrated reference receiver) and measure, monitor and produce ionospheric related data.

It must be pointed out, however, that the present research for the suitable adjustment strategy to apply in the calibration process, was entirely based on a single reference station analysis, since it was the only dataset available for the development of the best adjustment strategy, which was later applied to an undisclosed number of stations for evaluation of the procedure accuracy to predict the true *DCB* of the other stations, based on a reference offset and equal adjustment strategy.

1.3. SUMMARY

In the first part of the present work, the ionosphere development since its historical discover, measurements, models, predictions, and disturbances will be described. Then after looking to the complex physical phenomena occurring at the ionospheric layers, impacting communications, surveillance and navigation systems on Earth, several models and sensors will be mentioned to measure/monitor the ionosphere and its disturbances. At the core of these sensors are the *GNSS* (passive sensors) that introduced a significative advance on ionospheric research, based on the observables that enabled researchers and common users to access the *L-band* radar section and estimate the ionospheric effects, affecting different radio modulated signals.

As such, from simple to complex strategies to estimate *TEC* were developed to help the single-frequency receivers improve their position, navigation, and timing as to inspire researchers to better monitor and predict the ionosphere, even today. A plethora of spatial and mathematical models were developed and combined to improve the estimation of the ionosphere impact on different *GNSS* signals and to estimate instrumental *DCBs.* Accordingly, the capabilities of *NeQuick-G* empirical models will also be proposed

as an additional strategy for simultaneous ionosphere and receiver DCB estimation, using combined dual frequency carrier and code observations.

In the meantime, before applying the proposed procedure to real data, a series of tests are conducted to exploit and better understand how *NeQuick-G Az* models relate with *TEC* during different times of the year and day, to describe and quantify how single layer model mapping function affects the conversion from Slant *TEC* (*STEC*) to Vertical *TEC* (*VTEC*), and how significative are the error results for the developed $\min[\chi^2(t)]$ adjustment at different times of day, using simulated biased data.

At the last stage of the research, the results achieved for the reference receiver (Furnas) will be discussed along with two different time adjustment strategies and several elevation masks for mean day-to-day variation of the *rDCB* and *Az* model estimation, *rDCB* and *Az* model intra-day variation, *rDCB* and *Az* model adjustment during quiet and active days, estimated *Az* daily mean *VTEC* results against reference *VTEC* from Global Ionospheric Maps (*GIMs*) and finally, the calibration phase for the undisclosed testing stations (Flores, Terceira and Funchal) evaluation of the mean error calibration accuracy and precision.

The conclusions with the accuracy of the procedure results herein achieved, against reference accuracy values, closes this dissertation, and provides clues for further research and support of future applications.

2. THE ATMOSPHERE

Earth's atmosphere is the indispensable for the protection and survival of life on Earth. With advances in space technologies, human activities are now evolving into the upper atmosphere and space, and therefore, monitoring and study Earth's atmosphere, as the space environment, have become an international hot topic (Jin et al., 2019). According to its ionized characteristics, Earth's atmosphere can be divided into two major parts, i.e., the ionosphere and neutral atmosphere.

2.1. THE NEUTRAL ATMOSPHERE

The neutral atmosphere is that part of the atmosphere that is electrically neutral and stretches from the ground level up to a height of 50 km and beyond (Fig. 1). It is colloquially known as the air. Air is made up of nitrogen (*N*), oxygen (*O*), carbon dioxide (CO_2), as well as some other atoms and molecules including water vapor. With the inclusion of water vapor in the medium, will then refer to it as moist air.

The refractive index (n) of a parcel of moist air is a function of its temperature (T), the partial pressures (P_d) of the dry constituents (N, O, CO_2 etc.) and the partial pressure (e) of the water vapor $n = n(T, P_d, e)$. Essentially, air is a nondispersive medium, with n independent of frequency throughout most of the radio spectrum and including the frequencies used by all *GNSS*.

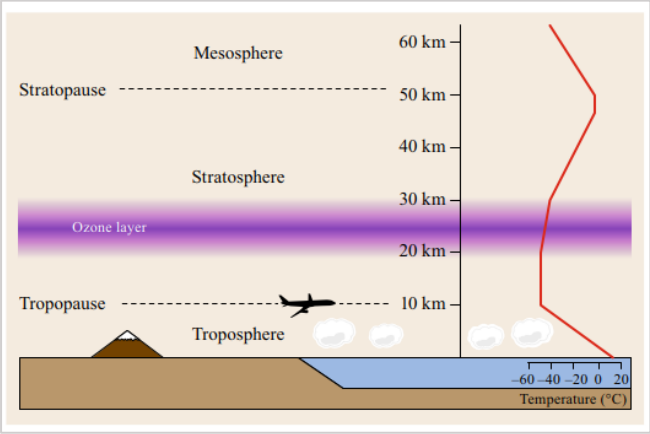

Fig. 1 – The troposphere is the lowest layer of Earth's atmosphere. The layer up is the stratosphere, followed by the mesosphere. Distinction between the layers is made with the vertical temperature. (Hobiger and Jakowski, 2017).

Since the bulk of the neutral atmospheric effect occurs in the lowest most part of the atmosphere – the troposphere – the effect is then often termed as tropospheric propagation delay (Langley et al., 2017).

2.2. THE IONOSPHERIC MEDIUM

The ionospheric layer discovery, started with the need to find an explanation for *Marconi's* demonstration of the crossing of the Atlantic with a radio wave transmission, from England to Canada in 1901. Kennelly (1902) and Heaviside (1902) at the time, independently suggested the event could be explained by possible reflection of waves in an ionized layer, which later was confirmed by Appleton and Barnett (1925), during an experiment with radio waves that proved its existence and height (Materassi et al., 2020).

Historically, the ionospheric theory, links solar photons with the Earth's neutral gases to yield a plasma population capable of being studied using ground-based instrumentation (Materassi et al., 2020). The flux of solar photons versus wavelength (called "*irradiance*") ranging from *X-rays* (*<~10 nm*) to extreme ultraviolet (*<~120 nm*) (collectively called *XUV* radiation), penetrates to different heights in the upper atmosphere to ionize the primary gases N_2, O_2, and *O,* and produce ionospheric plasma (with variable densities of free electrons (N_e) and ions, that increase with the distance from the Earth surface, in a non-uniformly way) (Fig. 2). Cosmic rays and energetic particles originating from the solar wind, may also contribute to the ionospheric ionization. Notably since the energy of solar radiation in the visible *(V)* and infrared *(IR)* wavelength are too low to ionize the neutral gas, they can therefore reach the Earth's surface (Hobiger and Jakowski, 2017).

The fact solar irradiance components reached different altitudes, led researchers to describe the ionosphere vertical structure as a series of "layers" (*D*, *E*, *F1*, and *F2*) produced at different photon penetration heights varying in altitude (Fig. 3) and in latitude, from the polar cap to the equator, according to a series of zones ordered by the solar zenith angles and the magnetic field characteristics, along the North-South meridians (Fig. 4) (Mendillo, 2020).

In this sense, the ionosphere became to be known as the ionized part of the Earth's atmosphere ranging from around 50 km up to about 1 000 km height (Hobiger and Jakowski, 2017).

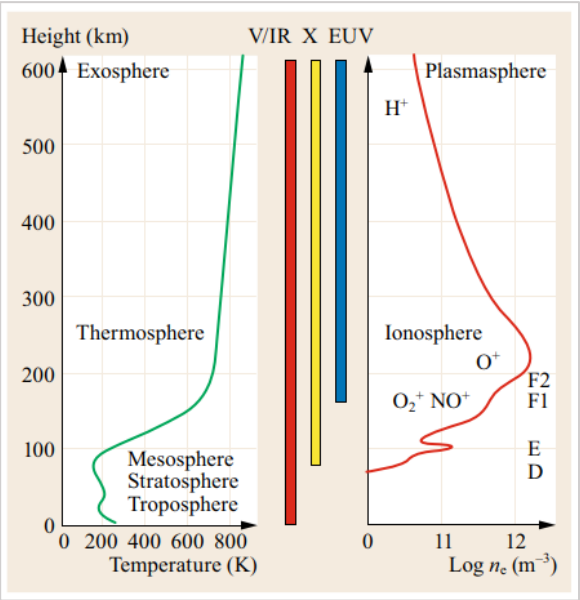

Fig. 2 – Electron density (N_e) vertical structure of the ionosphere (right) in comparison with the neutral atmosphere temperature (left) and solar radiation penetration depths (middle) (Hobiger and Jakowski, 2017) [300 K (26.85ºC); 800 K (526.85ºC)].

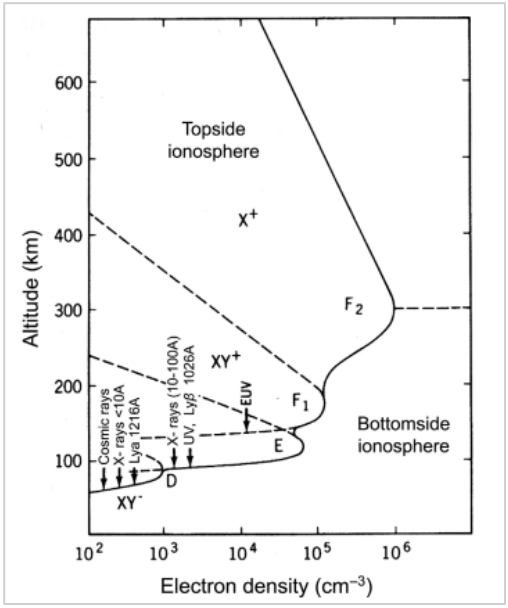

Fig. 3 – Layers of the Earth's ionosphere according to solar radiation and cosmic rays' penetration in the atmosphere. Notice that the separation between the bottom-side and topside of the ionosphere is defined by the peak of the F2 layer roughly at 300 – 350 km height (Bauer and Lammer, 2004).

2.3. THE DEVELOPMENT OF IONOSPHERE EMPIRICAL MODELS

Certainly the electron density *(N_e)* variable is the most important parameter from the applications perspective that governs all the effects on radio signals (Bust and Mitchell, 2008). The first attempt to define a vertical profile of the N_e up to the peak of the *F2* layer (Fig. 3), goes back to Appleton and Beynon (1947), when they introduced the concept of one *"parabolic"* N_e layer, according to the critical frequency *(f_0)* of the layer scaled from an ionogram and, its height and semi-thickness, scaled from computed values (Radicella and Nava, 2020).

Later in the *70's*, based on around 50 000 ionograms of the *Alouette sat* topside ionosonde, Llewellyn and Bent (1973), designed the first empirical model of the ionospheric N_e profile for trans-ionospheric radio propagation, by which Klobuchar (1987) later resort to develop the Ionospheric delay Correction Algorithm *(ICA)* still in use today by the Global Positioning System *(GPS)* for ionospheric *VTEC* estimation.

After, Giovanni and Radicella (1990) introduced a new model to describe the N_e vertical profile up to the *F2* layer peak, using a combination of three *Epstein* layers that uninterruptedly improved in the subsequent years by Radicella et al. (1995), Hochegger et al. (2000), Radicella and Leitinger (2001), and Nava et al. (2008), until acquiring the capability to estimate both vertical and slant N_e profiles below and above the *F2* layer peak (thus, the respective integrated *TEC*) for any specified path and location.

Although the empirical models mentioned so far was strictly oriented for ionospheric and trans-ionospheric radio propagation purposes, parallelly developed and still object of continuous improvement is the International Reference Ionosphere *(IRI)* (Rawer et al., 1978), which generates a climatological description for the N_e, electron temperature, ion temperature and ion composition, from 50 to 2 000 km height and includes, also the *VTEC* calculation, besides other important physical components (details in (Bilitza et al., 2017) and (Radicella and Nava, 2020)).

2.4. LATITUDINAL REGIONS OF THE IONOSPHERE

The classical latitudinal regions for the ionosphere are the high-latitude, mid-latitude and equatorial regions (Fig. 4). The equatorial regions are characterized with the highest values for the peak-electron density that can move as far to the geomagnetic latitudes of *10°* to *20°,* often termed as equatorial anomalies, due to its high concentration of electrons (Komjathy, 1997). In turn, the mid-latitude is the least variable and undisturbed among the different regions, whereas at the high-latitudes, besides the photon-ionization, collisional ionization tend to occur, causing local enhancements in the electron concentration associated with auroral activity (Komjathy, 1997) (details about these and other physical phenomena occurring at this regions, can be found for instance in Materassi et al. (2020)).

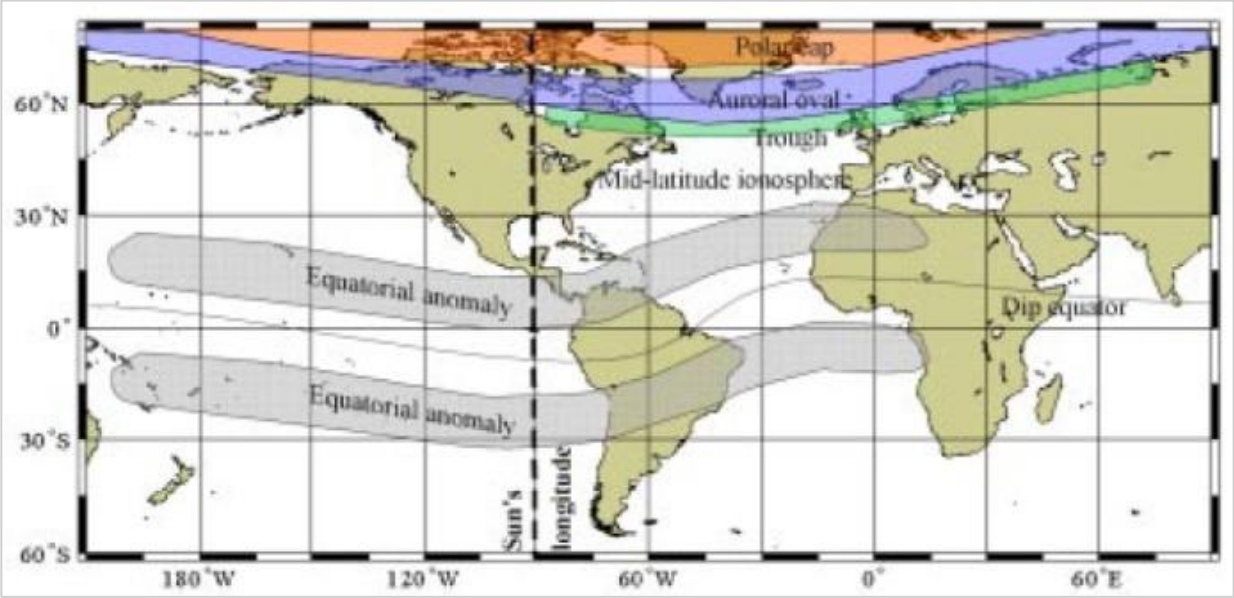

Fig. 4 – Major ionospheric latitudinal regions (Komjathy, 1997).

2.5. IONOSPHERIC DISTURBANCES

Solar disturbances or geomagnetic field disturbances, directly or indirectly associated with the events on the sun can result in ionospheric disturbances (Komjathy, 1997). Several examples of these type of events are given in Materassi et al. (2020)), reason why only a brief description of the most important, Solar Flares, Geomagnetic Storms and Ionospheric Storms, is given next.

Solar Flares *(SFs)* are characterized by the emission of radiation throughout the entire electromagnetic spectrum and by the ejection of charged particles. The radiation produced by *SFs* in the ultraviolet and *X-ray* bands reaches Earth in approximately eight minutes, although most part of the ejected particles take around one to two days to arrive, allowing *SFs* to serve as predictor for potential ionospheric storms. Moreover, the high energy associated with *SFs* radiation, produces a sudden ionization increase and by extension an abrupt *TEC* increase (Hernández-Pajares et al., 2011).

Geomagnetic Storms, usually occurs in conjunction with ionospheric storms (although they can occur independently of a ionospheric storm) and can be due to solar flares, high speed solar wind streams (coronal holes) and sudden disappearing filaments. These type of storms are usually associated with increased N_e in the lower ionosphere and simultaneous increase absorption of radio waves (Komjathy, 1997).

Ionospheric Storms in turn, are typically associated with the arrival of solar wind enhancement and coronal mass ejection *(CME)* events happening during solar flares, that introduce high temporal and spatial variability of the N_e distribution (Hernández-Pajares et al., 2011).

2.6. SOLAR – TERRESTRIAL INDICES

There are several types of solar terrestrial indices to monitor the Earth ionosphere and the solar activity, therefore the most common are briefly described.

2.6.1. OTTAWA SOLAR RADIO FLUX ($F_{10.7}$) AND ZURICH SUNSPOT NUMBER (Rz)

The $F_{10.7}$ index is a measure of the solar activity due to the noise level generated by the sun at a wavelength *(λ)* of *10.7 cm,* in the Earth's orbit, correlating well with the sunspot number (*Rz*) (Aragon-angel et al., 2015) and the ionizing solar radiation in the Extreme Ultra-Violet *(EUV)* range (Hobiger and Jakowski, 2017). Hence, the $F_{10.7}$ index together with the R_z can be used as an index to represent the solar ionization level in the ionosphere and be expressed by solar flux units *(sfu),* where one *sfu* equals to 10^{-22} w m^{-2} hz^{-1} (GAL-OS-IONO, 2016).

2.6.2. Kp GEOMAGNETIC INDEX

The *Kp-index* is a global geomagnetic activity index, based on 3-hour measurements from ground-based magnetometers around the world, that quantify disturbances in the horizontal component of the Earth's magnetic field. *Kp* is expressed from zero (quiet) to 9 (greatly disturbed) and according to Li et al. (2021) between 0 to 4, can be seen as quiet (minor storm), 5 to 6, moderate storm and 7 to 9, intense storm.

2.6.3. SOLAR CYCLES

The evolution of the electron content over time is clearly dominated by three periods, the daily cycle (day and night), the seasonal cycle (with maxima in spring and autumn, and minima in summer and winter) and the 11 years cycle associated with the solar flux. The latter cycle already started to ascend towards the next 25th maximum, expected to occur around July 2025 as predicted in Fig. 5.

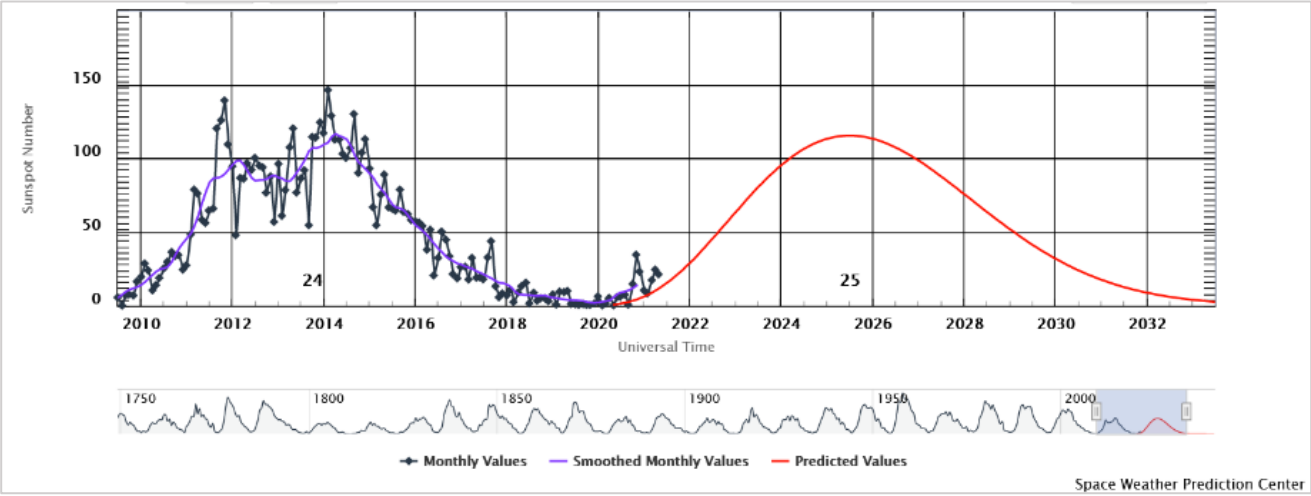

Fig. 5 – Measured 24 solar cycles (2nd row plot, in gray), last cycle (1st row plot, in blue) and next 25th solar cycle prediction (in red), by the International Solar Cycle 25 Prediction Panel (NOAA, 2021).

2.6.4. IONOSPHERIC REFRACTION INDEX

The ionospheric refraction index (*n*) is usually taken as the starting point for the ionosphere estimation impact into the travelling velocities of carrier phase (L_f) or phase modulated signals (P_f), as is the case for *GNSS* radio-frequency signals

$$I_{impact} = \int (n(s) - 1)\, ds \quad \text{(Eq. 1)}$$

Whereby, the integration of *n* takes place over the propagation path of the signal, with *n* changing with distance. For the carrier phase *(L)* and the pseudorange *(P)* estimation impact of the ionosphere, in units of meters it follows

$$I_{f,L} = -\frac{q}{f^2} - \frac{s}{2f^3} - \frac{r}{3f^4} + \cdots, \quad \text{(Eq. 2)} \qquad \text{and} \qquad I_{f,P} = \frac{q}{f^2} + \frac{s}{f^3} + \frac{r}{f^4} + \cdots, \quad \text{(Eq. 3)}$$

where, *f* is the satellite frequency (Hz) and *q*, *s*, and *r* are the 1st, 2nd and 3rd-order terms, according to

$$q = \frac{A_p}{2} \int N_e ds = 40.3 \int N_e ds \quad \text{(Eq. 4)}$$

$$s = A_p A_g \int N_e B |\cos\theta| ds = 2.256 \cdot 10^{12} \int N_e B |\cos\theta| ds \quad \text{(Eq. 5)}$$

$$r = \frac{3}{8} A_p^2 \int N_e^2 ds = 2437 \int N_e^2 ds \quad \text{(Eq. 6)}$$

where $\int N_e\, ds$, is the integral of the electron density for a cross-section of one square meter along a slant (or vertical) path between two points (e.g., from receiver to satellite). Thus, the integral of the *STEC* is referred as

$$STEC = \int N_e\, ds \quad \text{(Eq. 7)}$$

STEC typically ranges from 10^{16} to 10^{18} el/m^2 and often is expressed in terms of *TEC* Units (TECU), with 1 *TECU* equal to 10^{16} el/m^2 column. Assuming for instance an ionosphere of 60 *TECU* on (Eq. 4) then the ionospheric delay (*I*) of q/f^2 ≈ 10 m is given for the 1st order term of (Eq. 3) at GPS L_1. Additionally, using a geomagnetic field of B = $5 \cdot 10^{-5}$ tesla on (Eq. 5) the *I* will be at the level of s/f^3 ≈ 1 cm or less in the 2nd order term of (Eq. 3) and in the case of the 3rd order effect (Eq. 6), at the level of the carrier phase measurement accuracy (Leick et al., 2015).

Indeed, the 1st order term accounts for more than *99.9%* of the total *I* in both the *GNSS* code (the delay) and the carrier phase (the advance) (Hernández-Pajares et al., 2011), which encourages to consider only the 1st order term of the ionospheric effect, from equations (Eq. 2) and (Eq. 3), for the ionosphere impact as

$$I_f = \frac{\pm 40.3}{f^2} STEC \quad \text{(Eq. 8)}$$

Concurrently, for the ionospheric impact conversion between two any given frequencies the following relations can be considered

$$I_{1,P} = -I_{1,L} = -\frac{c}{f_1} I_{1,\varphi} \quad \text{(Eq. 9)} \quad \text{and} \quad I_{2,P} = -I_{2,L} = -\frac{c}{f_2} I_{2,\varphi} \quad \text{(Eq. 10)}$$

$$\frac{I_{1,P}}{I_{2,P}} = \frac{f_2^2}{f_1^2} \quad \text{(Eq. 11)} \quad \text{and} \quad \frac{I_{1,\varphi}}{I_{2,\varphi}} = \frac{f_2}{f_1} \quad \text{(Eq. 12)}$$

where *P* and *L* refer to numerical values in linear units of meters and φ subscript indicates unit of radians for the ionospheric phase advance.

Considering, for instance an ionosphere of 1 *TECU* impacting two different frequencies of *GPS* L_1 and L_2 translates to a code range delay of $I_{1,P} \approx 0.1624\, m$ for f_1 and for f_2 of $I_{2,P} = (154/120)^2 \cdot I_{1,P} \approx 0.2674\, m$, which is equivalent to differential range delay between L_1 and L_2 of $\Delta s_{I_{2P},I_{1P}} \approx 0.2674 - 0.1624 \approx 0.105\, m$ and thereof a differential time delay of $\Delta t_{I_{2P},I_{1P}} \approx 0.35\, ns$ (when divided by the speed of light).

Accordingly, the well-known relations for time and range delays between *GPS* L_1 and L_2 of $\approx 1\, ns\, per\, 2.85\, TECU$ and $\approx 1\, meter\, per\, 9.52\, TECU$ of measured ionosphere, respectively.

3. IONOSPHERIC SOUNDING

Measuring changes in the ionosphere is central to understand the solar-terrestrial environment impact on communications, surveillance, and navigation systems on Earth (Bust and Mitchell, 2008). Throughout the years, several sources of reliable data for ionospheric plasma monitoring have been used. For instance, the world-wide network of ionosondes has monitored ionospheric N_e at and below the *F-peak*; the powerful incoherent scatter radars have been measuring the plasma densities, temperatures, and velocities throughout the whole ionosphere; the topside sounder satellites providing the global distribution of N_e from the satellite altitude down to the *F-peak* region; *in situ* satellite measurements of ionospheric parameters, along the satellite orbit; and rocket observations for the lower ionosphere to obtain plasma parameters in the *D-region* (Bilitza et al., 2011).

Although a great advance and impact on atmospheric probing and ionospheric plasma sensors was achieved, when *GNSS*-based atmosphere sounding started to be used and recognized as remote sensing tool. The principle behind it, relies on the measurement of the atmospheric propagation effects on *GNSS* signals, travelling from satellites to receivers on ground or aboard satellites, that can be accurately estimated and used for atmospheric variability monitoring (Elgered and Wickert, 2017).

3.1. GLOBAL NAVIGATION SATELLITE SYSTEM (GNSS)

A brief description about the main aspects related to the *GNSS* architecture (segments and signals) and observables is given following, since the present discussion is about ionospheric modelling and receiver differential code bias and therefore, other and several interesting *GNSS* topics can be found, for instance, in Hofmann-Wellenhof et al. (2008), Subirana et al. (2013), Leick et al. (2015) and Teunissen and Montenbruck (2017).

A Global Navigation Satellite System (*GNSS*) is a generic term denoting a satellite navigation system (e.g., GPS, GLONASS, Galileo and BeiDou) that provides continuous positioning over the globe. Basically it consists of three main segments: the space segment, which comprises the satellites; the control segment, which is responsible for the proper operation of the system; and the user segment, which includes the GNSS receivers providing positioning, velocity and precise timing to users (Subirana et al., 2013) (in Fig. 6 the GPS example is shown).

3.1.1. SEGMENTS

The space segment consists of satellites themselves placed into a specific constellation orbiting about 20 200 km above the Earth and arranged in orbits to provide the desired coverage as seen in Fig. 6.a). The control segment, in turn, utilizes Earth based tracking stations spread around the world to manage

the entire navigation system. Specific locations of these stations for *GPS* are shown in Fig. 6.b) and comprise of two master control stations (one primary and one backup), four data uploading stations and *16* monitor stations. The control segment tracks and monitors errors and biases in the satellites orbit, clock, and health, this information is then sent through radio signals up to the space segment, which are then sent backdown to the user segment to track, decode and utilize for position, velocity and timing applications (Fig. 6.c)).

a) b) c)

Fig. 6 – The Global Navigation Satellite System three segment operation system, based on the Space Segment, Control Segment and User Segment; a) GPS Space Segment with six orbit planes and four satellites per plane; b) GPS Ground Control Segment; c) User Segment (VectorNav, 2021).

3.1.1.1. SPACE SEGMENT

The main functions of the space segment are to generate and transmit code and carrier phase signals, and to store and broadcast the navigation message uploaded by the control segment. These transmissions in turn are controlled by highly stable atomic clocks onboard of the satellites themselves (Subirana et al., 2013).

3.1.1.1.1. SATELLITE CONSTELLATIONS

The first satellite of a navigation system was launched by the United States in 1978, that later developed to a fully operational constellation of 24 satellites, known as the NAVSTAR Global Positioning System in 1995 (Fig. 7). Today known as *GPS* and providing a service of 31 fully usable satellites, was followed by other nations with similar constellations, as it was case of Russia, with *GLONASS* (*Global'naya Navigatsionnaya Sputnikovaya Sistema*), China with *BeiDou* (the Big Dipper) and Europe with *Galileo*.

GLONASS achieved a 24 satellite full operational capability *(FOC)* in 1996, although it dropped to only seven in 2002, due to Russia's economic difficulties. Today, its again operating with 24 satellite transmitting the legacy Frequency Division Multiple Access *(FDMA)* signals and, due to its ongoing modernization process will include the Code Division Multiple Access signals *(CDMA)* like other constellations do.

BeiDou 3rd segment, *i.e.*, the global segment after the 1st and 2nd segment integration into one regional configuration, initiated in 2015 and achieved *FOC* of 24 Middle Earth Orbit *(MEO)* satellites, plus three Inclined Geosynchronous Orbit *(IGSO)* and two Geostationary Orbit *(GEO)* in 2020. In turn, *Galileo* started offering Early Operational Capability (EOC) in 2016 and was expected to achieve *FOC* of 24 *MEO* satellites in 2020, although at the present time only 20 satellites are operating. The overall number of *MEO* operational satellites to use around the world at present time are 99.

System	GPS	GLONASS	BeiDou	Galileo
Orbit	MEO	MEO	MEO, IGSO, GEO	MEO
Nominal number of satellites	24	24	27, 3, 5	30
Constellation	6 planes 56° inclination	Walker (24/3/1) 64.8° inclination	Walker (24/3/1) 55° inclination	Walker (24/3/1) 56° inclination
Frequency (MHz)	L1 1575.42 L2 1227.60 L5 1176.45	L1 1602.00 L2 1246.00 L3 1202.025	B1 1561.098 B2 1207.14 B3 1268.52	E1 1575.42 E5a 1176.45 E5b 1207.14 E6 1278.75

Fig. 7 – An overview of the global satellite-based navigation systems adapted from (Langley et al., 2017).

3.1.2. SIGNALS

GNSS satellites continuously transmit navigation signals at two or more frequencies in the L band. These signals contain ranging codes and navigation data to allow users to compute both the travel time from the satellite to the receiver and the satellite coordinates at any epoch (Subirana et al., 2013). The main signal components are:

- Carrier: A radio frequency sinusoidal signal at a given frequency;
- Ranging code: Sequences of zeros and ones which allow the receiver to determine the travel time of the radio signal from the satellite to the receiver;
- Navigation data: A binary-coded message providing information on the satellite ephemeris (pseudo-Keplerian elements or satellite position and velocity), clock bias parameters, almanac (with a reduced-accuracy ephemeris data set), satellite health status and other complementary information.

Following, *GPS* signals are provided, described, and later used, since they are similar to other *GNSS* constellations, despite some particular differences.

3.1.2.1. GPS SIGNALS

GPS currently operates on three carrier frequencies known as L_1, L_2, and L_5. They are located on the *L-band* radar section and were chosen due to their ability to penetrate most atmospheric obstructions such as clouds, fog, or rain. Legacy *GPS* signals L_1 and L_2 were design for civilian use (case of L_1) and military applications (L_1 *and* L_2). Meaning that signals in the L_1 band (Coarse/Acquisition code C/A and the navigation message) are provided as open service for standard positioning purposes, whereas precision code signals (P-code or P(Y)), simultaneous provided in L_1 and L_2 have been restricted with cryptographic techniques to military and authorized users only (Fig. 8).

With the ongoing *GPS* signal modernization process, an additional Link 5 (L_5) frequency and several new ranging codes on the different carrier frequencies were introduced and referred to as the civil signals *L2C*, *L5C* and *L1C* and to the new military M code (Subirana et al., 2013).

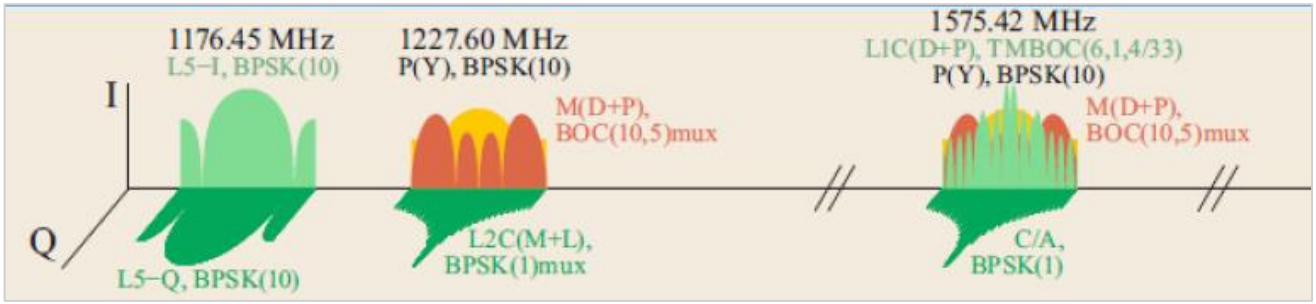

Fig. 8 – GPS signals overview. Colors indicate open signals (shades of green), authorized signals (shades of red), and signals that can be tracked with restrictions (yellow) (Teunissen and Montenbruck, 2017).

3.1.2.1.1. CARRIER, CODE (C/A AND P(Y)) AND NAVIGATION MESSAGE

The *GPS* signal from each satellite is shaped by three components, the carrier-phase (L_f), the pseudo-random noise (*PRN*) code and the navigation message (Fig. 9). The *PRN* code gives each satellite a unique identification that allows all satellites to transmit on the same frequency band without jamming. The Coarse or Acquisition (*C/A*) code is generated at 1.023 *Mbps* on the L_1 band, while the Precise code (*P-code*) signals are generated at 10.23 *Mbps* on L_1 and L_2 bands. P-codes are encrypted with Y-code to become P(Y)-code and act as an anti-spoofing measure to be single used by military applications. Recently, M-code (*GPS* modernized signals) were also introduced in L_1 and L_2 bands to provide additional protection against jamming and increase security of military *GPS* applications. The *GPS* legacy navigation message, in turn, is a binary-coded signal broken into 25 frames of 30 *s* due (50 *bps*) that enables a receiver to achieve a position solution before receiving the entire navigation message. The code and navigation message are modulated onto a sinusoidal carrier signal as shown in Fig. 9.

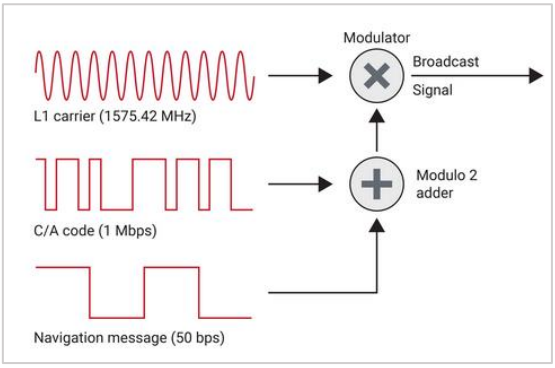

Fig. 9 – Code and navigation message modulation onto a sinusoidal carrier signal (VectorNav, 2021).

3.1.2.1.2. GPS NAVIGATION DATA

The navigation message contains all the necessary information to allow users to perform the positioning service. This includes the ephemeris parameters needed to compute the satellite coordinates with sufficient accuracy, the time parameters and clock corrections needed to compute satellite clock offsets

and time conversions, the service parameters with satellite health information, the ionospheric parameters model needed for single-frequency receivers, and the almanacs allowing computation of the position of 'all satellites in the constellation' with a reduced accuracy (1–2 km of 1σ error), which is needed for acquisition of the signal by the receiver. The ephemeris and clock parameters are usually updated every two hours, while the almanac is updated at least every six days (Subirana et al., 2013).

Currently *GPS* besides the legacy navigation message (*LNAV*), introduced four additional messages *CNAV*, *CNAV-2*, *MNAV* and *L5-CNAV,* three are civil messages, while *MNAV* is a military message. The latter messages, besides having different formats than the *LNAV* are more accurate and frequent.

3.1.3. GNSS RAW OBSERVABLES

The basic *GNSS* observable is the travel time (*ΔT*) of the signal propagation from the phase center at the satellite antenna (the emission time) to the phase center at the receiver antenna (the reception time). This value multiplied by the speed of light (*c*) gives the apparent range (*P = c ΔT*). Typically, the *P* is obtained by correlating the received *PRN* code with a replica implemented in the receiver that moves in time (*t*) until the maximum correlation is obtained (Fig. 10) (Subirana et al., 2013).

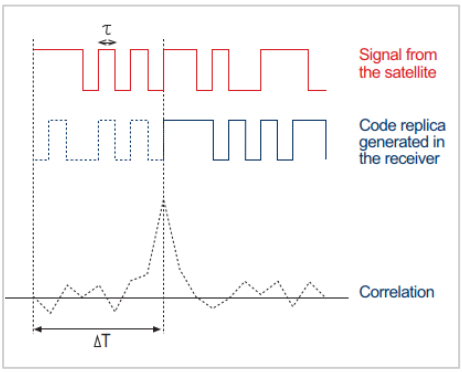

Fig. 10 – Correlation of the received *PRN* code with the receiver replica (Subirana et al., 2013).

3.1.3.1. CODE OR PSEUDROANGE

The 'apparent range', among other factors, is affected by synchronization errors between the receiver and satellite clocks, reason why it is known as the pseudorange / code range (*P*), since it doesn't match the true geometric distance. Therefore, the P_f measurement (at frequency *f)* obtained by the receiver will also include besides the geometric range (*ρ)*, clock synchronization errors, signal propagation delays, relativistic effects, instrumental delays, multipath and receiver noise (Fig. 11). Taking all these terms into account we can write the P_f, as follows:

$$P_f = \rho + c(dt_r - dt^s) + T + \alpha_f STEC + K_{f,r} - K_f^s + M_f + \varepsilon_f \quad \text{(Eq. 13)}$$

where, *ρ* is the geometric range between the satellite and receiver Antenna Phase Centers (*APC*) at emission and reception time respectively, dt_r and dt^s are the receiver and satellite clock offsets from the *GNSS* time scale including the relativistic satellite clock correction; *T* is the tropospheric delay (non-dispersive); α_f *STEC* is the frequency-dependent ionospheric delay term, where α_f is a conversion factor given by $\alpha_f \cong \frac{40.3}{f^2} 10^{16}\, m/TECU$; $K_{f,r}$ and K_f^s are the receiver and satellite instrumental delays,

dependent on the code type and frequency; M_f represents the multipath effect also dependent on code and frequency, and ε_f is the receiver noise.

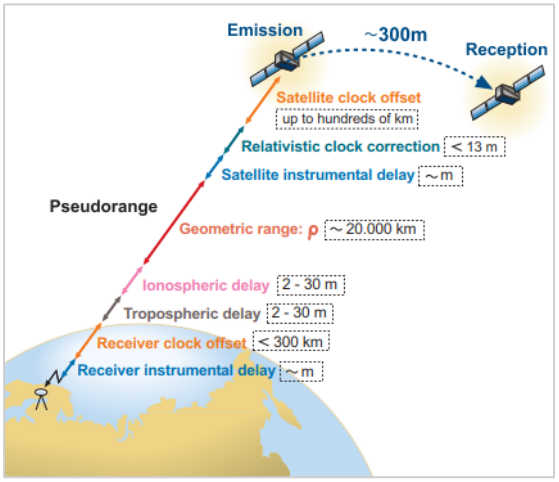

Fig. 11 – Pseudorange measurement contents and significance if not accounted for in the standard observation model (Subirana et al., 2013).

3.1.3.2. CARRIER PHASE

The carrier-phase (L_f) can also be used to obtain a measure of the apparent distance between satellite and receiver. These L_f measurements are much more precise than P_f measurements from two to three orders of magnitude smaller, *i.e.*, approximately at millimeter level ($\simeq 0.01\lambda_f$, λ_f being the frequency wavelength), along with a smaller multipath effect (less than $\lambda_f/4 \simeq 0.05$m), forwarding this observable as the most proper measurement for high-accuracy applications in general and for ionospheric sounding in particular (Hernández-Pajares et al., 2011). However, carrier-phase measurements include an unknown number of integer wavelengths ($\lambda_f N_f$) often referred as the ambiguity term (B_f). Indeed, this ambiguity changes arbitrarily every time the receiver loses lock on the signal, producing jumps or range discontinuities, that needs to be properly solved in each continuous arc of data (*i.e.*, with no cycle-slips (Blewitt, 1990)). The L_f measurements can be modelled as

$$L_f = \rho + c(dt_r - dt^s) + T - \alpha_f STEC + k_{f,r} - k_f^s + \lambda_f N_f + \lambda_f w + m_f + \epsilon_f \quad \text{(Eq. 14)}$$

where, besides the terms from (Eq. 13), it includes the frequency dependent wind-up term $(\lambda_f w)$ due to the circular polarization of the electromagnetic signal and the frequency dependent integer ambiguity term N_f.

3.1.4. COMBINATION OF OBSERVABLES

From the raw observables described and following Subirana et al. (2013), the combinations often used in *GNSS* applications are the Ionospheric-free combination of carrier (L_C) and code (P_C) measurements, (Eq. 15) and (Eq. 16), respectively, for 1st order ionospheric effect removal and the Geometry-free combination of carrier (L_I) and code (P_I) measurements, (Eq. 17) and (Eq. 18), respectively, to cancel out the geometric part of the measurements and leave all the frequency-dependent effects

$$L_C = \frac{f_1^2 L_1 - f_2^2 L_2}{f_1^2 - f_2^2} \quad \text{(Eq. 15)} \quad \text{and} \quad P_C = \frac{f_1^2 P_1 - f_2^2 P_2}{f_1^2 - f_2^2} \quad \text{(Eq. 16)}$$

$$L_I = L_1 - L_2 \quad \text{(Eq. 17)} \quad \text{and} \quad P_I = P_2 - P_1 \quad \text{(Eq. 18)}$$

Other combinations can be done and acquired in Subirana et al. (2013).

3.1.4.1. OBSERVABLES MODEL REARRANGEMENT

It is reasonable to perform some rearrangements to refer the clocks of the raw observables to the code Ionosphere-free (P_C) combination of f_1 and f_2 frequencies, before performing a combination of observables. According to Subirana et al. (2013) this new clock (δt) redefinition will enable the code instrumental delay (K) to cancel out in the P_C combination and to appear always along with the ionospheric term and a frequency-dependent coefficient $\alpha_{(\cdot)}(I + k_{21})$, where, K_{21} (is the satellite plus receiver DCBs for frequencies f_1 and f_2) given as

$$K_{21} = K_{21.rcv}^{sat} = \left(K_{2,rcv} - K_{1,rcv}\right) - (K_2^{sat} - K_1^{sat}) = K_{21,rcv} - K_{21}^{sat} = K_{2,rcv}^{sat} - K_{1,rcv}^{sat} \quad \text{(Eq. 19)}$$

and (I) is taken as the ionospheric delay in the geometry-free combination

$$I = (\alpha_2 - \alpha_1) \cdot STEC \cong \frac{40.3\,(f_1^2 - f_2^2)}{f_1^2 f_2^2} 10^{16} \cdot STEC \quad \text{(Eq. 20)}$$

In this sense (Eq. 13) and (Eq. 14) can be rewritten (full derivation given in Subirana et al. (2013)) as

$$P_i = \rho + c(\delta t_r - \delta t^s) + T + \tilde{\alpha}_i(I + K_{21}) + M_i + \varepsilon_i \quad \text{(Eq. 21)}$$

$$L_i = \rho + c(\delta t_r - \delta t^s) + T - \tilde{\alpha}_i(I + K_{21}) + b_i + \lambda_i N_i + \lambda_i w + m_i + \epsilon_i \quad \text{(Eq. 22)}$$

where, $\tilde{\alpha}_i \equiv \frac{\alpha_i}{\alpha_2 - \alpha_1}$, $(i = 1{,}2)$, $\alpha_i = \frac{40.3}{f_i^2} 10^{16}\ m/TECU$, and $b_i = k_i - K_i + 2\tilde{\alpha}_i K_2$, will be a frequency dependent bias as the code bias to be split in into two different terms $b_i = b_{i,rcv} - b_i^{sat}$, for the receiver and the satellite carrier phase bias (Subirana et al., 2013).

The advantage of including K_{21} in the equations of carrier-phase measurements (Eq. 22), joining the ionosphere term (I) is to provide closed expressions for different combinations of measurements that are especially useful when working with combinations of pairs of frequencies that simplify relationships between equations and parameters (Subirana et al., 2013). As it can be proven from the resulting equations (Eq. 23) and (Eq. 24) given for the geometry-free combination in 4.1.1.

4. DCB ESTIMATION WITH IONOSPHERIC TEC MODELS

The ionospheric *TEC* accounts for one of the most important parameters for atmospheric remote sensing (Liu et al., 2020), however, ionospheric *TEC* and *DCB* usually need to be estimated simultaneously.

DCB can be classified into two categories from the observation data type perspective: *intra*-frequency *DCB* occurring between two different types of observations obtained at the same frequencies; and inter-frequency *DCB* occurring between two observations obtained from two different frequencies.

DCB occurs at the satellite and receiver instruments, the former named as satellite *DCB (sDCB)* and the latter as receiver *DCB (rDCB)* (Hernández-Pajares et al., 2011). Generally the *sDCB* can be understood as the delay from signal generation to signal arrival at the transmission *APC*, including signal generation, demodulation, up conversion and transmission to the satellite *APC*, whereas the *rDCB* can be understood as the delay from receiver *APC* to signal acquisition and tracking, in which the bias introduced by the digital filter is the main source of *rDCB* (Hauschild and Montenbruck, 2016).

For the estimation of *inter*-frequency *DCB* corrections normally the methods can be divided into three categories: *(1)* hardware calibration used to measure the *DCB* by special instruments before satellites and receivers are put into use; *(2)* simultaneous estimation of ionospheric *TEC* and *DCB* parameters based on global or regionally ionospheric *VTEC* modeling; and *(3) DCB* estimation after the deduction of ionospheric *TEC* externally provided by *TEC* models such as *GIMs* or three-dimensional *(3-D)* ionospheric models (Liu et al., 2020).

An overview for the combination of techniques applied by the Ionospheric Associate Analysis Centers *(IAACs)* of the International GNSS Service *(IGS)* Working Group on Ionosphere *(Iono- WG)* and by the scientific community, in general, to estimate *DCB* simultaneous with *TEC* or as a post-fit to *TEC,* are organized in the form of a flowchart in Fig. 12.

Although, before proceeding with a brief description about the techniques applied in Fig. 12 a note related with the nomenclature for the ionospheric models should be done. According to Radicella and Nava (2020) parameterized models are based on orthogonal function fits to data outputs of physics-based models, which in turn, are based on conservation equations (of continuity, momentum, energy, etc.) solved numerically for electrons and ions as function of spatial and time coordinates (Radicella and Nava, 2020). Indeed, for the common *DCB* and ionospheric *TEC* retrieval based on orthogonal function fits and / or interpolations, it seems adequate to frame them as *geomatic models* instead of parameterized, since, what they really do, is a combination of mathematical function

adjustments in a geo- or sun-fixed system of coordinates to ionospheric observations. While, empirical models rely on the description of ionospheric parameters with mathematical functions derived from historic experimental data for the description of average and regular variations of ionospheric parameters (Radicella and Nava, 2020).

4.1. SIMULTANEOUS DCB AND IONOSPHERIC TEC RETRIEVAL

4.1.1. MEASUREMENTS

The code P_I and carrier-phase L_I ionospheric observable are given as

$$P_I = P_2 - P_1 = I + K_{21} + \varepsilon_{P_I} \quad \text{(Eq. 23)}$$

$$L_I = \phi_1 - \phi_2 = I + K_{21} + B_I + \beta \cdot \omega + \varepsilon_{L_I} \quad \text{(Eq. 24)}$$

where, the wind-up term (ω) affected by $\beta = (\lambda_1 - \lambda_2) = -0.054\, m\, (GPS)$ is at the centimeter level and accurately corrected for permanent receivers (and neglected hereafter). The ionospheric delay (I) is defined by (Eq. 20) as $I = \alpha \cdot STEC$, where $\alpha \cong 0.105\ m/TECU$ (GPS $_{L1\text{-}L2}$), K_{21} is the sum of the satellite and receiver *DCB* in meters and ε (m) is the combination of noise and multipath effect distinguishing the pseudorange ε_{P_I} from the carrier-phase ε_{L_I}. Additionally, B_I is the ambiguity term which is the main limiting factor that prevents the carrier-phase measurements to be treated as precise pseudorange, expressed as

$$B_I = b_I + (\lambda_1 N_1 - \lambda_2 N_2) \quad \text{(Eq. 25)}$$

where, $b_I = b_1 - b_2$, is the ionospheric bias, $b_{(i)}$ is the frequency dependent (f_i) carrier phase bias and $\lambda_1 N_1$ and $\lambda_2 N_2$ are the unknown number of integer wavelengths for each frequency. Therefore, the key for using the carrier phase observable in *STEC* retrieval will reside in the ability to isolate the integer ambiguities from the estimated real parameter B_I and explicitly fix those values to integers. In fact the difference of the ionospheric observables P_I and L_I, will be in the procedure to solve for the ionospheric bias in (Eq. 25) (Nie et al., 2018).

4.1.1.1. CARRIER-TO-CODE LEVELLING (CCL)

One of the methods to solve for the ionospheric bias (b_I) is to align L_I with P_I, *i.e.*, averaging the difference between the L_I and P_I ionospheric observable. In this sense, for a continuous arc assuming there are (n) epochs, the ambiguity term can be computed as

$$\langle L_I - P_I \rangle_{arc} = \frac{1}{n} \sum_{i=1}^{n} (L_I - P_I)_i = \bar{B}_I + \varepsilon_{\langle I \rangle} \quad \text{(Eq. 26)}$$

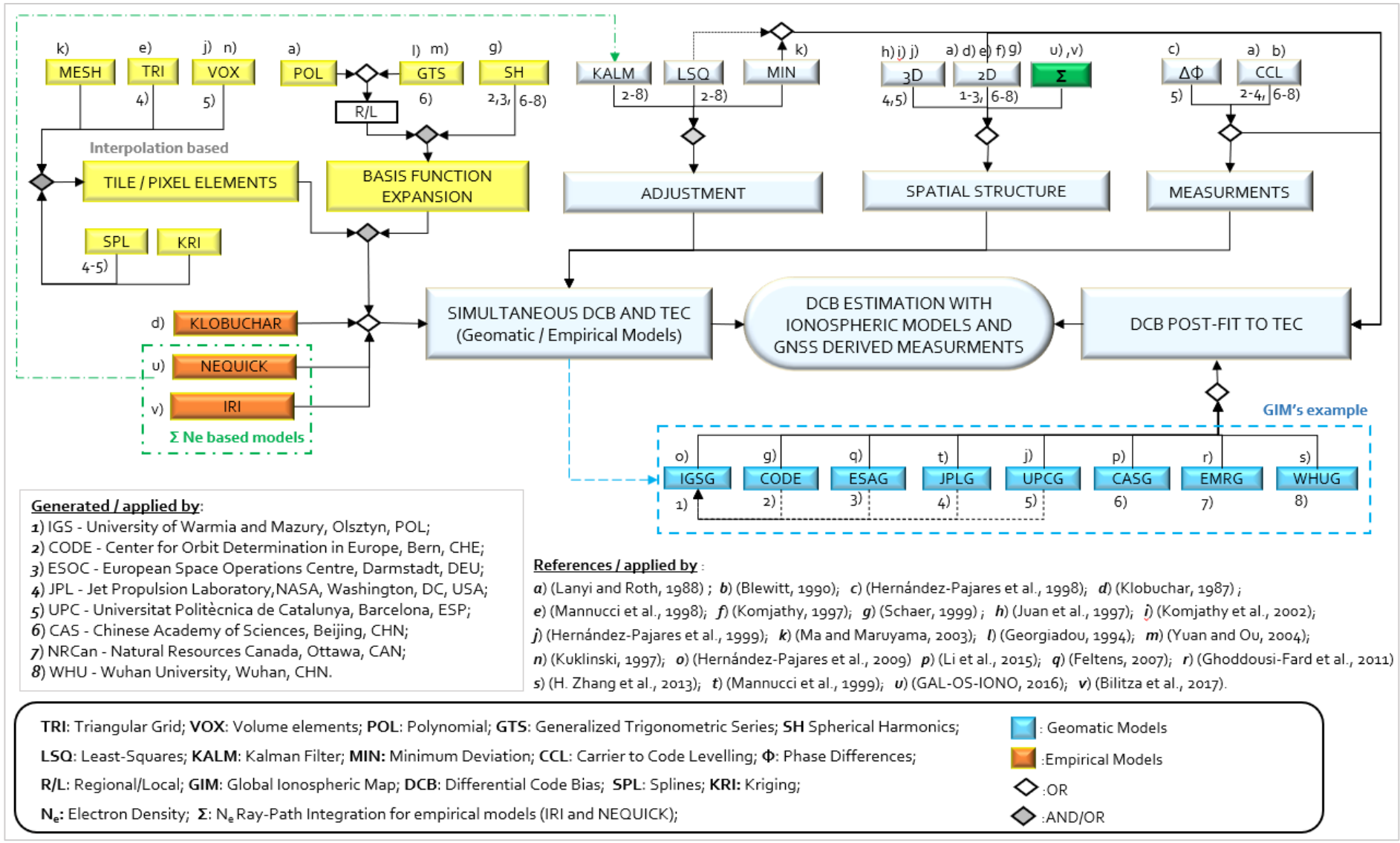

Fig. 12 – Flowchart with classical *DCB* estimation strategies according to measurements, spatial structure, adjustment technique and adopted *TEC* model for ionospheric space-time variability description.

where < > stands for the average value during the time period of the carrier-phase measurements belonging to the same arc and $\varepsilon_{\langle I \rangle}$, is the leveling error from the combination of the code and carrier phase measurement noise as well as the multipath effects (Ciraolo et al., 2007). Combining (Eq. 24) and (Eq. 26) we get the Carrier L_I to P_I Code leveled (CCL) ionospheric observable as:

$$sP_I = L_I - \bar{B}_I = L_I - \langle L_I - P_I \rangle_{arc} = I + K_{21} + \varepsilon_{SP_I} \quad \text{(Eq. 27)}$$

It is important to note that (Eq. 27) neglects the effect of noise and multipath from the carrier-phase observations, since it has no influence in the results, because they are 100 times smaller than the ones on the code-delay (Ciraolo et al., 2007). In this way, the accuracy for the *CCL* observable *(sP_I)* is mainly affected by leveling errors ranging from ± *1.4* to ± *5.3 TECUs* (Ciraolo et al., 2007).

4.1.1.2. CARRIER PHASE DIFFERENCES

At the present time, Universitat Politècnica de Catalunya *(UPC)* is the only *IAACs* that acquires *STEC* ionospheric observations single based on carrier-phase difference measurements. The *UPC* approach avoids the alignment with code for ambiguity estimation and simultaneously cancels out the phase ambiguity, during the carrier phase differences to the first point of each satellite to receiver continuous phase arc, according to the expression

$$\frac{\Delta L_I}{k} = L_I(t+\tau) - L_I(t) \quad \text{(Eq. 28)}$$

where, $k = 0.105\ m/TECU$ and τ, is the amount of time to provide enough geometry variation of the ray-path and therefore allow the solution for the N_e retrieval (more details in Hernández-Pajares et al. (1998)).

4.1.2. SPATIAL STRUCTURE

Lanyi and Roth (1988) concluded that *TEC* and sum of *sDCB* with *rDCB,* could statistically be estimated if three important assumptions were considered: *(1)* the temporal behavior of the ionosphere was assumed to be time independent in a reference frame fixed to Earth-Sun axis; *(2)* the ionosphere geometry was approximated by a spherical shell with infinitesimal thickness to represent *VTEC* using a mathematical model over a subarea of this shell at 350 km height; and *(3)* the instrumental characteristics of *sDCB* and *rDCB* had to be considered constant in time.

Those assumptions suggested that *DCB* could be considered constant offsets with different time or elevation-angle dependence, than the ionospheric delay, which enabled the separation from the ionospheric component with high precision *(<<1 TECU)* and reasonable accuracy from one to three *TECU* (Mannucci et al., 1998) and (Mannucci et al., 1999).

4.1.2.1. IONOSPHERIC 2-D TEC MAPPING – THE SINGLE LAYER MODEL

According to (Eq. 20) and Fig.13, *STEC* is estimated by the integration of N_e along the propagation path between a receiver, here designated by *Rx,* and a satellite transmitter, here designated by *Tx,* as

$$STEC = \int_{R_x}^{T_x} N_e \times ds = \sum_{i=1}^{n} (N_e)_i \delta s_i \cong \sum_{i=1}^{n} \frac{(n_e)_i \delta h_i}{\frac{\delta h_i}{\delta s_i}} = \sum_{i=1}^{n} \frac{\delta V_i}{\cos \zeta_i} = \sum_{i=1}^{n} M_i \delta V_i \qquad \text{(Eq. 29)}$$

where *ds* is the line-of-sight distance; *n* the number of discretized layers; δs_i and δh_i are the slant and vertical height element of *i* th layer; ζ_i is the zenith distance at ionospheric pierce point *(IPP)* of *i* th layer; δV_i is the *VTEC* of *i* th layer and M_i is the mapping function *(MF)* of the *i* th layer (Hernández-Pajares et al., 2011).

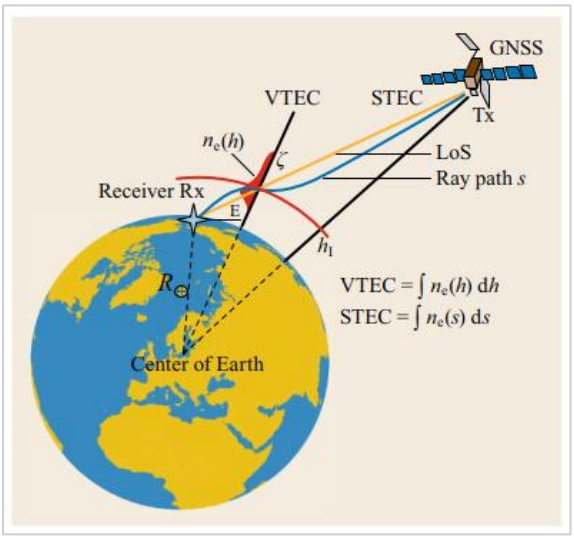

Fig.13 – Thin-shell mapping function approach mapping VTEC deduced from STEC measurements (Hobiger and Jakowski, 2017).

Since *GIMs* (geomatic models in Fig. 12) usually provide normalized information in terms of *VTEC,* then any link related *STEC* can only be computed if a so-called obliquity factor or *MF* dependent of the ray-path elevation *(E)* and layer height is applied. Therefore, assuming a thin-shell ionosphere (*n=1*) and applying a geometric relationship for *STEC* conversion to the corresponding V*TEC,* at the *IPP* of the ray-path *s* with the ionospheric shell height h_I, provides the following single layer model *(SLM)* mapping function

$$M(E) = \frac{STEC}{VTEC} = \frac{1}{\cos \zeta} = \left[1 - \left(\frac{R_\oplus \cos E}{R_\oplus + h_I}\right)^2\right]^{-1/2} \qquad \text{(Eq. 30)}$$

where $R_\oplus$ is the Earth radius and h_I is usually within the height interval of *350−450 km*. Different approximations have been used, Klobuchar (1987), suggested that for a single layer height of 350 km and an *E* between 5° to 90°, within a *2%* margin error, the following MF could be used

$$M(E) = 1 + 2\left(\frac{96° - E}{90°}\right)^3 \qquad \text{(Eq. 31)}$$

Later, Schaer (1999) advanced with a modified the SLM *(MSLM)* mapping function with reference to N_e *Chapman* profile correction factor *α,* dependent of a minimum elevation *E* (or maximum zenith distance) at the receiver and an optimum shell height H_{opt}, as follows

$$M(E) = \left[1 - \left(\frac{R_\oplus \cos(\alpha \cdot E)}{R_\oplus + H_{opt}}\right)^2\right]^{-1/2} \qquad \text{(Eq. 32)}$$

where, for a minimum elevation of 10°, yields a H_{opt} of 403.1 *km* and *α* of 0.9886 (Schaer, 1999).

The computation of *STEC* from a given *VTEC* map should therefore be performed with the same *MF* used to compute the original map, otherwise, the results will be degraded, jeopardizing any improvement associated with a better *MF* (Hernández-Pajares et al., 2011). This is why the ionospheric *MF* is one of the first assumptions to consider when ionospheric corrections are need to apply in *GNSS* data (Hernàndez-Pajares et al., 2005).

4.1.2.2. IONOSPHERIC 3-D TEC MAPPING

To additionally improve *TEC* mapping other techniques have been used to separate the ionosphere into different spherical layers with specific *MF* (Mannucci et al., 1999), or to apply tomographic methods that provide *3-D* estimations of the ionospheric *Ne* (Hernàndez-Pajares et al., 2005).

4.1.2.2.1. A MULTI-LAYER MODEL BASED ON THREE THIN SHELLS

To solve for the electron content distribution on multiple horizontal grids vertically distributed (multiple-shell), Komjathy et al. (2002) introduced a modified model that approximates the ionosphere to a three-thin shell model, with each shell being centered at a fixed altitude instead of using a single grid at a fixed height (Fig. 14). In fact, this was a simple extension of the *SLM* from one to three shells, to solve for the horizontal basis functions on separate layers. Accordingly, the following observation equation

$$STEC = M(h,E)\sum_i C_i B_i(\theta,\phi) + b_r + b_s \qquad \text{(Eq. 33)}$$

where (θ, ϕ), are latitude and longitude of each *IPP*, *M(h,E)* is the thin-shell *MF* for the satellite elevation angle (*E*) and layer height (*h*), B_i are the horizontal *MF* (triangular tiles, bi-cubic splines, etc.), C_i are the basis function coefficients, and b_s and b_r are the *sDCB* and *rDCB*, respectively (Komjathy et al., 2002).

An illustration for the three shells set at *250*, *400* and 800 km, where the line-of-sight vector piercing the ionosphere at three separate points is shown (Fig. 14). The *STEC* data is converted to the vertical using the obliquity function $M(h_i,E)$ separately computed for the three shells, then the *VTEC* dependence on θ and ϕ is parameterized according to a linear combination of basis functions B_i and coefficients C_i in a solar-geomagnetic θ_s and ϕ_s dependency (Komjathy et al., 2002).

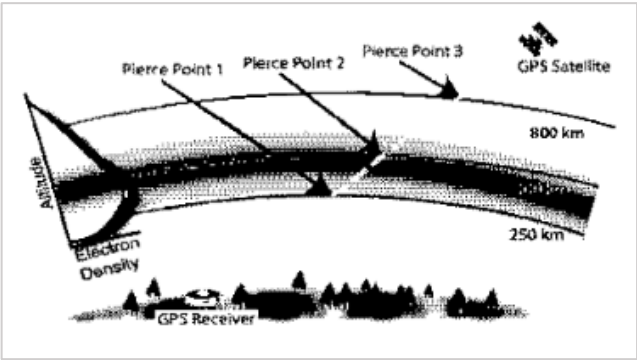

Fig. 14 – *JPL* three-shell model with layer heights at 250, 400 and 800 km (Mannucci et al., 1998).

4.1.2.2.2. TOMOGRAPHIC BASED MODELS

The formality to retrieve direct *3-D* derivations of the N_e applying tomographic techniques and estimate a global *VTEC* model according to Hernández-Pajares et al. (2011) is given by

$$N_e = \sum_i \sum_j \sum_k (N_e)_{i,j,k} \cdot p_{i,j,k} \quad \text{(Eq. 34)}$$

where the volume elements or voxel basis functions $P_{i,j,k}(r)$, that "tessellate" the sphere are defined as *1* if *r* (length of the ray-path crossing the "illuminated cells" at time *t*) is closer to the voxel center $r_{i,j,k}$ than to the other voxel centers or, 0, otherwise (Fig. 15 and Fig. 18); the values of the index *k* run over the different layers of the model as *i,j* runs the horizontal distribution of each voxel. Accordingly, *p*, the length segment of the satellite to receiver ray intersection with a voxel *i - j - k* ($\Delta l_{i,j,k}$) is expressed as $\Delta l_{i,j,k} = \int_{r_T}^{r_R} p_{i,j,k} \mathrm{d}l$, and the main observation (Eq. 24) based on the ionospheric carrier-phase can consequently be written with (Eq. 29) as:

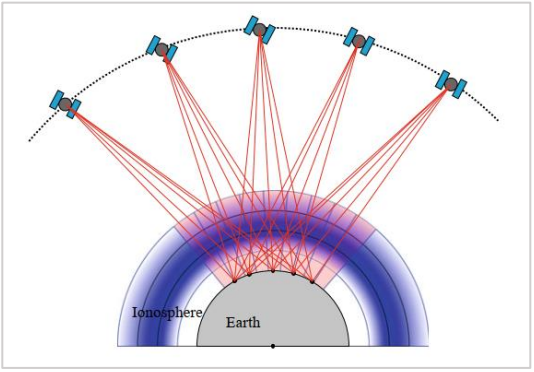

Fig. 15 – Ionospheric electron density ray tomography geometrical coverage, (Jin et al., 2019).

$$L_I \cong \alpha \sum_i \sum_j \sum_k (N_e)_{i,j,k} \cdot \Delta l_{i,j,k} + B_I \quad \text{(Eq. 35)}$$

This approach avoids the *VTEC* mis-modeling associated with a fixed height assumption of the electron content distribution and is suitable to obtain local details by the limited scope of every basis function $P_{i,j,k}$ (Hernández-Pajares et al., 2011).

4.1.2.3. 3-D ELECTRON DENSITY INTEGRATION

From the last example the benefit of using *3-D* N_e integration against *2-D SLM* or discrete *3-D* multiple *SLM,* evidences the advantage of using *3-D TEC* models to integrate the N_e along any ray-path as it is the case, for instance, of *NeQuick-G* and *IRI* (described in 4.1.4.2 and 4.1.4.3, respectively) and therefore, avoid *MF* conversion errors.

4.1.3. MATHEMATHICAL FUNCTIONS

The ionospheric structure and its variation are rather complicated in both time and space, which unavoidable leads to the difficulty task of describing the ionosphere with a unified mathematical model. Thence it is important to describe the capability of different mathematical models (Li et al., 2019) and choose a suitable mathematical representation for *VTEC* spatial and temporal variability (Brunini and Azpilicueta, 2009).

4.1.3.1. BASIS FUNCTIONS EXPANSION

Various functions have been suggested by several authors, the most used are the Polynomial Function (Lanyi and Roth, 1988) *(POLY)*, Generalized Trigonometric Series Function (Yuan and Ou, 2004) *(GTSF)* and the Spherical Harmonic expansion functions (Schaer, 1999) *(SH)*. Different models, different *DCB* accuracy's and, even for the same models, but with different degrees and orders, totally different results (Kao et al., 2013).

4.1.3.1.1. POLYNOMIAL EXPANSION

The *POLY* model is based on a *2-D Taylor* expansion at the central point of the surveyed area and its conventional expression is given as follows:

$$VTEC(\theta, s) = \sum_{m=0}^{n_{max}} \sum_{m=0}^{m_{max}} E_{nm} (\theta - \theta_0)^n \, (s - s_0)^m \quad \text{(Eq. 36)}$$

Herein, E_{nm} is the *Taylor* expansion coefficient of the ionosphere to be solved; $\theta - \theta_0$ indicates the difference of latitude between the *IPP* and the center of the measurement area; $s - s_0$ is the difference of solar hour angle between the *IPP* and the center of the measurement area; *n* and *m* are the model orders in θ and ϕ, respectively (Jin et al., 2019).

4.1.3.1.2. GENERALIZED TRIGONOMETRIC SERIES

The 15th parameter trigonometric series was first developed by Georgiadou (1994) and then extended by Yuan and Ou (2004), to better express the diurnal variation of *TEC* at mid-latitudes, with adjustable parameters in geographical or geomagnetic coordinates

$$\begin{aligned} VTEC = \; & A_1 + \sum_{i=1}^{N_2} A_{i+1} \theta_m^i + \sum_{i=1}^{N_3} A_{i+N_2+1} h^i + \sum_{i=1,j=1}^{N_I,N_J} A_{i+N_2+N_3+1} \theta_m^i h^j + \\ & + \sum_{i=1}^{N_4} \left\{ A_{2i+N_2+N_3+N_I+N_J} \cos(ih) + A_{2i+N_2+N_3+N_I+N_J} \sin(ih) \right\} \end{aligned} \quad \text{(Eq. 37)}$$

where, A_i are the model coefficients; N_2, N_3, N_I, N_J and N_4 are the adjustable model orders; $\theta_m = \theta_i + 0.064 \cos(\phi_i - 1.617)$ is the geomagnetic latitude at *IPP*, θ_i and ϕ_i are geographic latitude and longitude at *IPP* and $h = \frac{2\pi}{24}(t - 14)$, with local time (*t*) in hours at sub-ionospheric point.

4.1.3.1.3. SPHERICAL HARMONICS EXPANSION

The *SH* functions compose of an orthogonal system where any *SH* can be expanded as a linear combination of the *SH* functions. The *SH* function for ionospheric *TEC* can be expressed as follows (Schaer, 1999):

$$VTEC(\phi, s) = \sum_{n=0}^{n_{max}} \sum_{m=0}^{n} \tilde{P}_{nm}(\sin\theta) \left[\left(\tilde{C}_{nm} \cos(m\, s) + \tilde{S}_{nm} \sin(m\, s) \right) \right] \quad \text{(Eq. 38)}$$

where θ is the geodetic/geomagnetic latitude of the *IPP*; $s = \phi - \phi_s$ is the Sun time angle for *IPP*, where ϕ, ϕ_s are the geodetic/geomagnetic longitude of the *IPP* and the Sun geodetic/geomagnetic longitude at the corresponding epoch, respectively; n_{max} is the highest order of *SH* expansion; $\tilde{P}_{nm} = N_{nm} P_{nm}$ is the normalized associated *Legendre* function with *n* order and *m* degree, where N_{nm} is the normalization factor, P_{nm} is the classical *Legendre* function; $\tilde{C}_{nm}$, are the unknown SH coefficients to be determined and $\tilde{S}_{nm}$ are the Global Ionospheric Map parameters, *i.e.*, the regional or global ionospheric electron content model parameters (full details are given in Schaer (1999)).

4.1.3.2. TILE OR VOLUME BASED INTERPOLATION

Spatial interpolation methods also play a prominent role in the process of grid-based ionosphere modeling, especially for under-sampled regions where GNSS stations are sparsely and irregularly distributed. Various interpolation methods have been extensively studied, *e.g.*, Ordinary Kriging *(OrK)*, Universal Kriging *(UnK)*, Inverse-Distance Weighting *(IDW)*, interpolating polynomials, B-splines, and multiquadratic (Li et al., 2018).

4.1.3.2.1. MESH TILES

Although the following example did not apply any mathematical interpolation technique due to its dense network of receivers, it can be given as mesh based example for *TEC* retrieval within each mesh boundary and size. Ma and Maruyama (2003), taking advantage of the *GPS* Earth Observation Network *(GEONET)* set up by the Geographical Survey Institute *(GSI)* of Japan (Fig. 16), established a 32 mesh grid, each with a 2x2° in θ and ϕ, where *TEC* could be evaluated independently. For each mesh, much as 20 receivers could be present, although in several others none. The *TEC* in the latter meshes had to be obtained with the receivers in the adjacent ones. Therefore, without employing a complex mathematical model the strategy for *TEC* retrieval assumed an identical *VTEC* at any point within a mesh, but for different meshes they could differ. Hence, for any lines of sight converging on the same mesh the vertical components of their *STEC* were all taken to be the same.

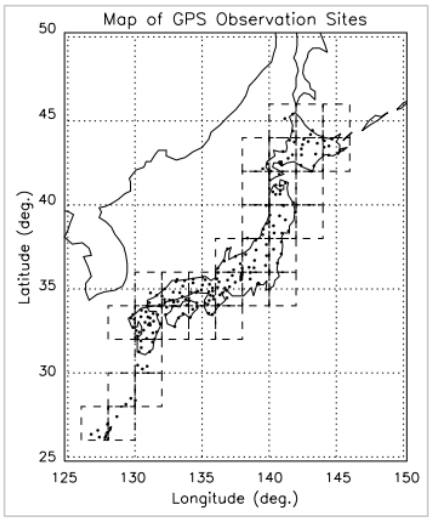

Fig. 16 – Dual frequency receivers of Japan *GPS* Earth Observation Network (*GEONET*). The dash lines separate the area enclosed into 32 meshes. The size of the mesh is 2º by 2º in longitude and latitude, respectively (Ma and Maruyama, 2003).

4.1.3.2.2. TRIANGULAR TILES

The Jet Propulsion Laboratory *(JPL)* developed a technique for global *VTEC* retrieval that resorts to a locally supported basis functions, within individual triangular tiles, that «tessellates» the sphere with a single shell ionospheric model for *TEC* interpolation. Each tile is regarded as a rigid plate that tilts to follow the measured *TEC* gradients within the tile (Fig. 17). The intra-tile *TEC* of the rigid plate model is expressed as a linear combination of the *TEC* values at each vertex of the triangular tile. Whereas, each vertex *TEC* value is multiplied by a weighting function that depends on the distances to the three vertices of the intersected tile (Mannucci et al., 1998).

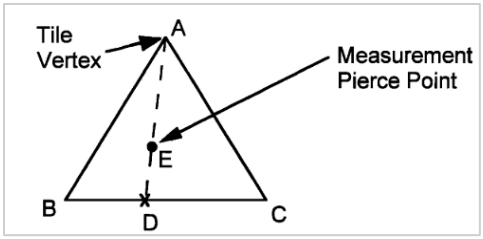

Fig. 17 – Triangular tiles used for TEC interpolation and representation by JPL (Mannucci et al., 1998).

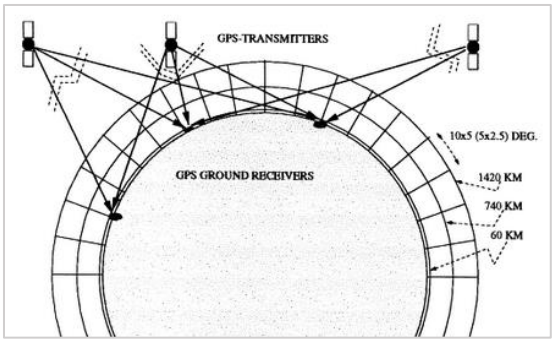

Fig. 18 – UPC two layer voxel for ionospheric global TEC mapping (Hernández-Pajares et al., 1999)

4.1.3.2.3. TWO LAYER VOXELS

Rius et al. (1997) presented the first experimental results that used GPS data to image the ionosphere in tomography based manner. Although the vertical grid he adopted consisted only of four height voxels, it was a key step to the transition from *2-D* mapping and intermediate multiple shells into *3-D* imaging (Bust and Mitchell, 2008). Following, Hernández-Pajares et al. (1999) developed the first practical application for *GIM* by setting up a two layer grid of voxels, with horizontal sizes of 10×5° and 5×2.5°, in local time and latitude, at the layer boundaries between 60-740 km and 740-1420 km, respectively, (Fig. 18).

4.1.4. EMPIRICAL MODELS

Although, empirical models, such as *Klobuchar's*, *NeQuick*, *IRI* and others, already provide a *STEC / VTEC* measurement based on a pre-defined user and broadcast related parameters, these same models can also be used as an adjustment *TEC* model to fit uncalibrated ionospheric observations. Thus, if an adequate data processing strategy is adopted during the selected adjustment procedure the hereby mentioned empirical models, can be applied for simultaneous *DCB* and *TEC* retrieval (as suggested in Fig. 12).

4.1.4.1. KLOBUCHAR

GPS ICA, developed by Klobuchar (1987) uses eight broadcast coefficients to describe the ionosphere with a *SLM* capable of removing over 50% of the ionospheric error, according to the mean estimated vertical delay at L_1, for a given local time and geomagnetic location. The diurnal variation of the vertical delay is modelled by a cosine function with varying amplitude and period, dependent of the geomagnetic latitude Θ. The phase of the cosine is fixed to 14 h Local Time *(LT)* and during nighttime the vertical delay is approximated to a constant value of 5 ns (Fig. 19). The dependency on Θ is given by a *3rd* order polynomial, with the coefficients α_n and β_n (eight in total) broadcasted in the *GPS* navigation message (Radicella et al., 2008).

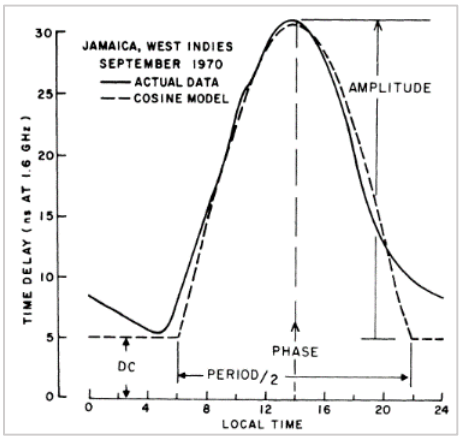

Fig. 19 – Fit example for the cosine model of monthly average ionospheric time-delay, as presented by Klobuchar (1987) for Jamaica, West Indies station, September 1970.

4.1.4.2. NEQUICK

NeQuick is a *3-D* and time dependent ionospheric N_e model particularly tailored for trans-ionospheric applications that allows to calculate the electron concentration at any location in the ionosphere and thus *TEC,* along any receiver to satellite (*rcv-sat*) ray-path by means of numerical integration (Nava et al., 2008). It estimates the *TEC* for radio-wave propagation forecast based on empirical climatological representations of the ionosphere that predict the N_e monthly means from analytical profiles, depending on the solar activity-related values, as the smoothed sunspot number (R_{12}) or $F_{10.7}$ solar flux, month of the year, geographic latitude, longitude, height and universal time (*UT)* (GAL-OS-IONO, 2016).

NeQuick has been adapted for real-time *Galileo* single-frequency ionospheric corrections (*NeQuick-G*), based on the Effective Ionization Level (*Az*) input parameter, determined by three broadcast coefficients, included in the navigation message for real-time predictions (GAL-OS-IONO, 2016). The *Az* is defined as follows:

$$Az(\mu) = a_0 + a_1\mu + a_2\mu^2 \quad \text{(Eq. 39)}$$

where, μ is the modified dip latitude (modip), with $\mu = I'/\sqrt{\cos\theta}$, being *I'* the true magnetic inclination or dip in the ionosphere (usually at 300 km), θ the geographic latitude of the receiver (Rawer, 1963), and a_0, a_1, a_2 the three broadcast coefficients. For the μ computation, *NeQuick-G* uses an internal grid file with the newer International Geomagnetic Reference Field (*IGRF*) version model for the Earth's magnetic field.

NeQuick-G provides a correction capability of at least 70% of the ionospheric code delay *RMS*, with a lower STEC residual error bound of 20 *TECU* for any location, time of day, season, and solar activity, excluding the periods where the ionosphere is largely disturbed, for instance due to geomagnetic storms (GAL-OS-IONO, 2016).

4.1.4.3. IRI - INTERNATION REFERENCE IONOSPHERE

IRI was initiated by the Committee on Space Research (COSPAR) and the International Union of Radio Science *(URSI)* in 1969, since then it has been steadily improving with newer data and better modeling techniques leading to the release of several key editions of the model since (Rawer et al., 1978), until *IRI*-2016 (Bilitza et al., 2017). *IRI* is a joint work of many researchers from all over the world and has been recognized as the climatological standard model by the International Standardization Organization *(ISO)* since 2009 (Bilitza et al., 2011).

At the actual development stage *IRI* has the capability to provide real-time ionospheric weather conditions based on the ingestion of real-time measurements like ionosonde-derived peak parameter values, that can be used besides other ionospheric physical components to obtain the N_e and the corresponding electron content, for a given location and epoch and along any desired ray-path. For more details about I*RI* and the scope of its application please refer to Bilitza et al. (2017).

4.2. DCB POST-FIT TO IONOSPHERIC TEC

There are some examples in the literature that describe how to perform *DCB* estimation after the deduction of ionospheric *TEC.* For instance, Ma and Maruyama (2003), knowing beforehand the *sDCB* tried out a series of receiver bias candidates to find out the minimum *TEC* standard deviation of all *rDCB* trial values, based on pre-computed *VTEC* results acquired from Japan *GEONET* grid. Arikan et al. (2008), also with *sDCB* beforehand knowledge, applied the post-fit approach for single *rDCB* estimation based on the *IGS GIMs VTEC* differences with a *de-noised CCL* measurements, obtained from each station. Montenbruck et al. (2014), with a two-step approach for *DCB* post-fitting to *TEC,* was able to determine *sDCB* and *rDCB* for *GPS*, *Galileo*, and *BeiDou,* using only pseudorange observations and *IGS GIM's*.

Currently there are seven *IAACs* producing their own *GIMs*, applying different datasets and modeling techniques (see Tab. 1 and Fig. 12) and each of them resulting in different levels of accuracy (Wielgosz et al., 2021). Namely, the Chinese Academy of Sciences *(CAS)* (Li et al., 2015); the Center for Orbit Determination in Europe *(CODE)* (Schaer, 1999); the European Space Agency *(ESA)* (Feltens, 2007); Jet Propulsion Laboratory *(JPL)* (Mannucci et al., 1999); Natural Resources Canada *(NRCan)*

(Ghoddousi-Fard et al., 2011); Universitat Politècnica de Catalunya (UPC) (Hernández-Pajares et al., 1999) and Wuhan University *(WHU)* (Zhang et al., 2013).

Tab. 1 – The International *GNSS* Service (*IGS*) and Associate Analysis Centers (*IAAC's*) algorithm strategies for Global Ionospheric Mapping (*GIM*), adapted from Roma-Dollase et al. (2018) and Wielgosz et al. (2021).

IAAC	Measurment	Spatial Structure	Adjustment	Geometry / Functions	Interpolation	DCB Strategy	Time	Start Date	References
IGSG	Combined	Single Layer (SL) - 2D	-	Combined	Weighted Mean	Simultaneously to VTEC	2h	1998.4	(Hernández-Pajares et al., 2009)
CASG	Carrier to Code Levelling (CCL)		Least-Squares (LSQ)	SH and GTS	-		2h/0.5h	2016	(Li et al., 2015)
ESAG				Spherical Harmonics Expansion (SH)			2h	1998.4	(Feltens, 2007)
EMRG							1h	1998.4, 2015.3	(Ghoddousi-Fard et al., 2011)
WHUG			Ineq. Const. LSQ				2h	2016	(H. Zhang et al., 2013)
CODG		Modified SL - 2D	LSQ				2h/1h	1998.4	(Schaer, 1999)
JPLG		3 Layer Shell - 3D	Kalman	Spherical Triangle Tiles	Splines		2h		(Mannucci et al., 1999)
UPCG	Carrier Only	2 Layer Voxel - 3D		Tomographic		Post-fit to VTEC			(Hernández-Pajares et al., 1999)

ESAG new 3D model is not yet operational.

In conclusion of this section (4) fully dedicated to the techniques used for *DCB* estimation with ionospheric models, a summary of the advantages, disadvantages and obtained values for the estimation methods according to Liu et al. (2020) is given in Tab. 2.

Tab. 2 – Summary of DCB estimation methods according to Liu et al. (2020)

Methods	Hardware calibration	Global/Regional simultaneous estimation of TEC and DCB	DCB estimation after deduction Ionospheric TEC
Advantage	Simple operation	Improved accuracy of observations; Avoid the determination of ambiguity parameters;	DCB estimation in the individual epochs;
Disadvantage	Long update time, low reliability	Estimating DCB as daily constants; Evident leveling errors when DCB has significant short-term variations or severe multipath effects;	High dependence on the ionospheric model;
Obtained Value	rDCB; sDCB	rDCB+sDCB;	rDCB+sDCB;

5. METHODOLOGY

5.1. DATASET AND RECEIVER LOCATION

Two months (July-August) of ionospheric observations from Day Of the Year (*DOY)* 182 to 243 of 2019, in Açores and Madeira region (Fig. 20), were collected during the *24th* Solar Cycle minimum. The ground station coordinates, receiver models and antenna types used in the adjustment procedure are defined in Tab. 3. The number of valid processed measurements with a minimum elevation mask of 10° and three satellite in view for the reference Furnas (FRNS) station are *17 752*. The data decimation used was five minute epochs of five seconds observations (cycle slip corrected), on *GPS* frequencies L_1 and L_2, using both carrier-phase and pseudorange measurements, for highly precise uncalibrated ionospheric observations obtained with the Carrier-to-Code Levelling procedure (Eq. 27).

Tab. 3 – Açores and Madeira stations coordinates and description from the national network of *GNSS* receivers (*ReNEP*), used for *rDCB* reference offset estimation, at the reference FRNS station and *rDCB* calibration process application to TERC, FLRS and FUNC stations.

Station	Latitude	Longitude	Elipsoid Altitude	Receiver	Antenna
Furnas (FRNS)	37º 46´09.59755´´N	25º 18´29.56028´´W	275.330 m	Leica GX1230GG	Leica AX1202GG
Terceira (TERC)	38º 43´08.36667´´N	27º 09´10.78006´´W	408.900 m	Leica GX1200GG Pro	Leica T504GG
Flores (FLRS)	39º 27´13.79713´´N	31º 07´35.00117´´W	79.918 m	Leica GRX1200GG Pro	Choke-Ring Leica AT504GG
Funchal (FUNC)	32º 38´52.60577´´N	16º 54´27.41982´´W	78.497 m	TRIMBLE Alloy	TRIMBLE GNSS-Ti Choke Ring

An important note to make, is that all the data results, except for the calibration phase itself, are related to Furnas (FRNS) reference station, since it was the only available dataset to work with and refine the adjustment strategy for different time intervals and elevations masks. Moreover, similar to the day-to-day and intra-day variation for *rDCB* estimation results, as computed for the reference station, the adjustment results for the other stations are provided in the Appendix (10,11 and 12) for comparison.

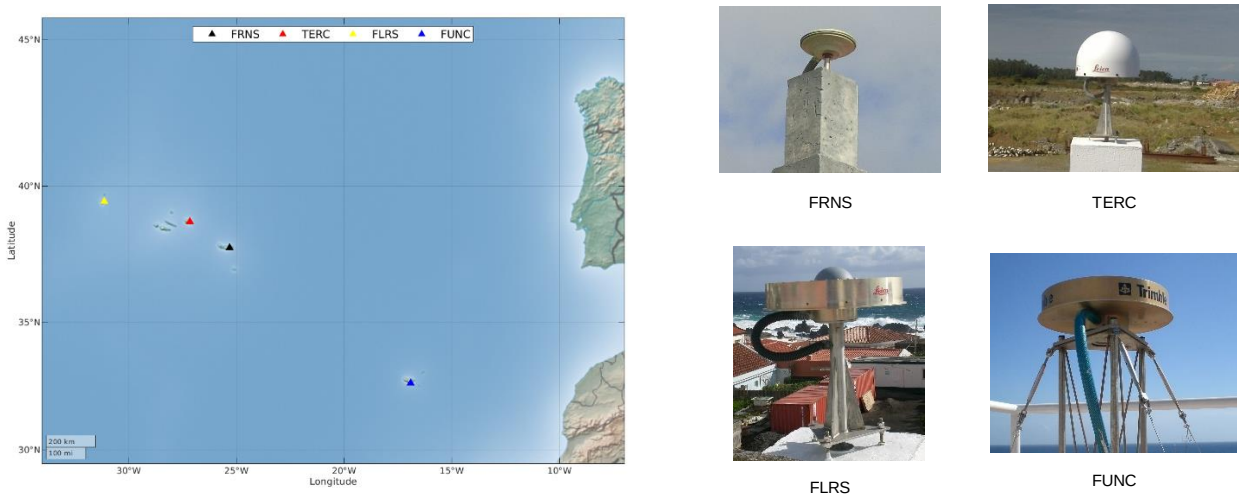

Fig. 20 – Açores and Madeira stations location and respective receiver antennas from ReNEP website.

5.2. RECEIVER DCB ESTIMATION WITH NEQUICK IONOSPHERIC MODELS

According to Ciraolo et al. (2007), Rovira-Garcia et al. (2016) and Nie et al. (2018), combining (Eq. 27) with (Eq. 20), provides precise ionospheric *STEC* measurements though uncalibrated. Therefore, considering $sP_I = L_I - \bar{B}_I = I + K_{21} + \varepsilon_{SP_I}$, where $I = (\alpha_2 - \alpha_1) \cdot STEC = \alpha \cdot STEC$, and $\alpha_f \cong \frac{40.3}{f^2} 10^{16}\, m/TECU$, *f* in (Hz), for GPS L_1 and L_2 case, $\alpha \cong 0.105\ m/TECU$ and neglecting noise and residual multipath effects (ε_{SP_I}) due to levelling errors in the order of 1.5 *TECU RMS (*Rovira-Garcia et al., 2016)*,* we can convert the previous ionospheric observable from meters to *TEC* units by taking $sP_I = 0.105 \cdot STEC + K_{21}$ and dividing entirely by $\alpha \cong 0.105\ m/TECU$, to obtain $9.524 \cdot sP_I = STEC + 9.524 \cdot K_{21}$, and re-written as

$$sP'_I = STEC + K'_{21} \quad \text{(Eq. 40)}$$

where sP'_I, represents the uncalibrated *CCL* ionospheric observable between each *rcv-sat* ray-path*,* in *TECU*, K'_{21}, is the receiver plus satellite *DCB* also in *TECU* and *STEC,* the ionospheric electron content to be modelled according to each epoch and *rcv-sat* ray-path.

For simultaneously *TEC* and *rDCB* retrieval a test for every possible bias combined with an array of effective ionization (*Az*) models is calculated, until the best fit between the uncalibrated *CCL* measurements (sP'_I), the K'_{21}, and the modelled STEC is achieved (Fig. 21). The adjustment / fit procedure is accomplished when the minimum sum of the chi-square differences (χ^2) between *m* ray-path measurements plus the pre-defined trial bias interval and a set of Az models is acquired, according to the following expression for each epoch

$$[\min[\chi^2(t)]]_{t=\{1,n\}} = \left[\min \sum_{j=1}^{m} \left[\left(STEC^j_{r,test}\left(t, b_{(i)}\right) - STEC^j_{r,mod}(t)\right)^2\right]\right]_{t=\{1,n\}} \quad \text{(Eq. 41)}$$

where, *t* is the epoch of interest, *n* is the total number of epochs from the time-series, *m* is the number of satellites in view at epoch *t*, *j* is the *PRN* number, *r* is the receiver and, $STEC^j_{r,test}\left(t, b_{(i)}\right)$ and $STEC^j_{r,mod}(t)$, will be given as follows

$$STEC^j_{r,test} = sP'_I - K'_{21} = sP'_I + sDCB^j - rDCB \quad \text{(Eq. 42)}$$

Considering $sP'_I + sDCB^j$ equivalent to the semi-calibrated ionospheric observable ($STEC_{sc}$), we then have

$$STEC^j_{r,test} = STEC_{sc} - rDCB \quad \text{(Eq. 43)}$$

Making the $rDCB = rDCB(t, b_{(i)})$, where b_i is the trial *rDCB* (in *TECU*) to be tested, according to the defined interval given by $b_{(i)} = \{\min(rDCB), \max(rDCB)\}$, where, $i = (\max(rDCB) - \min(rDCB))/p$, with *p* being the precision (in *TECU*) and *i* the number of (b_i) values to test. Thus

$$STEC^j_{r,test}(t, b_{(i)}) = STEC^j_{r,sc}(t) - rDCB(t, b_{(i)}) \quad \text{(Eq. 44)}$$

In turn, since $STEC^j_{r,mod}(t)$ will be dependent of *NeQuick-G Az TEC* models, we can express them as

$$STEC^j_{r,mod}(t) = STEC^j_{r,Az_k}(t) \quad \text{(Eq. 45)}$$

where, $STEC^j_{r,Az_k}(t)$ dependence for each *rcv-sat* pair and epoch is acquired as function of

$$STEC^j_{r,Az_k}(t) = f(t, \theta, \phi, h, a_{i,k}) \quad \text{(Eq. 46)}$$

where, *t* is the epoch (for month of year and hour of the day in *UTC*), θ, ϕ, h, are the rcv and sat geodetic coordinates of latitude, longitude, and height, respectively, and $a_{i,k'}$ are the *Az* coefficients to compute according to the following expression

$$[a_{i,k}] = f_{p_k} \cdot [a_0, a_1, a_2] \quad \text{(Eq. 47)}$$

where, a_0, a_1, a_2, are the constant initial values that will be affected by a series expansion factor (f_{p_k}) for integer Az_k values retrieval as follows,

$$f_{p_k} = f_{p_0} + (k-1)^r, \text{ with } \begin{cases} f_{p_0} = Az_{min}/(a_0 + a_1 \cdot \mu + a_2 \cdot \mu^2) \\ r = Az_p/(a_0 + a_1 \cdot \mu + a_2 \cdot \mu^2) \end{cases} \quad \text{(Eq. 48)}$$

where $k = 1, .., n$, and $n = Az_p/(Az_{min} - Az_{max})$, being *n* the total number of *Az* models to acquire for each slant ray-path at epoch *t*, Az_p, the precision in *sfu* (solar flux units) desired, Az_{min} and Az_{max}, the minimum and maximum interval values of *Az* models, also in *sfu*, and μ, the receiver modip. Thus, substituting (Eq. 44) and (Eq. 45), into (Eq. 41) expands to

$$[\min[\chi^2(t)]]_{t=\{1,n\}} = \left[\min \sum_{j=1}^{m} \left[\left(STEC^j_{r,sc}(t) - rDCB(t, b_{(i)}) - STEC^j_{r,Az_k}(t)\right)^2\right]\right]_{t=\{1,n\}} \quad \text{(Eq. 49)}$$

where the semi-calibrated $STEC^j_{r,sc}(t) = sP'_I(t) + sDCB^j(DOY)$ in *TECU*, is the *CCL* ionospheric observable plus the *sDCB* daily broadcast.

The relevant results per *rcv-sat* configuration at epoch *t,* according to the $\min[\chi^2(t)]$ adjustment procedure will then be the *rDCB (t)* and the *Az(t)* model, with which the intra-day and day-by-day variation and all relevant statistical information can be evaluated.

From the experience acquired during the testing and results phase, two additional features were included in the algorithm, to address the mis-modelling effects that persisted despite the time of day or

elevation mask considered. Therefore, a cut-off *TEC* value of 3 *TECU* (~ 1 ns) for the $STEC_{r,test}^{j}\left(t, b_{(i)}\right)$ variable was added to minimize the interference of noise measurements, during the model adjustment at low / quite ionospheric activity periods (*e.g.*, dawn epochs). Another was to have the possibility to adjust the *Az* model not only for a single epoch *t,* but for any sum of epochs, by adjusting (Eq. 49) as follows

$$[\min[\chi^2(stp)]]_{stp=\{s,n/s\}} = \\ = min\left[\sum_{t=1+(stp-s)}^{stp}\left[\sum_{j=1}^{m}\left[\left(STEC_{r,sc}^{j}(t) - rDCB(t, b_{(i)}) - STEC_{r,Az_k}^{j}(t)\right)^2\right]\right]\right]_{stp=\{s,n/s\}} \quad \text{(Eq. 50)}$$

where, $s = w \cdot h/e$, with *e* being the minimum sampling data measurements (in our case five minutes), *h,* is a constant equivalent to one hour (expressed in the same units of *e*) and *w* is the time window of the sum of epochs to adjust in a single result (expressed in hours). The *stp* term, is the total number of sum of epochs given by *stp = n / s,* where *n* is the total number of five min epochs from the entire time-series.

5.3. ACCURACY / PERFOMANCE ASSESSMENT

For the performance assessment we can use the accuracy and precision achieved since we know beforehand the «true» *DCB* values of the reference receiver and all the other stations mentioned in Tab. 3, from previous direct calibrations. Therefore, computing the difference between the estimated *rDCB* mean of the reference station and its true value can then be used as a measured of accuracy for the adjustment procedure, according to the selected time interval and elevation mask and include the precision evaluation, by measuring the day-by-day and intra-day repeatability of the results.

While, for the calibration assessment, using the estimated *rDCB* mean difference of the reference station from its true value and then deducting it from the mean *rDCB* estimation results of the other stations (to be compared against their true values), enables the computation of the mean error calibration procedure in terms of precision and accuracy.

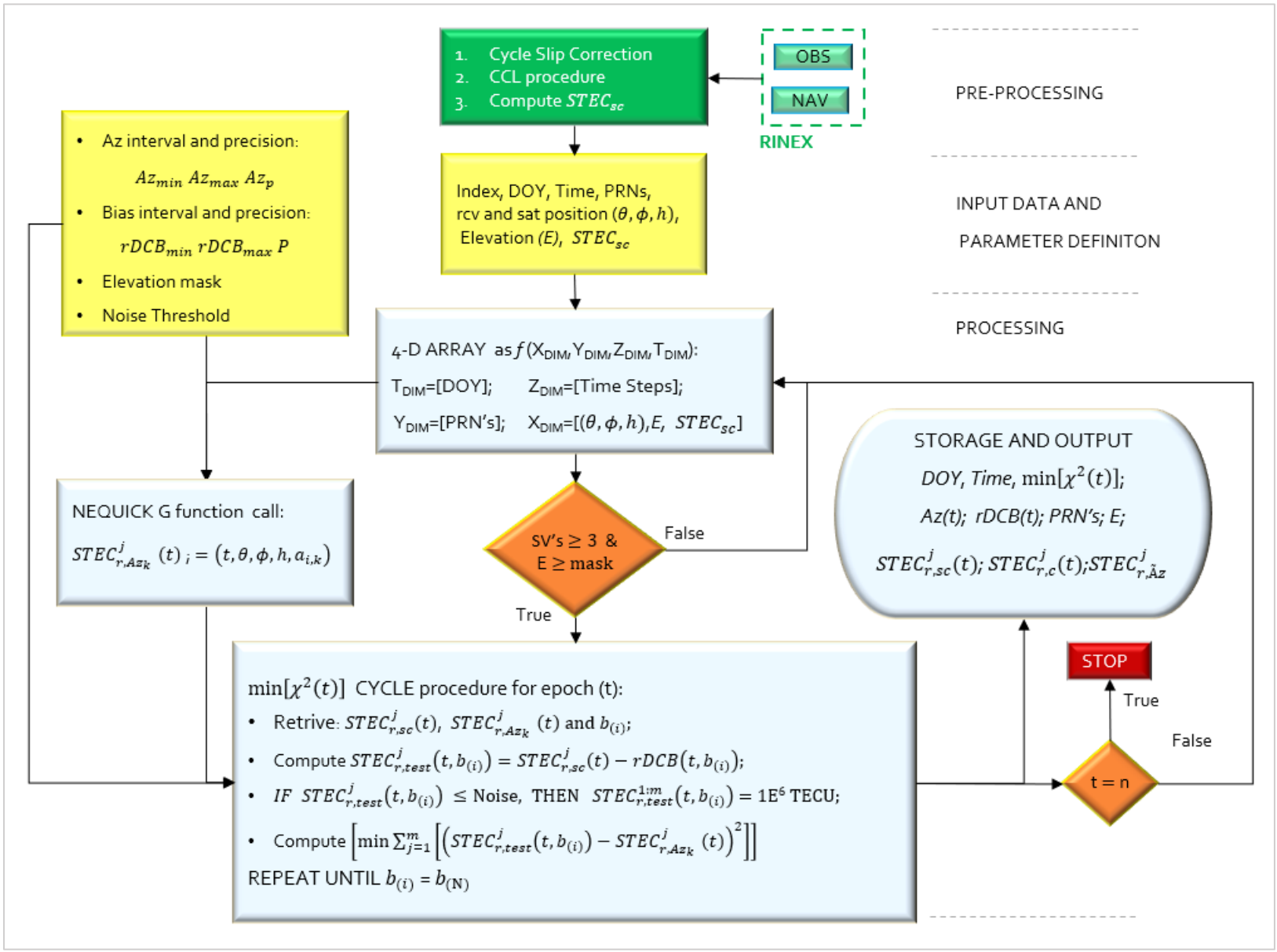

Fig. 21 – Algorithm flowchart with the pre-processing stage (in green), the user parameter definition and base data indexing before the processing stage in a *4-D* array (in yellow), the cycle processing stage associated with the $\min[\chi^2(t)]$ adjustment (in blue), and the conditions for entering and exiting each epoch adjustment cycle (in orange) until the end of the entire data processing is done (in red).

6. TESTING

6.1. SPATIAL-TEMPORAL ANALYSIS OF NEQUICK PREDICTIONS

Before exploiting the capabilities of *NeQuick-G* to predict the ionosphere state according to location, time and *rcv-sat* configuration, several worldwide and locally *STEC* predictions were done to understand the relations between *Az* models against *TEC* magnitude for several times of day, quantify mapping function conversion errors in single layer models and, finally, to assess the error of the $\min[\chi^2(t)]$ adjustment procedure based on simulated biased data.

6.1.1. CRITICAL TIMES FOR GLOBAL IONOSPHERIC ACTIVITY

Adopting *Az* moderate solar activity coefficients, according to annex E.2 of GAL-OS-IONO (2016), a_0 = 121.129893, a_1 = 0.351254133 and a_2 = 0.0134635348 for *VTEC* values acquisition in a worldwide grid, the highest ionospheric activity detected was found to be around 07th hour *UTC* of the 10th month, generally in the north hemisphere and in particular on the Eastern Asia / Pacific western region (Fig. 22), whereas, the lowest activity was found to be around the 13th hour UTC of the 7th month, generally at the south hemisphere and in particular on the Indian-Pacific region (Fig. 23).

6.1.2. CRITICAL TIMES FOR AÇORES LOCAL IONOSPHERIC ACTIVITY

Similarly, applying the same *Az* coefficients for the Açores region, centered at Furnas reference station (modip (*u*) of 46.38º) the *VTEC* values for each hour of the day and every month of the year revealed that the highest ionospheric activity for this region was at the 15th hour *UTC* of the 4th month (Fig. 24), while the lowest activity was found to be at the 6th hour *UTC* of the 1st month (Fig. 26).

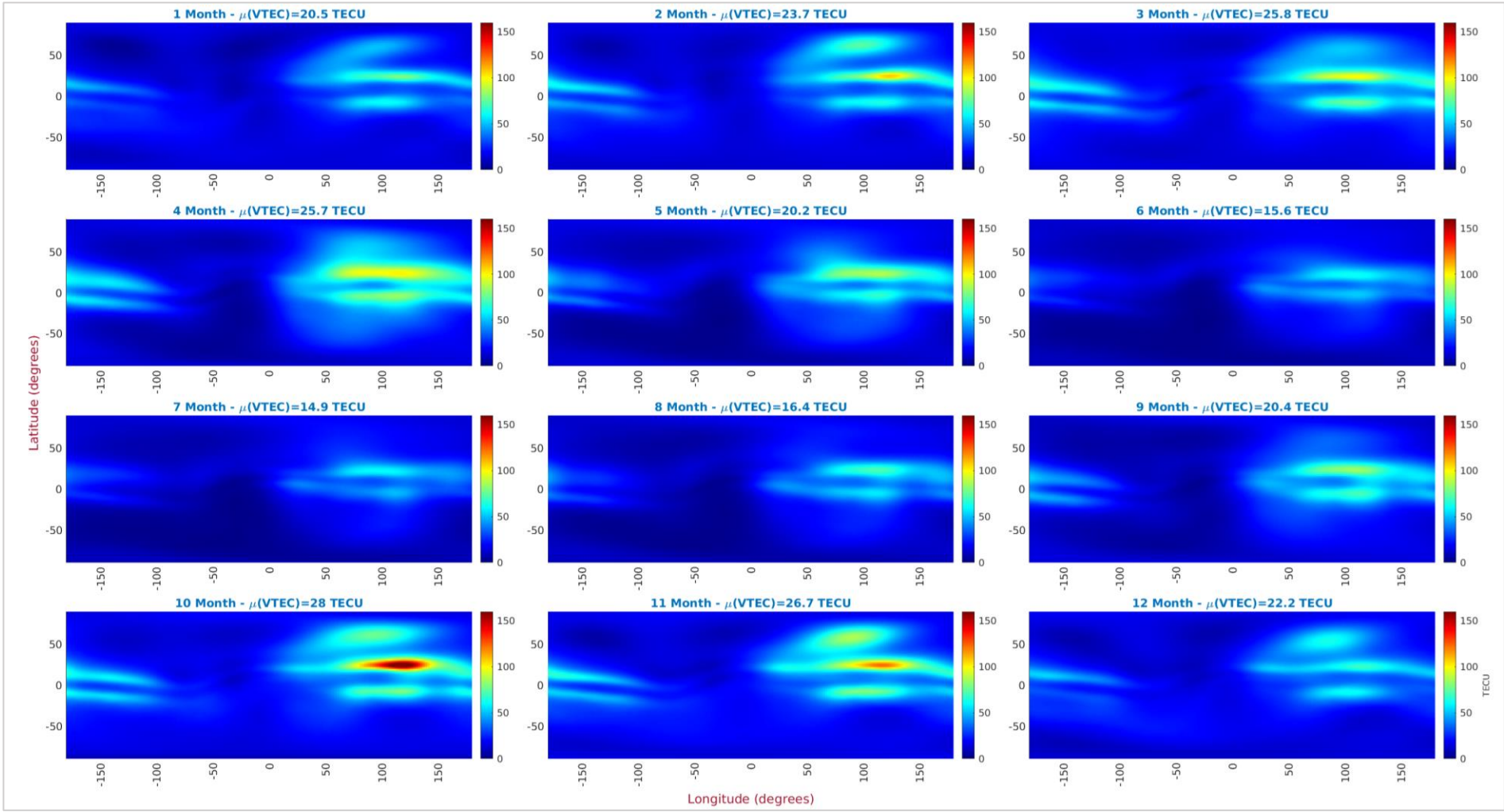

Fig. 22 – Monthly *VTEC* prediction using *NeQuick G* moderate solar activity coefficients, a_0 = 121.129893, a_1 = 0.351254133 and a_2 = 0.0134635348, (annex E.2 of GAL-OS-IONO (2016)), for global ionospheric activity, monthly mean (in the top of each tile) with highest annual mean at the 07th hour *UTC* of the 10th month.

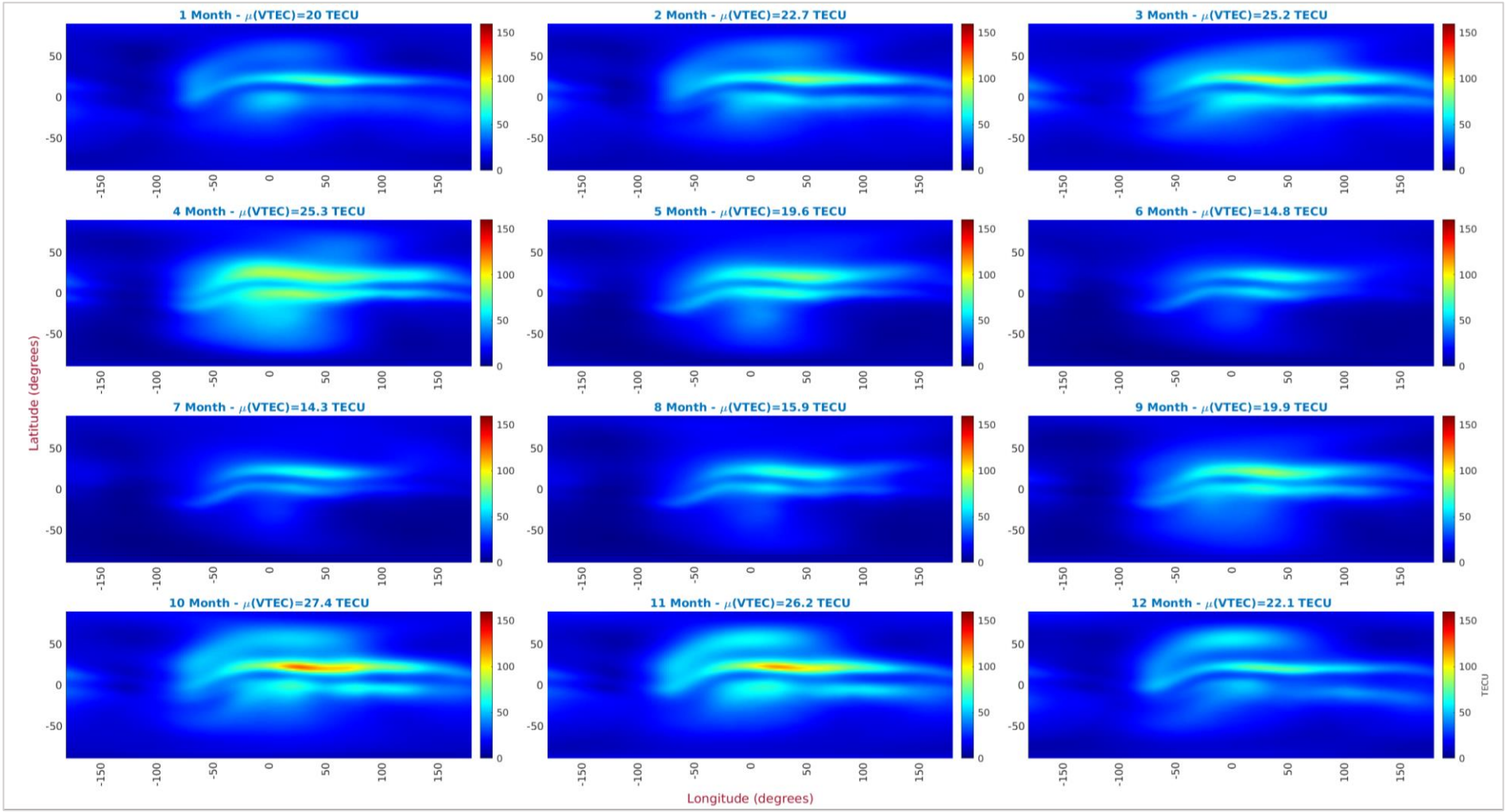

Fig. 23 – Global ionospheric activity for the same solar activity coefficients of Fig. 22, where the lowest monthly *VTEC* mean value is found to be at the 13th hour *UTC* of the 7th month.

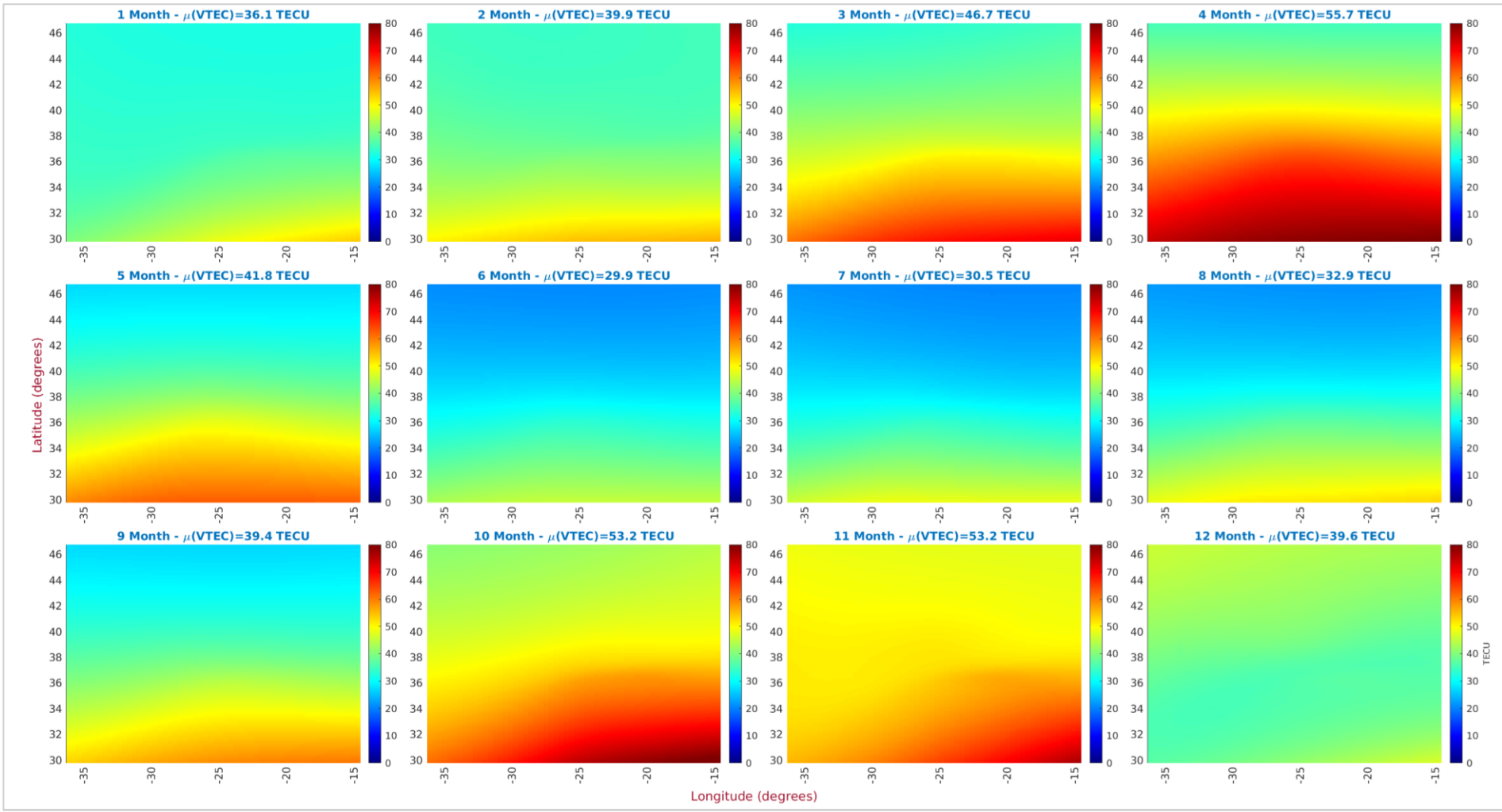

Fig. 24 – Açores local ionospheric activity prediction for the same solar activity coefficients of Fig. 22, where the highest monthly *VTEC* mean value is found to be at the 15th hour *UTC* of the 4th month.

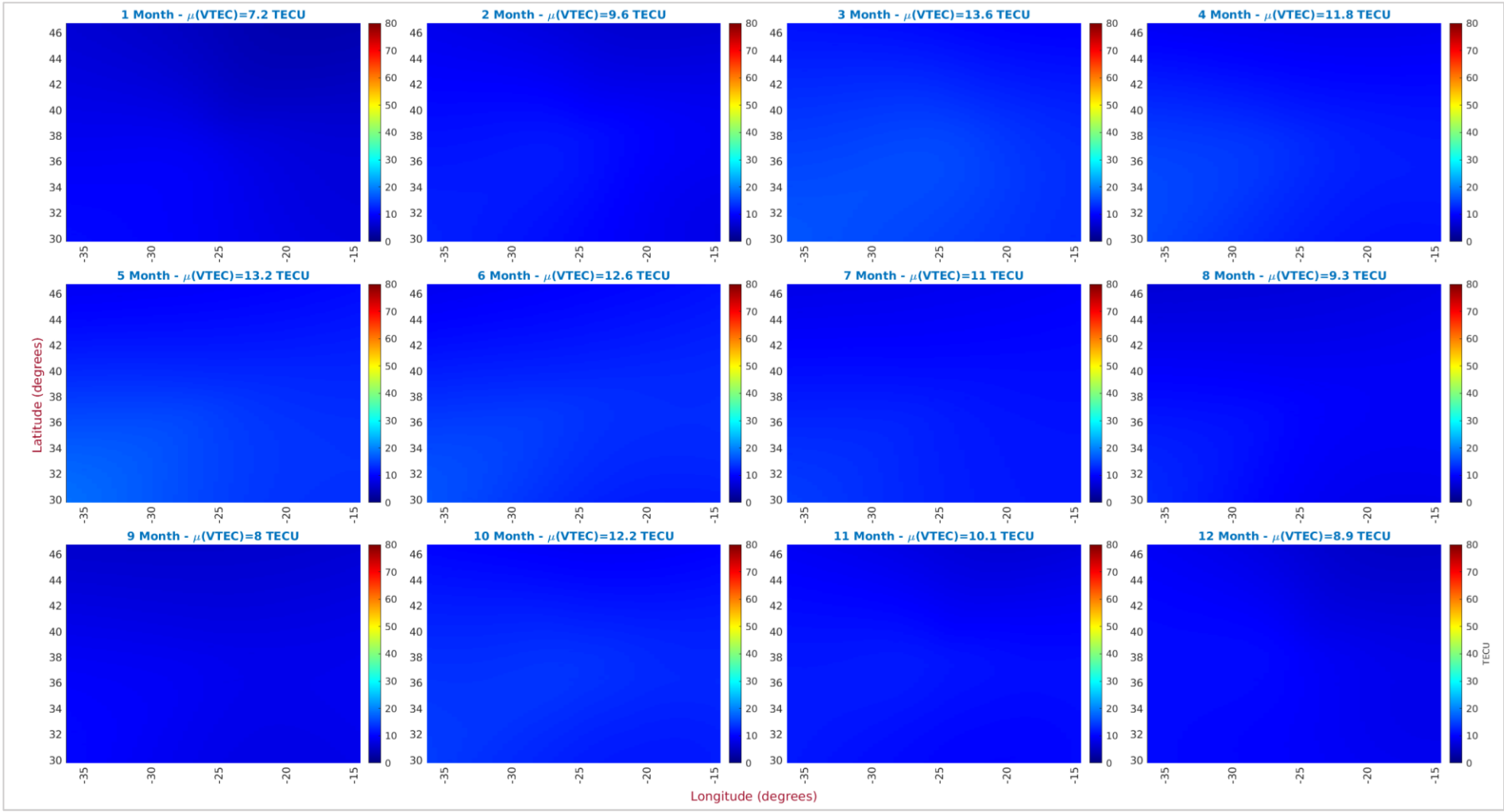

Fig. 25 – Açores local ionospheric activity prediction for the same solar activity coefficients of Fig. 22, where the highest monthly *VTEC* mean value is found to be at the 06th hour *UTC* of the 1st month.

6.2. EFFECTIVE IONIZATION MODELS FOR TEC IN AÇORES REGION

An illustration of the *VTEC / STEC versus Az* curves (*VTEC* only at receiver station zenith) using a uniform distribution of *IPP's* intersection at 450 km layer height for representation purposes and *STEC* estimation, according to a predefined interval of *Az* models, varying from 1 sfu to 200 sfu, considering the Açores previous estimated high and low solar activity times of the day and several elevations angles and azimuths, is shown in Fig. 26.

According to Fig. 26, the *TEC* magnitude values are highly dependent and inversely proportional to the elevation angles and notably high during direct sun irradiance hours than pre-dawn hours, with significant dependence on the azimuth relation with sun position or hour of the day. Moreover, the high potential for mis-modelling of *Az* values should be noted during the pre- and dawn hours, where small *TEC* variation between 1 to 2 *TECU* can represent in the zenith case, a model variation around 40 to 80 *sfu*, respectively. Or, in the case of the 30º elevation angle, with the *rcv-sat* ray-path in the Eastern quadrant, an equal variation (1-2 *TECU*) can generate a mis-modelling of 20 to 40 *sfu*, respectively. Indeed, additional evidence of mis-modelling effects occurs in the South-Eastern ray-path quadrant, when low elevation angles as 10º can detect *TEC* values smaller than the zenith *TEC*, for any *Az* model below 40 *sfu*, which may seem unexpected.

Acknowledging the *Az* modelling behavior during quiet periods highlighted the need to adopt mitigation strategies for the adjustment procedure, since for low TEC variations unavoidable mixed with receiver noise measurements, will clearly affect the accuracy of the results during those time periods.

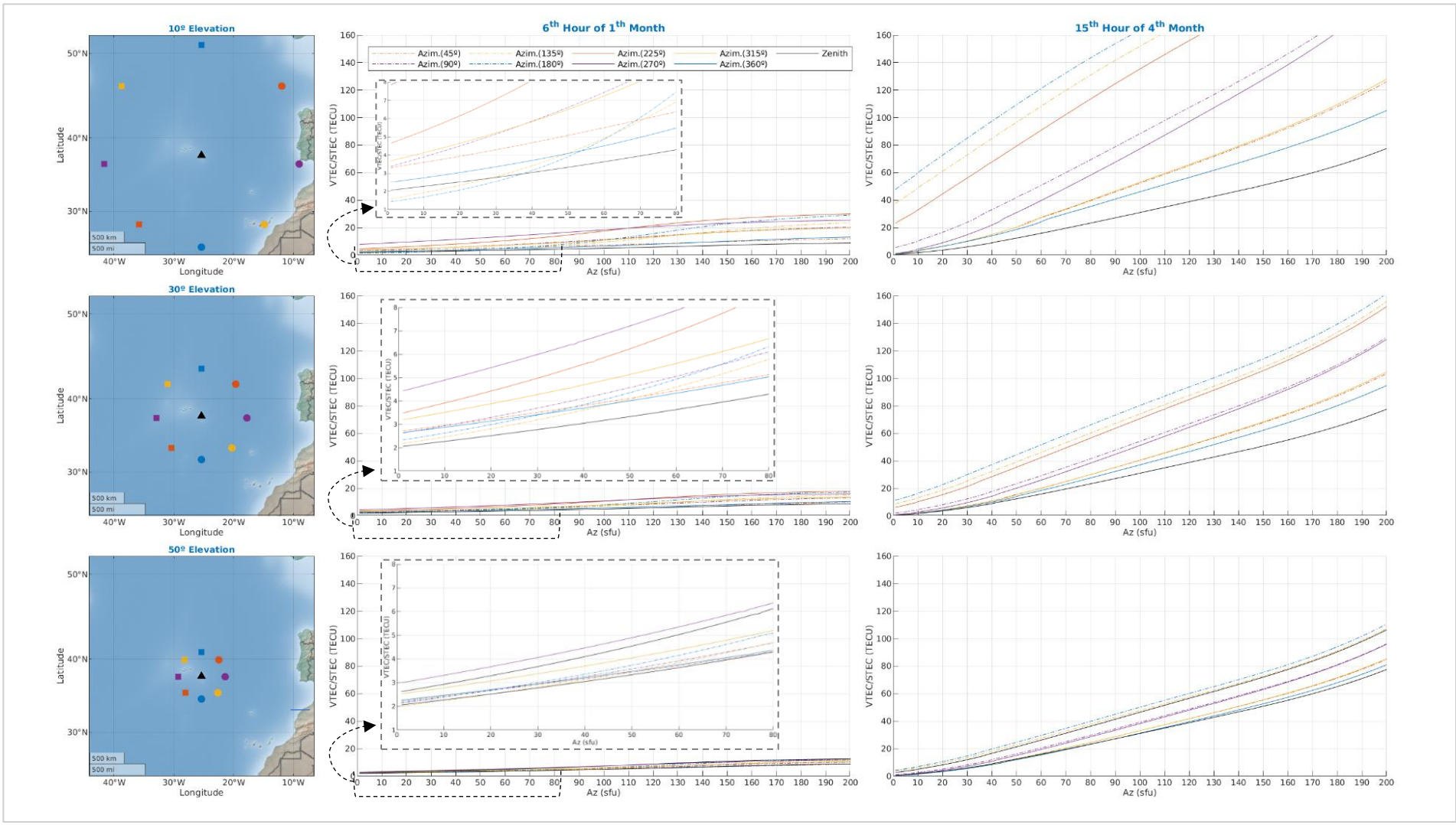

Fig. 26 – *NeQuick-G Az* models for *TEC* prediction at Açores region (*u* of 46.38º) using multiple elevations angles (10, 30, 50 and 90º) and azimuth's (45, 90, 135, 180, 225, 270, 315, 360º) at 6th hour *UTC* of 1st month (lowest activity period) and 15th hour *UTC* of 4th month (highest activity period). A zoom for *TEC* values against *Az* models is given inside a dashed-box presented over the lowest activity period. *IPP's* are represented at a 450 km layer height.

6.3. MAPPING FUNCTION CONVERSION ERRORS

Proceeding with the advantage for *NeQuick-G* to provide *TEC* predictions at any location and any *rcv-sat* ray-path, the magnitude and spatial distribution of the mapping function (Eq. 30) conversion errors are illustrated for a mid-latitude region (at Açores) in Fig. 28, adopting moderate solar activity conditions for two critical times of day and using all the combined elevation and azimuth angles between [10 to 90º] and]0-360º], respectively, for a single layer model at 450 km height.

All the *IPP VTEC* values located between a virtual receiver and a virtual satellite at the zenith (*VTEC* reference values), are shown 2nd column tiles of Fig. 28. Conversely, in the 3rd column tiles of Fig. 28, the *STEC*-to-*VTEC* values for each *IPP* is calculated using the mapping function (Eq. 30) and finally, in the 4th column tiles, the differences between the mapped and reference *VTEC* values for each critical time of the day is computed.

According to the overall results an amplified *VTEC* error difference in the North-South axis, if compared with East-West axis, is visible at the highest solar activity time, although fading during the lowest activity period. Moreover, the bias along the North-South axis reveals that mapped *VTEC* values at the North quadrant are lower than the reference *VTEC* values and, inversely, in the South quadrant are higher than the reference values. The root mean square error (*RMSE*) was 3.31 *TECU* and 0.65 *TECU*, for the highest and lowest activity period, respectively. While the relative *RMSE* was 5.8% and 8.3%, highest and lowest activity period, respectively. Meaning that absolute *VTEC*-to-*STEC* (and *vice-versa*) conversion errors are higher during high solar activity periods, although with higher weight in the lower activity periods.

Intending to acquire a wider view of the mapping function conversion errors throughout the entire day and different layer heights (350 km and 450 km), using all combined elevation and azimuth angles and a moderate solar activity, in Fig. 29 and Fig. 30 an illustration of the magnitude and spatial distribution of the conversion errors is given for the 350 km and 450 km layer heights, respectively . Similarly, to what seen before in Fig. 28, the North-South axis bias remains with special evidence during the day period, independently of the layer height. Also, the magnitude of the conversion errors increased from 6 *TECU* to 10 *TECU* due to a higher degradation of *STEC*-to-*VTEC* conversion at 350 km layer height.

Finally, a summary plot with the results according to the layer height is shown in Fig. 27, for the mean error (μ(*E*)), the RMSE, and the relative RMSE (RRMSE). The layer at 450 km height provides lower conversion errors than a layer at 350 km, with a minimum *RMSE* around 0.80 and 1 *TECU* and a maximum around 3.31 and 5.50 *TECU*, for the 450 and 350 km layer heights, respectively. Notable, is the mean error oscillation of the 450 km layer height around 0 *TECU* value, while the 350 km layer is

mostly around -1.5 *TECU*. Clearly, in the case of the single layer model adoption for *STEC*-to-*VTEC* conversion (and *vice-versa*) the 450 km layer height outperforms the 350 km layer.

The aforementioned mapping function conversion errors have been highlighted, for instance, by Hernández-Pajares et al. (1999), when he referred that for a fixed ionospheric height the whole ionosphere could induce errors ranging from a few TECU at middle latitudes up to *10* TECU or more, in the equatorial regions.

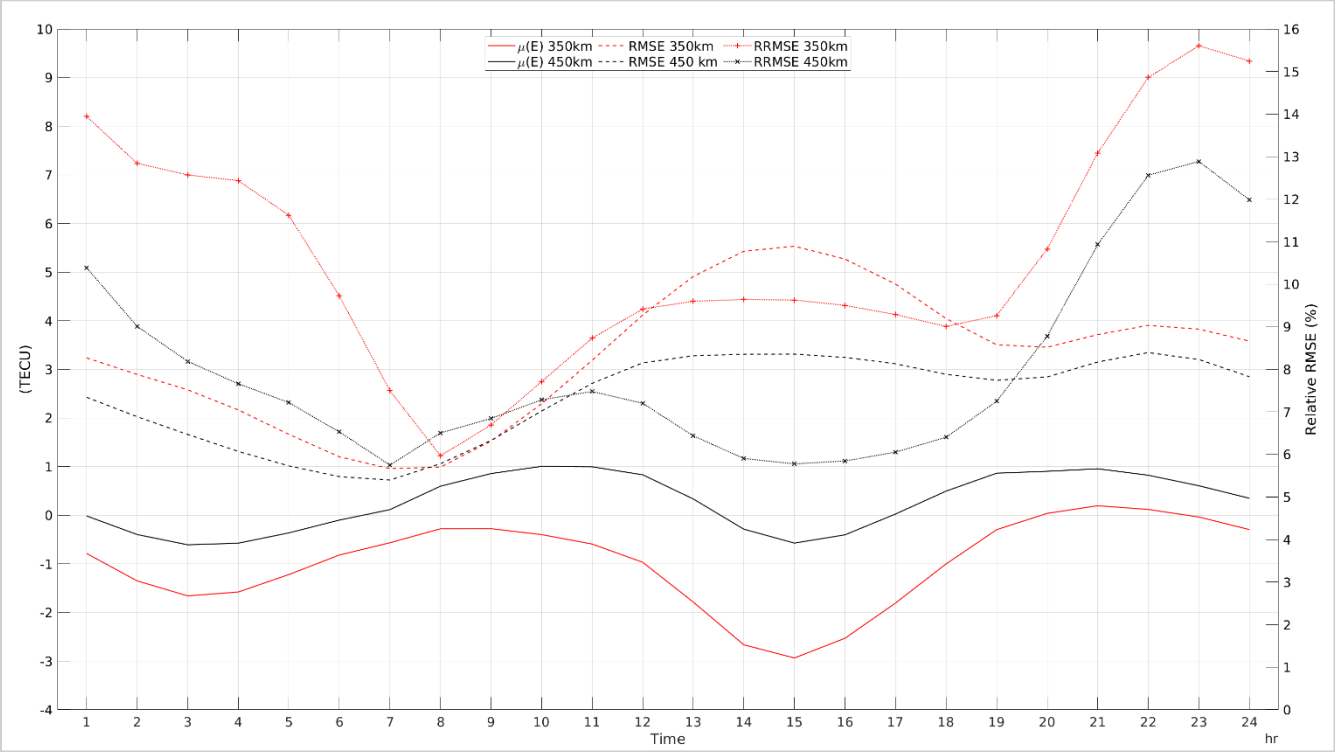

Fig. 27 – Intra-day mapping function conversion errors for the 4th month of the year, at Açores region (centered at 37N,25W), considering moderate solar activity coefficients as referred on Fig. 22 and two fixed layer heights at 350 and 450 km.

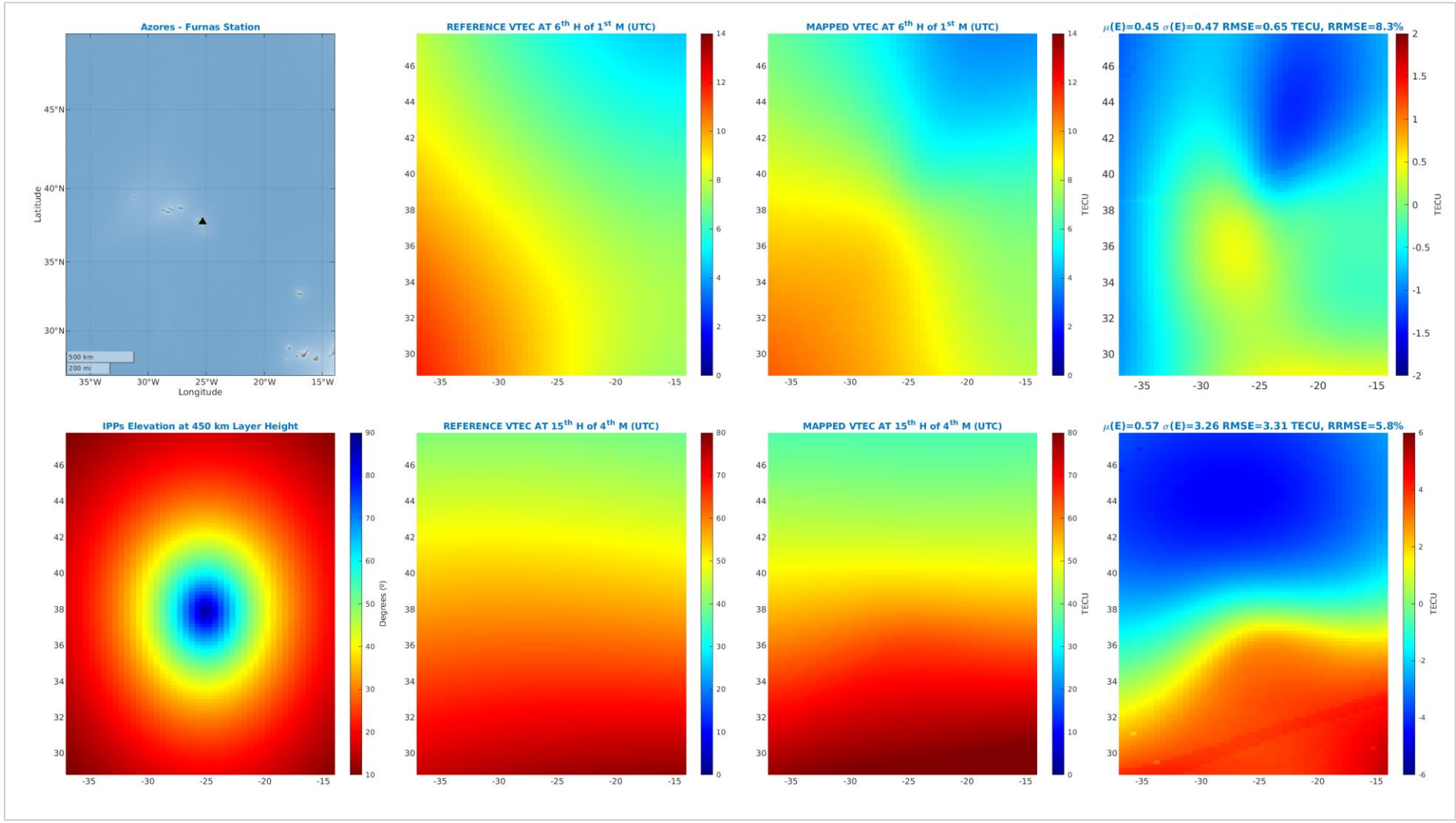

Fig. 28 – (For a 2 x 4 mosaic) in [1,1] Furnas receiver location; in [2,1] IPP's at 450 km layer height; Reference *VTEC* values in [1,2] (6 hr / month 1) and in [2,2] (15 hr / month 4) *UTC*; Mapped *VTEC* for hours and months of [1:2, 2]; Mapped minus reference *VTEC* in [1, 4] (6 hr / month 1) mean error of 0.45 *TECU* and standard deviation 0.47 *TECU*; Mapped minus reference *VTEC* in [2, 4] (15 hr / month 4) mean error of 0.57 *TECU* and standard deviation 3.26 *TECU*. Notice the different scales of the color bars (for low and high activity). Moderate solar coefficients as used in Fig. 22.

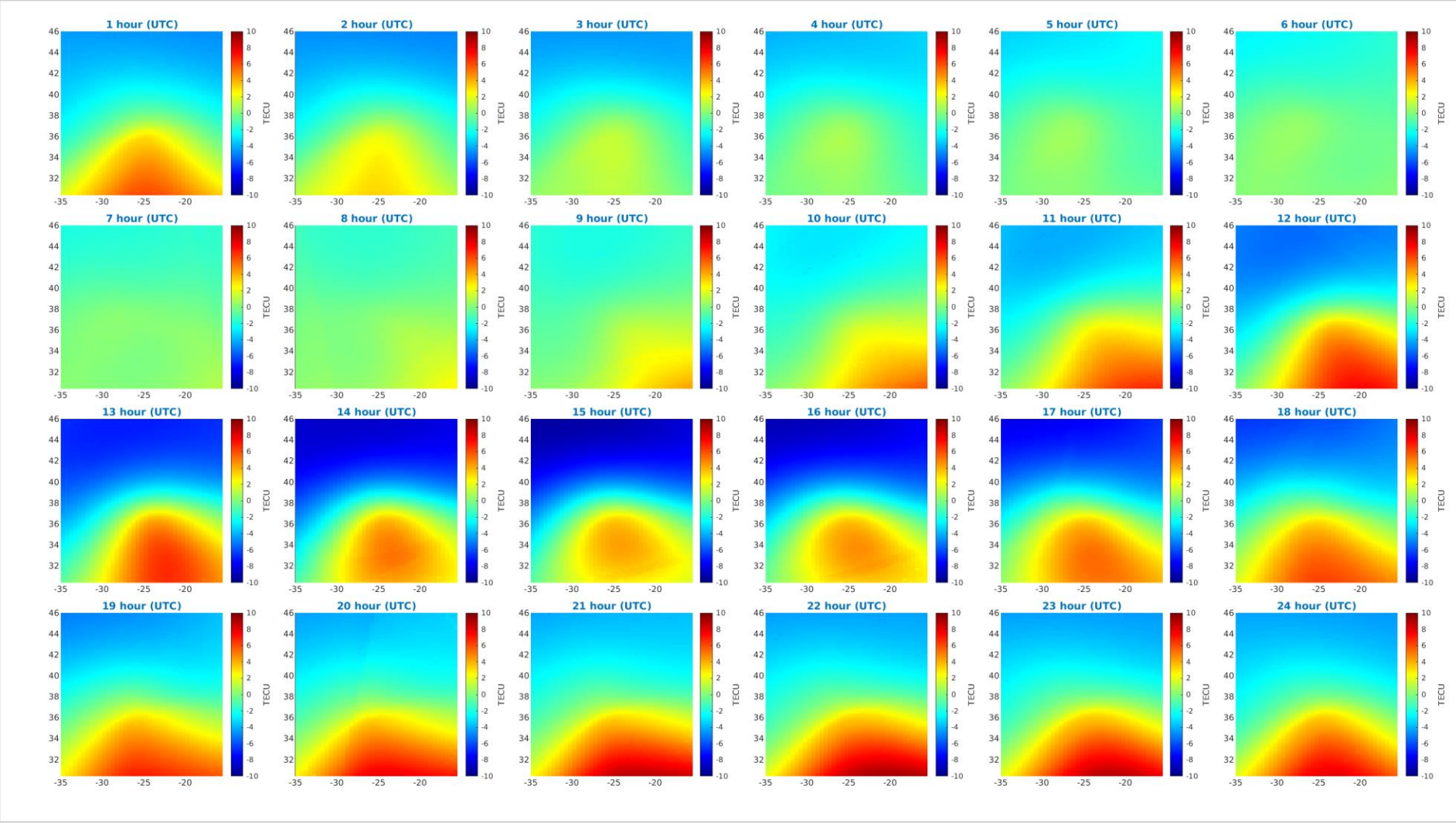

Fig. 29 – 24 hours mapping function conversion errors for a 350 km layer height centered at Furnas receiver location (37.769 N, 25.308 W, 0.276 km). Moderate solar coefficients as use in Fig. 22.

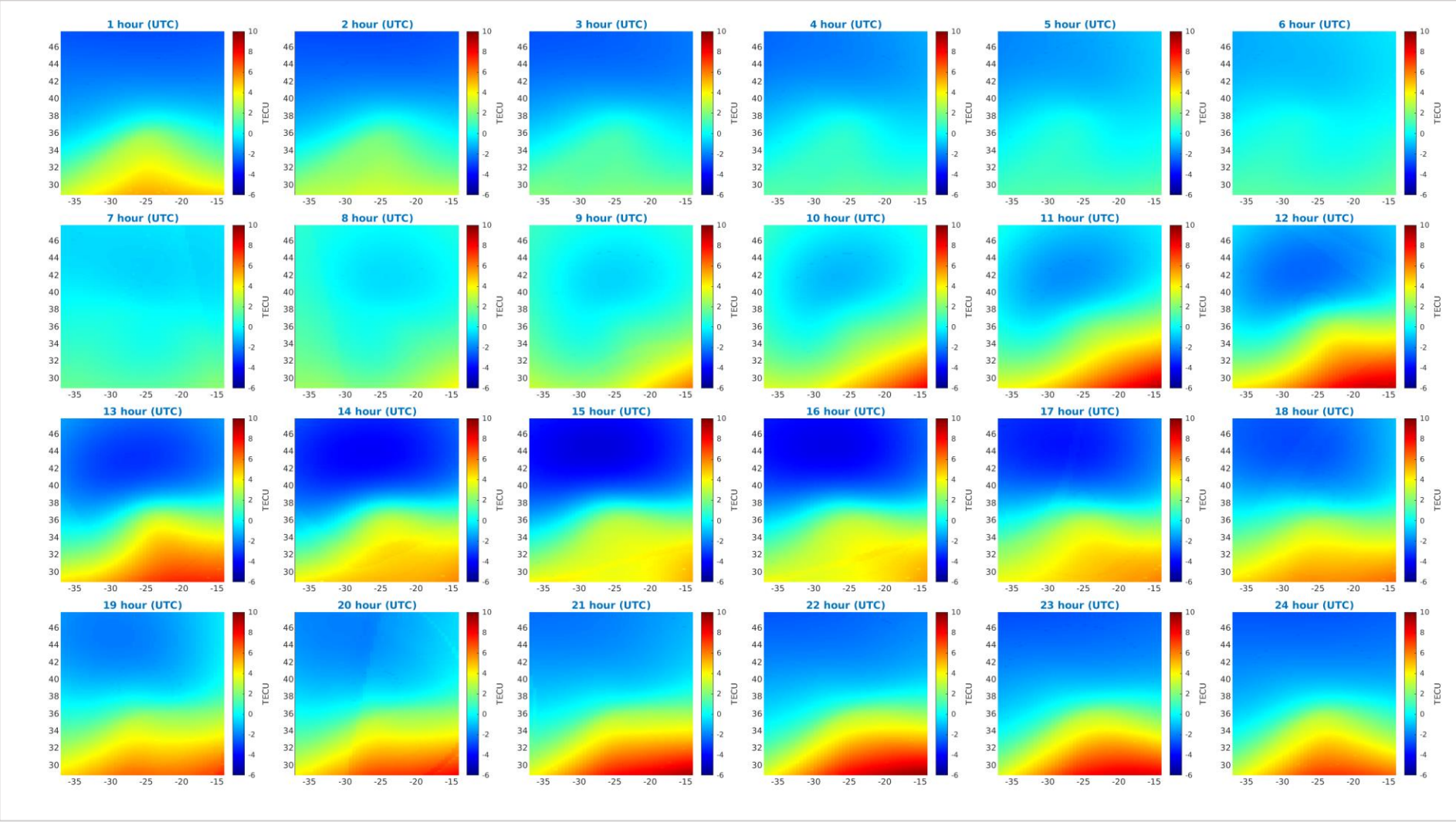

Fig. 30 – 24 hours mapping function conversion errors for a 450 km layer height using the same assumptions and parameters of Fig. 29.

6.4. ERROR ASSESSMENT WITH SIMULATED DATA

6.4.1. THE MONT CARLO APPROACH

The general principle for the simulation resorts to a pre-selection of *Az* base models (Az_0) to test the procedure adjustment accuracy and precision based on well-known *STEC* values attributed to each *rcv-sat* ray-path, plus an added gaussian random distributed *TEC* error and a constant bias.

6.4.1.1. ONE SINGLE BIAS

Knowing precisely the *STEC* values to expect for each *Az* model and *rcv-sat* configuration, the first test was to identify a pre-selected bias value, during two critical times of the day (15th hr of month 4 and 6th hr of month 1), with an additionally stress condition for *TEC* differentiation of the highest activity time from the lowest, by setting Az_0 model of 100 *sfu* for the 15th hour and 45 *sfu* for the 6th hour.

According to Fig. 31 and Fig. 32, it's possible to observe that for a simulated bias of -18 *TECU* and - 1 *TECU,* at the highest and lowest activity periods, respectively, the $\min[\chi^2(t)]$ adjustment was able to accurately identified the initial bias and the Az_0 model initially used to simulate the observations.

The interval and precision of the bias vector in this example was between -30 to 30 *TECU* and 1 *TECU*, respectively, which equates to 61 tested biases. In turn, the interval and precision of the *Az* model vector, was between 1 and 150 *sfu* and 1 *sfu*, respectively.

Notably, as highlighted in 6.2 for the lowest ionospheric activity time of day (Fig. 32) it is remarkable how small *TEC* variations (in this case, 1 *TECU*), equates to a significant variation in the estimation of the correspondent *Az* model.

6.4.1.2. 1 000 GAUSSIAN RANDOM ERRORS

For the following test scenario, a similar search strategy as described before adopted, although instead of a single bias it consists of four groups of 1 000 gaussian random errors introduced into pre-selected $STEC_0$ values obtained from the Az_0 models of 100 sfu and 45 sfu, for high and low ionospheric activity and same *rcv-sat* configuration. Each set of 1 000 gaussian random errors is generated with a standard deviation of 0.1, 0.5, 1 and 2 *TECU* and the precision of the bias search vector increases from 1 *TECU* to 0.1 *TECU*, to provide similar precision of the random introduced errors. As such, the number of the bias values to test goes from 61 to 601 values (- 30 to 30 *TECU*), while *Az* interval remaines the same.

Therefore, from Fig. 33 and Fig. 34 for 15th hour and 6th hour, respectively, the results indicate that introduced random errors with precision higher that 0.1 *TECU* are mis-identified, while those equal or with lower precision are accurately identified, as is happens for the respective Az_0 model.

Also, during the highest ionospheric activity period the selected Az_0 models (45 or 100 sfu), are almost insensible to the mis-identification introduced by the random error's precision, staying between -0.05 and 0.05 *TECU*, whereas the Az_0 mis-modelling is flawless, with 0 *sfu* error (Fig. 33).

Not quite accurate and precise are the results for the 6th hour, although very close from the previous ones, since the mis-identification of the introduced random errors stayed between -0.07 and 0.07 *TECU* and the Az_0 mis-modelling effect between -1 and 1 *sfu* (Fig. 34).

Even if the last results seem irrelevant when compared with the precisions used, they can however, introduce a significant impact when dealing with real measurements for quiet activity hours of the day.

6.4.1.3. 1 000 GAUSSIAN RANDOM ERRORS PLUS CONSTANT BIAS

To conclude the assessment of the accuracy for the procedure using the same *rcv-sat* configuration (of Fig. 31), an Az_0 of 45 and 100 sfu, 1 000 gaussian random errors of 0.1, 0.5, 1 and 2 *TECU* combined with five different bias values of -5, -2.5, 0, 2.5 and 5 *TECU*, in Fig. 35 and Fig. 36, the results obtained for 15th hour and the 6th hour, respectively, are given.

As expected the bias identification was more accurate and precise for 15th hour than the 6th hour, since the 15th hour the bias mis-identification mean error was around -0.0015 to 0.003 *TECU*, whereas for 6th hour was around - 0.0045 to 0.003 *TECU*. The standard deviation in turn, was between 0.0280 and 0.0298 *TECU* for the 15th hour, while for the 6th hour was between 0.042 and 0.044 *TECU*, considering the worst case results (Az_0 of 45 *sfu*).

The Az_0 model identification results were also better for the 15th hour than the 6th hour, since no mis-modelling were found, whereas for the 6th hour the mean Az_0 mis-modelling error was between - 0.04 and 0.06 *sfu* and the standard deviation between 0.64 and 0.70 *sfu*.

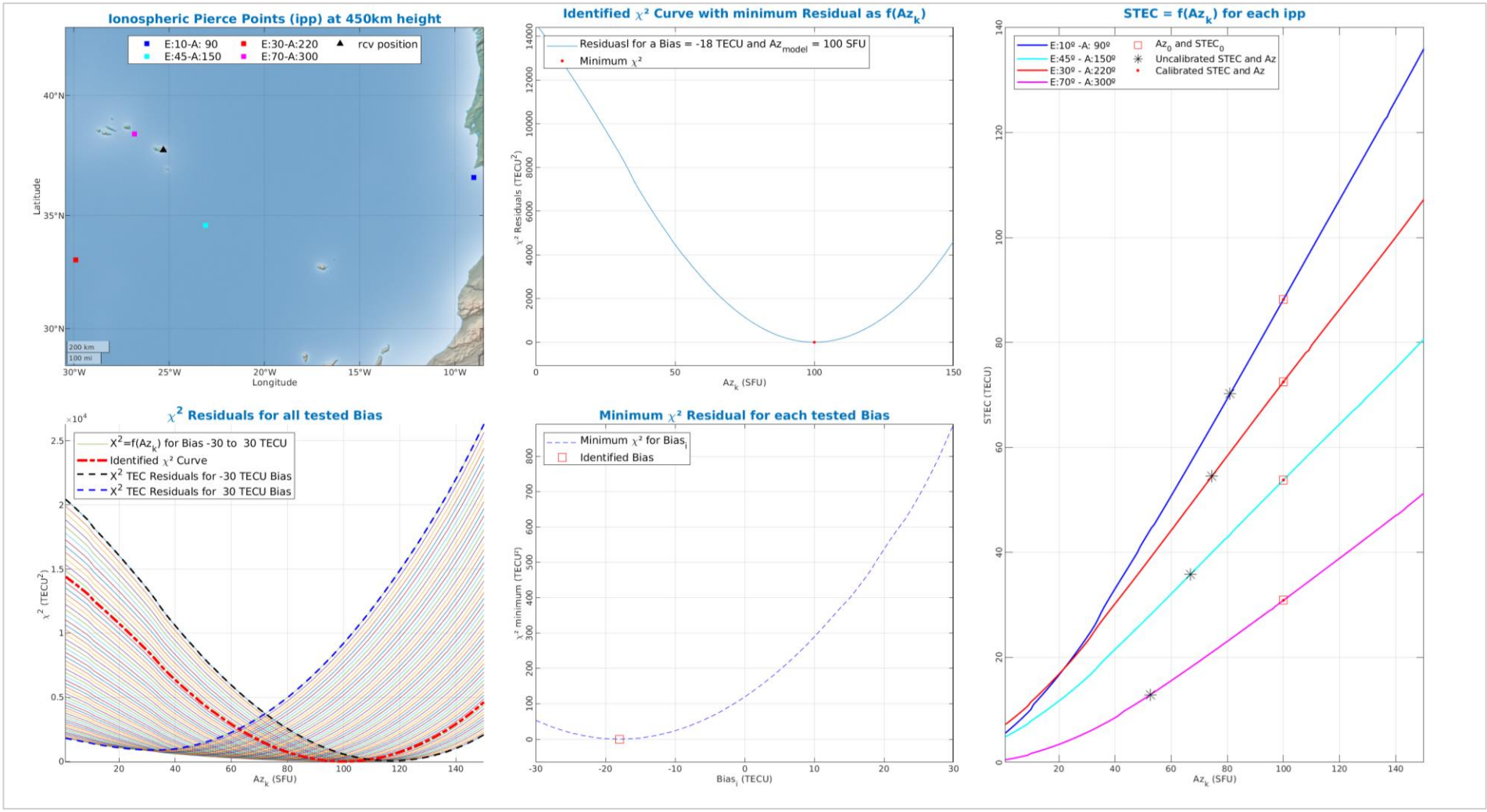

Fig. 31 – Error assessment of the $\min[\chi^2(t)]$ procedure to identify a pre-selected bias of -18 *TECU,* during the15th hour of the 4th month, for a specific satellite configuration, using simulated *STEC* data. In [1,1] *IPP's* at a layer height of 450 km; in tile [1:2,3] *STEC versus* the *Az* models for each *rcv-sat* ray-path, with and without uncalibrated measurements (identified by the respective square or star marker) where $STEC_0$ is the true unbiased value the procedure will look for (testing for several *Az* models every trial bias); in tile [2,1] are the $\min[\chi^2(t)]$ results for each *Az* model (1-150 *sfu*) plus a trial bias value (from -30 to 30 *TECU*) from which the minimum χ^2 is identified with relation to *Az* (the expected Az_0) and the respective trial bias that scored the lowest residual; in tile [2,2] a curve with all minimum residuals associated with each tested bias values identifying -18 TECU as being the minimum; in tile [1,2] is identified curve of tile [2,1].

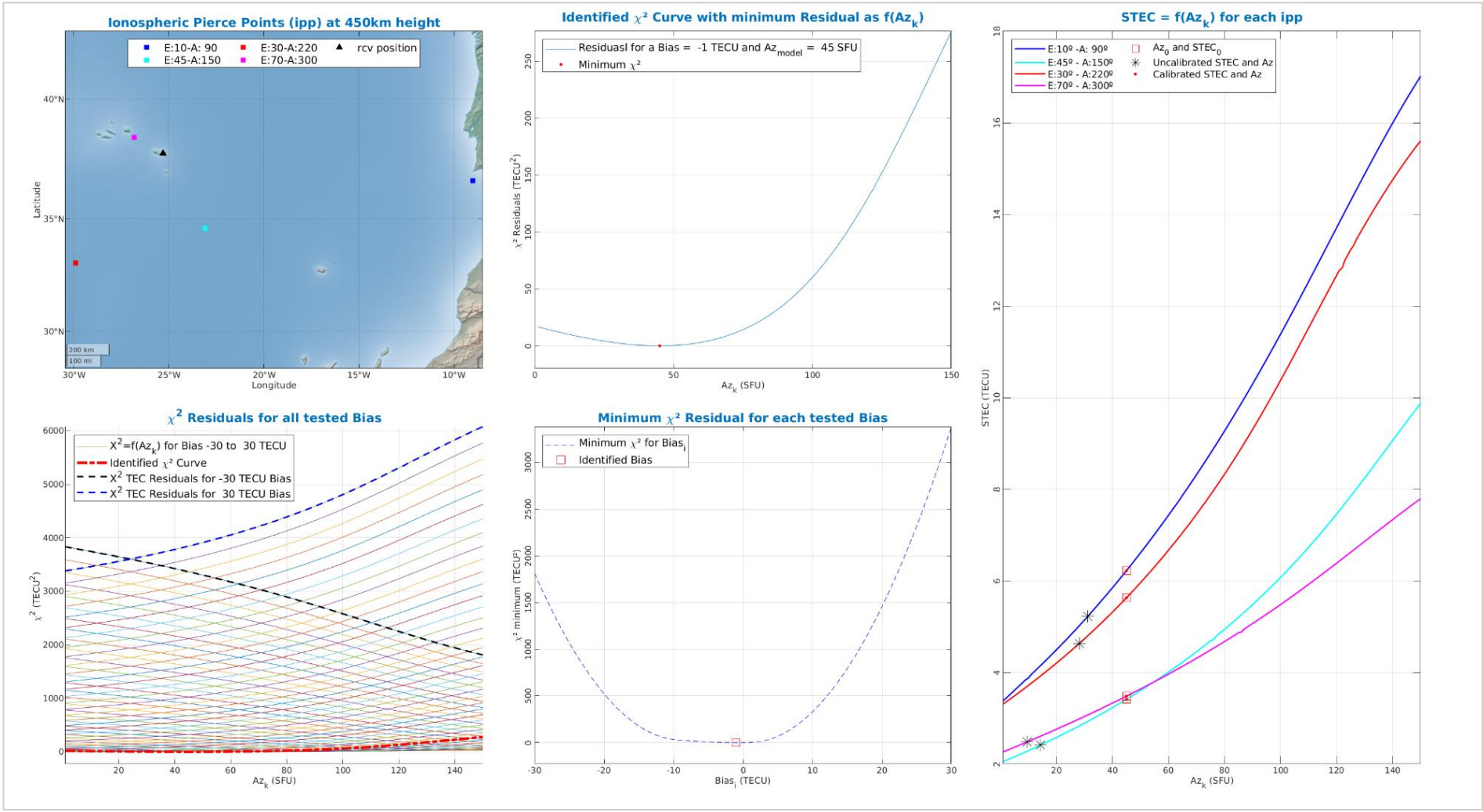

Fig. 32 – Error assessment of the $\min[\chi^2(t)]$ procedure to identify a pre-selected bias of -1 *TECU*, during the 6th hour of the 1st month, according to the same premises mentioned in Fig. 31.

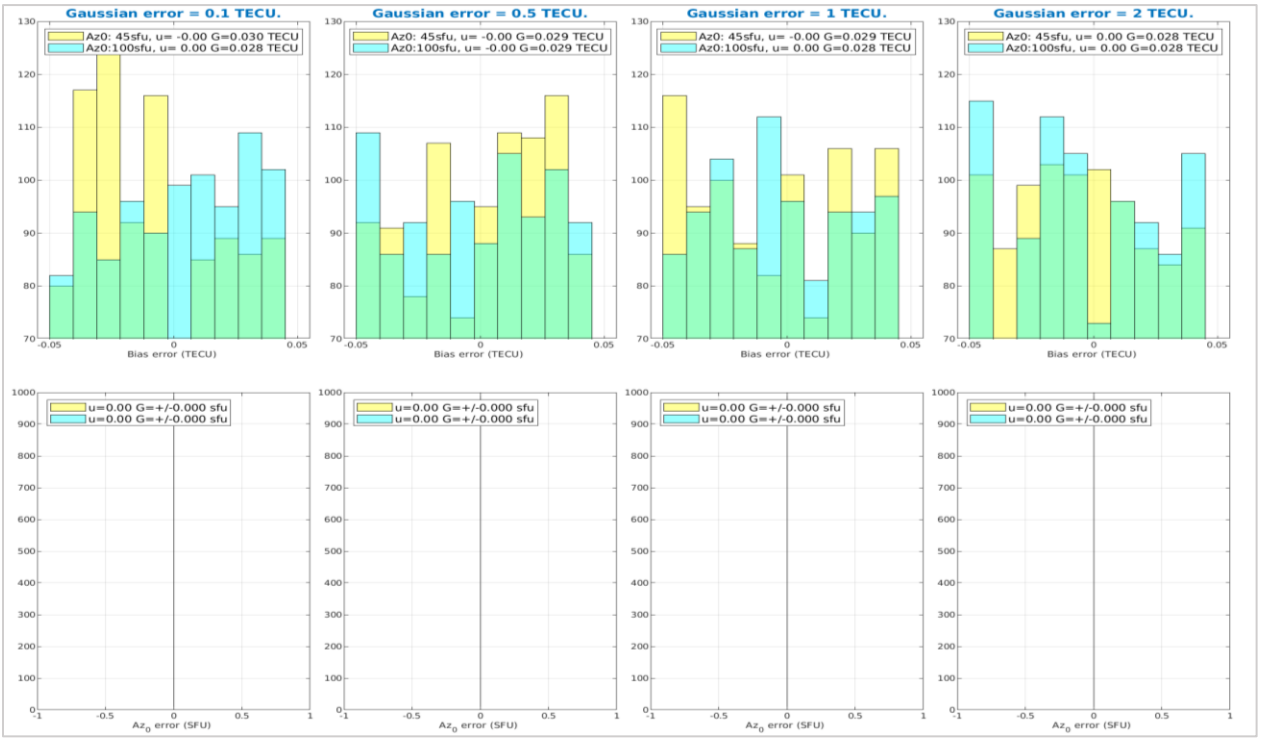

Fig. 33 – Histograms with bias mis-identification and Az_0 mis-modelling when adding 1 000 gaussian random errors of 0.1, 0.5, 1 and 2 TECU to each *rcv-sat* ray-path, using $STEC_0$ values obtained from pre-selected Az_0 models of 45 *sfu* and 100 *sfu* for 15th hour *UTC* of month 4, considering the same *rcv-sat* configuration of Fig. 31.

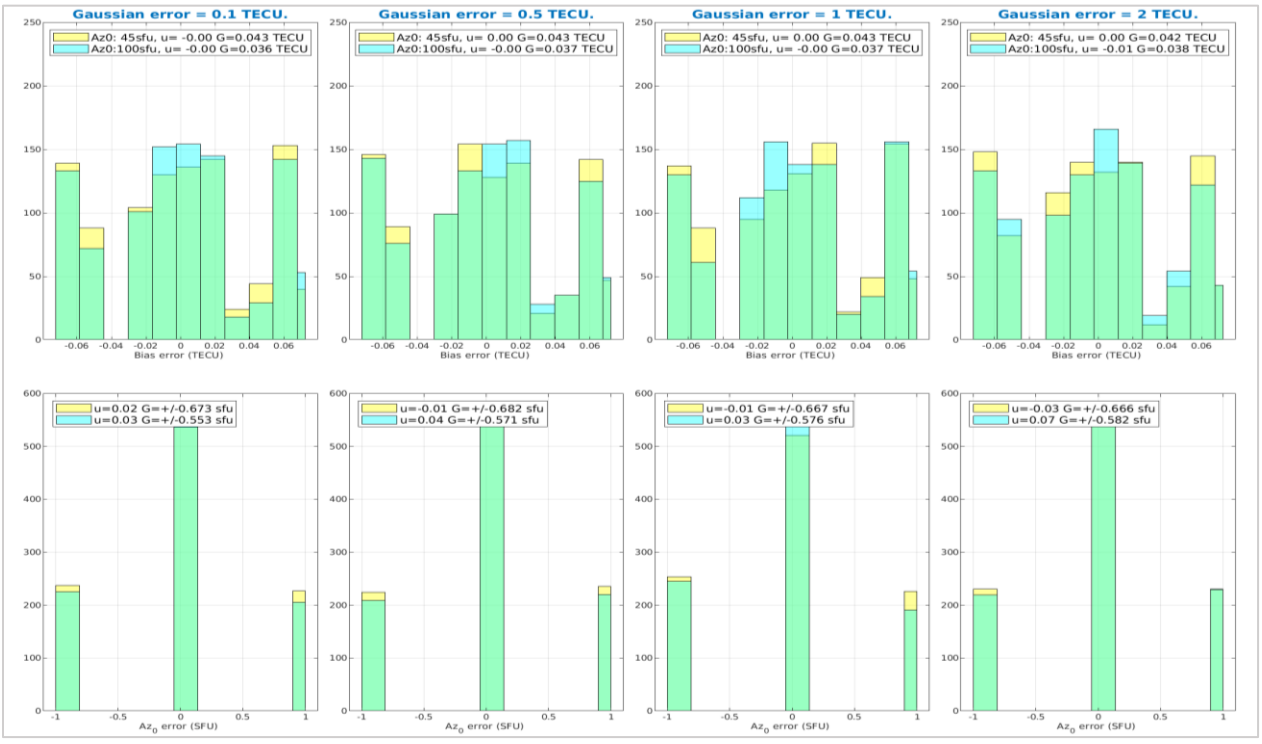

Fig. 34 – Histograms with bias mis-identification and Az_0 mis-modelling when adding 1 000 gaussian random errors of 0.1, 0.5, 1 and 2 TECU to each *rcv-sat* ray-path, using $STEC_0$ values obtained from pre-selected Az_0 models of 45 *sfu* and 100 *sfu* for 06th hour *UTC* of month 1, considering the same *rcv-sat* configuration of Fig. 31.

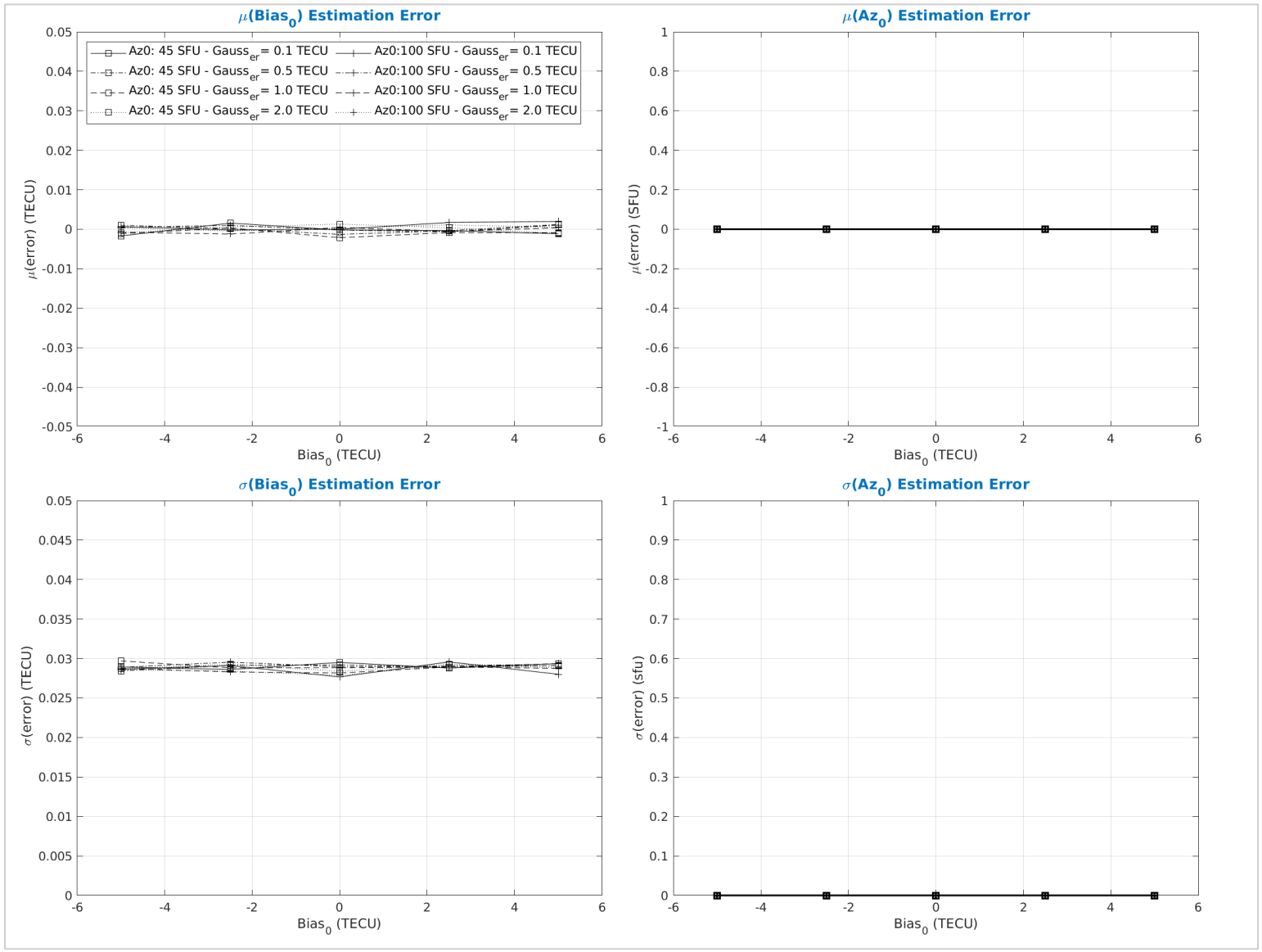

Fig. 35 – Mean and standard deviation for bias mis-identification and Az_0 mis-modelling, when adding 1 000 gaussian random errors of 0.1, 0.5, 1 and 2 *TECU* to 5 bias values of -5, -2.5, 0, 2.5 and 5 *TECU* for each *rcv-sat* ray-path (as shown in Fig. 31), considering an Az_0 model of 45 and 100 *sfu* for 15th hour *UTC* of month 4.

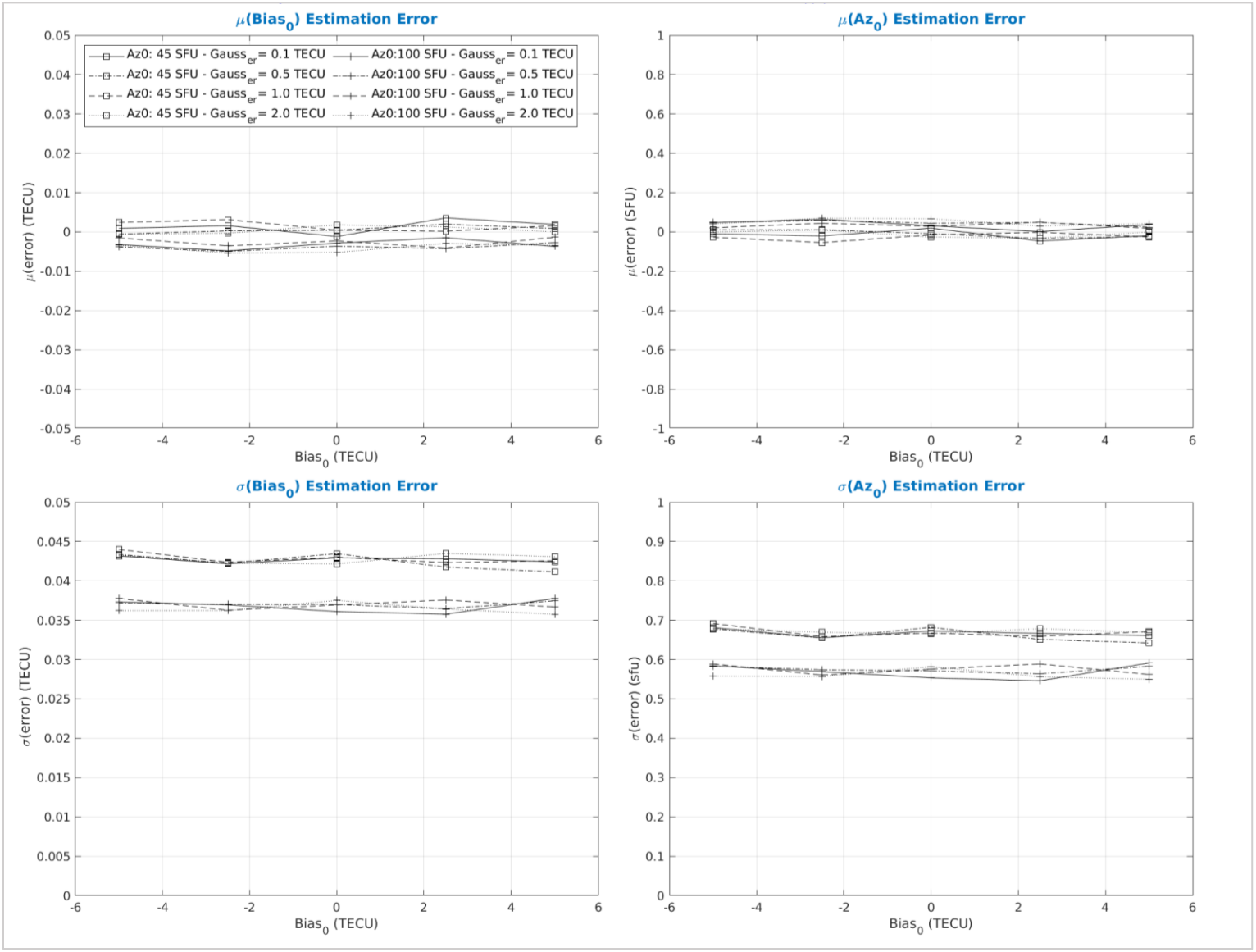

Fig. 36 – Mean and standard deviation for bias mis-identification and Az_0 mis-modelling, when adding 1 000 gaussian random errors of 0.1, 0.5, 1 and 2 *TECU* to 5 bias values of -5, -2.5, 0, 2.5 and 5 *TECU* for each *rcv-sat* ray-path (as shown in Fig. 31), considering an Az_0 model of 45 and 100 *sfu* for 06th hour *UTC* of month 1.

7. RESULTS AND DISCUSSION

As mentioned in 5.1, the following results with exception for the calibration phase, will solely analyze Furnas reference station (it was the only available dataset to work with), which consequently implies that the best adjustment strategy for *rDCB* calibration is not known until the selected reference offset is applied to the adjustment results of the other stations during the calibration phase in 7.6. Therefore, this section from 7.1 to 7.4, will focus on finding the right adjustment strategy according to the accuracy results obtained for the reference station *DCB* (its true value was known beforehand) and the daily effective ionization (*Az*) broadcast values.

The $\min[\chi^2(t)]$ adjustment procedure was applied to pre-processed semi-calibrated (and cycle-slip corrected) *CCL* ionospheric measurements, as mentioned in 5.2 (Fig. 21), to produce a valid number of observations as given in Tab. 4. Two filters were applied to the processed observations for the *Az* mis-modelling values exclusion of 1 sfu and 150 sfu (the latter was the maximum pre-defined *Az* threshold set for the adjustment).

Tab. 4 – Number of remaining observations after applying two filters of 1 *sfu* and 150 *sfu* to the *Az* results, given by the $\min[\chi^2(t)]$ adjustment procedure for each of pre-selected elevation mask.

Elevation Mask	Initial Number of Observations		1st Filter Az=1sfu	Remaining Observations		2nd Filter Az=150sfu	Remaining Observations	
[º]	N	[%]	n	N	[%]	n	N	[%]
10	17752	100	-8	17744	99.95	0	17744	99.95
20	17752	100	-40	17712	99.77	-2	17710	99.76
25	17752	100	-35	17717	99.80	-3	17714	99.79
30	17752	100	-38	17714	99.79	-114	17600	99.14

7.1. RECEIVER DCB AND AZ DAY-TO-DAY VARIATION

The summary with *rDCB* daily mean and *Az* mean models, using a $\min[\chi^2(t)]$ adjustment of five minute epochs (single epoch) and a 24 hour-long combined epoch ($12_{(5\ min)}$ x $24_{(hour)}$) is shown in Fig. 37 and Fig. 38, respectively. In Fig. 37, the daily mean *rDCB* variation from DOY 182 to 243 (*i.e.*, 62 days) is provided according to each elevation mask as it should be for the 24 hour adjustment (Fig. 38). However, in the latter case, the mean value was insensitive to the elevation mask.

On both figures (Fig. 37 and Fig. 38) an additional (+/-) standard deviation line (horizontal pointed lines) regarding the 62 day mean for each elevation mask is shown, although, in the former (Fig. 37), a daily standard deviation (colored squares) is also added, for stability analysis of the daily solution concerning the single epoch adjustments (288 epoch bias fits per day).

Also, in the right side of the mean *rDCB* tile (of Fig. 37 and Fig. 38) four histograms according to each elevation mask, are drawn to account for the *rDCB* daily variation in respect to the overall mean, where the error of the mean is computed according to $\mu \pm \sigma/\sqrt{N}$. With μ being the overall mean, σ, the standard deviation from the overall mean and *N* the number of days (62). A summary with the statistical information for the *rDCB* time-series mean, standard deviation and mean error, according to the adjustment procedure and elevation mask, is given in Tab. 5. Notice, that the accuracy evaluation is given according to its true bias of approximately 0 *TECU*.

Tab. 5 – Furnas reference station mean *rDCB*, standard deviation and error of the mean for the $\min[\chi^2(t)]$ adjustment procedure of 5 min and 24 h, per elevation mask, for DOY182-243 of 2019.

Number of Days	**Elevation Mask**	**Adjustment Strategy**	**Mean (μ)**	**Standard Deviation (σ)**	$Error = \mu \pm \sigma/\sqrt{N}$
N	[º]	[time]	[TECU]	[TECU]	[TECU]
62	10	5 min	5.68	0.385	5.68 ± 0.049
		24 hr	3.54	0.700	3.54 ± 0.089
	20	5 min	5.14	0.355	5.14 ± 0.045
		24 hr	3.58	0.715	3.58 ± 0.091
	25	5 min	5.03	0.365	5.03 ± 0.046
		24 hr	3.58	0.715	3.58 ± 0.091
	30	5 min	4.65	0.400	4.65 ± 0.051
		24 hr	3.58	0.715	3.58 ± 0.091

According to Tab. 5, the minimum *rDCB* mean error was 4.65 ± 0.051 *TECU* (1.632 ± 0.017 ns) for the 5 min adjustment (30º elevation mask) and 3.54 ± 0.089 *TECU* (1.242 ± 0.032 ns) for the 24 h adjustment (10º elevation mask). Suggesting that the 24 hour adjustment is more accurate, despite the lower precision, than the 5 min adjustment. Additionally, the 24 h adjustment provides almost the same *rDCB* mean*,* due to the noise threshold penalization used for the trial bias during low ionospheric activity (at pre- and dawn hours), since it suppressed some of the bias values (in the sum of epochs) that wouldn't be, if compared to the single epoch case. In the single epoch, every penalized trial bias (b_i) value from (Eq. 49) is excluded only at the respective epoch, instead of the entire sum of epochs. Reason why the sum of epochs mean bias is somehow flattened down, independently of the elevation mask.

Lastly, the stability of the single epoch adjustment is notably higher than the sum of epochs, if one compares the dispersion of daily results around the overall mean, given by the four histograms of both figures (Fig. 37 and Fig. 38). Meaning, that in the single epochs case, a lower mismodelling effect seems to be present for RDCB estimation, than for the 24 hour adjustment.

Proceeding into the *Az* estimated mean models, in the second row's tile of Fig. 37 and Fig. 38, the *Az* is also represented according to four elevation masks and, in this case, compared against the broadcast *Az* daily model and the 3 hour *Kp* geomagnetic index (2.6.2).

Please note in the left vertical axis of the *Az* tiles, that the daily solar flux units (sfu) are represented for the estimated and broadcasted *Az* models, while in the right axis, the 3 hour *Kp* indices are represented with an integer variation from zero (quiet) to 9 (greatly disturbed), with 0-4 quite (or minor geomagnetic storm), 5-6 moderate storm and 7-9 intense storm.

Additionally, from the *Az* tiles of Fig. 37 and Fig. 38, note the anomaly occurrence from days 10th to 15th of July (DOY 191-196) for the broadcast *Az* models, where the coefficients $a_0 = 48.5$ 0.03125, $a_1 = 0.03125$ and $a_2 = 0.0073853$ kept blocked during the entire period. Probably, because an algorithm security procedure blockage occurred (in the event of anomaly detection for the *Az* global estimation), only detected/fixed on the 16th of July (DOY 197), since the broadcasted Az coefficients sent back then were all 0. In such cases, according to GAL-OS-IONO (2016), the default values to consider and correct for a significant contribution of the ionospheric delay error should be $a_0 = 63.7$, $a_1 = 0$ and $a_2 = 0$. Therefore, 63.7 *sfu* for the Az model in DOY197, regardless of the ground station position.

Hence, the *Az* mean error differences with reference to the broadcast *Az* values for the single epoch and 24 h adjustments, will be estimated starting from July 17th to August 31st (DOY198-243). Thus, according to Fig. 37, Fig. 38 and Tab. 6, the 24 h *Az* mean modulation seems to provide higher accuracy than the 5 min adjustment, since the lowest mean difference was around 0.01±0.65 *sfu* (20º mask, 24 h), while for the single epoch was around 1.38±0.57 *sfu* (also 20º mask). Meaning, that the single epochs case, the *Az* modulation as higher mismodelling effect than the sum of epochs.

Tab. 6 – *Az* mean error differences for the 5 min and 24 h $\min[\chi^2(t)]$ adjustments with reference to broadcasted *Az* model values, from July 17th to August 31 (DOY198-243).

Az estimation mean differences	$Error_{\mu_{Az-Az_{Broadcast}}} = \mu \pm {}^{\sigma}/_{\sqrt{N}}$			
Elevation Mask	10º	20º	25º	30º
5 min [sfu]	-2.63 ± 0.60	1.38 ± 0.57	2.60 ± 0.62	5.22 ± 0.68
24 h [sfu]	-3.25 ± 0.66	0.01 ± 0.65	1.42 ± 0.65	2.14 ± 0.68

In the overall, the 24 hour adjustment seems to provide higher accuracy for *rDCB* estimation and *Az* modulation than the single epoch adjustment. Also, the 10º elevation mask seems more accurate for *rDCB* estimation, although the 20º mask for the *Az* estimation offers higher agreement with the *Az* broadcast values, independently of the adjustment scenario (5 min or 24 h adjustment).

Therefore, without having any knowledge at this stage about adequacy of the adjustment time strategy and elevation mask that will provide the best results for the calibration process, the 10º and 20º elevation mask using both time strategies are selected for further analysis.

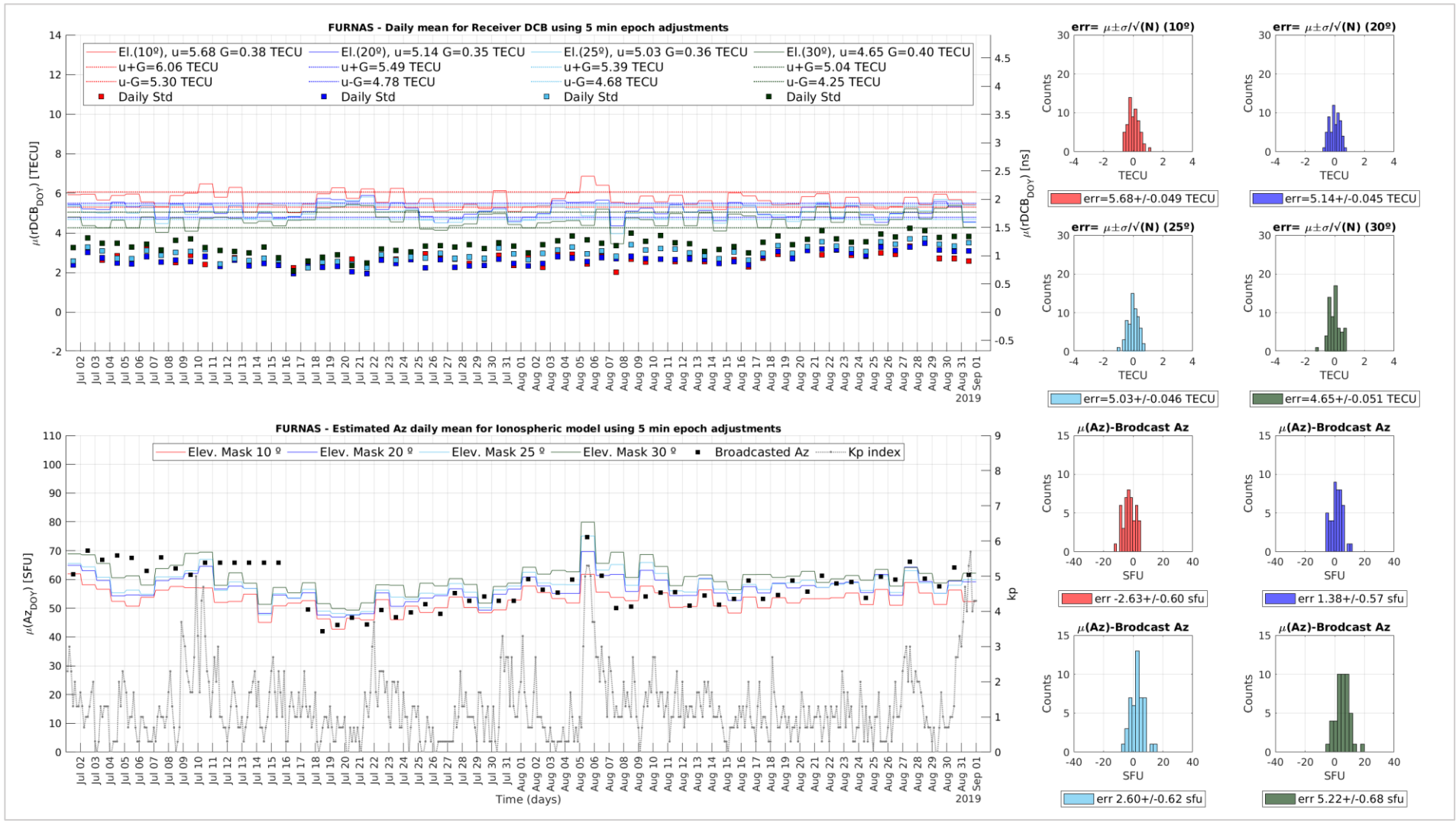

Fig. 37 – Furnas day-to-day results for the $\min[\chi^2(t)]$ adjustment procedure (using single 5 minute epochs) for *rDCB* daily mean (1st row tile) and corresponding *Az* daily mean (2nd row tile), from DOY 182 to 243 of 2019. The *rDCB* daily mean, daily standard deviation and Az daily mean model is depicted according the 10º (in red), 20º (in blue), 25º (in cyan) and 30º (in green) elevation mask. Four histograms with the *rDCB* daily mean variation (right side of the 1st row tile) and (below, 2nd row tile right side) four histograms with the difference between estimate *Az* daily mean against the broadcast *Az* values, from July 17th to August 31.

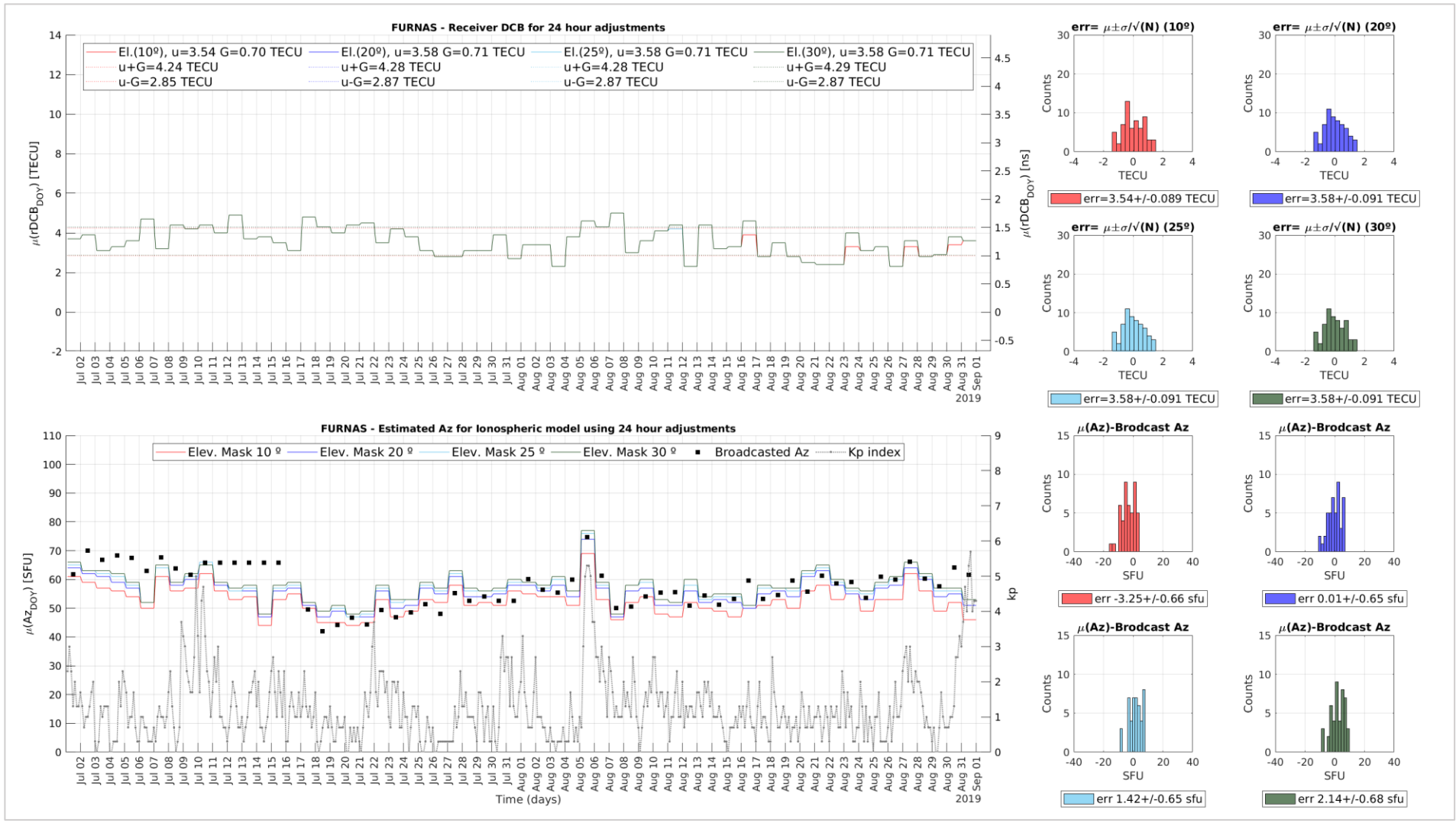

Fig. 38 – Furnas day-to-day results for the $\min[\chi^2(t)]$ adjustment procedure (using the 24 hour sum of epochs) with identical description for the plots meaning, according to Fig. 37.

7.2. RECEIVER DCB AND Az INTRA-DAY VARIATION

NeQuick-G Az models are an empirical climatological representation of the ionosphere that predicts monthly mean electron densities. Therefore, the monthly variations from DOY182-212 and DOY 213-243, given in Fig. 39 and Fig. 40, respectively, have higher significance than the complete time-series from DOY182 to 243 (Fig. 41), for the *rDCB* and *Az* intra-day variation analysis.

Please note, for the single epoch adjustment results that the corresponding intra-day *rDCB* and *Az* model exhibits a strong epoch variation (scattering), that worsens as the elevation mask increases. This could be related to errors in model, multipath, measurement noise, and sub- daily bias drifts. Ideally, the data should all lie on a horizontal line, indicating the bias value for the site, but this seldom occurs (Komjathy et al., 2005).

Indeed, if one places the 24 hour adjustment side-by-side with the intra-day results, between midnight (0 h UTC) and sunrise (7 h UTC), the mean intra-day variation (10º elevation) suggests a *rDCB* and *Az* model, relatively flattened and close to the 24 hour adjustment. Though, as the solar radiation starts to increase this clearly breaks off and higher *rDCB* values start to appear, with inversely lower *Az* values. This latter fact, in turn, establishes a strict inverse correlation between the *rDCB* and *Az* values, that for each increase in the *Az* value a decrease in the *rDCB* occurs and *vice-versa*.

Also, the *rDCB* intra-day variation has different epoch trends, depending on the time of the day, month of the year and elevation mask. This maybe be attributed to the daily geometry change / shift of the GPS satellites in view, due to the difference between the solar day and sidereal day time (3 min and 56 sec).

A summary with the mean *rDCB* and mean *Az* model, according to three different time series and adjustment strategies is provided in Tab. 7.

Tab. 7 – Receiver *DCB* and *Az* results for the 5 min and 24 h $\min[\chi^2(t)]$ adjustment, considering three time-series analysis, DOY 182-212, DOY 213-243 and DOY 212-243 of year 2019.

	Adjustment Time	DOY	Elevation Mask			
			10º		20º	
			μ	σ	μ	σ
rDCB [TECU]	5 min (intra-day)	182-212	5.69	2.698	5.17	2.481
		213-243	5.67	2.793	5.10	2.882
		182-243	5.68	2.746	5.13	2.690
	24 h (daily)	182-212	3.76	0.615	3.76	0.615
		213-243	3.33	0.704	3.40	0.746
		182-243	3.54	0.695	3.58	0.707
Az [sfu]	5 min (intra-day)	182-212	51.80	17.53	55.10	19.25
		213-243	53.91	19.53	58.33	22.16
		182-243	52.86	18.59	56.73	20.82
	24 h (daily)	182-212	52.87	5.01	55.65	5.19
		213-243	52.48	4.63	56.00	4.93
		182-243	52.68	4.83	55.82	5.07

From Tab. 7 mean and standard deviation results, according to each elevation mask, it is possible to verify that using the single epoch adjustment, the *rDCB* estimation is almost insensible to the month of the year (for instance 5.69 and 5.67 *TECU,* equals to 0.02 *TECU* variation (10º elevation), while 0.43 TECU for the 24 hour sum of epochs) and inversely, for *Az* model, is highly sensible. This relation could appropriate for the calibration process using the single epoch adjustment, since it reveals insensibility of the *rDCB* on time, and inversely, for Az model, a necessary dependence or sensibility.

7.3. RELATIVE ADJUSTMENT DIFFERENCES FOR QUIET AND ACTIVE DAYS

Taking in consideration the accuracy of the 24 h adjustment mentioned in 7.1 and also the stability of the single epoch adjustment, mentioned in 7.2, a comparative evaluation for each adjustment according to elevation mask and the geomagnetic activity (quiet and active days), is given in Fig. 42.

Apparently, according to the *rDCB* results (single epoch, Fig. 42), the 20º mask seems to provide lower reaction / sensibility to geomagnetic activity, thus, higher stability than the 10º elevation mask, as the mean value only varies from 5.68 *TECU* (quiet) to 5.56 TECU (active), -0.12 *TECU* (decreasing), while it increases +0.56 *TECU* for 10º elevation mask. Inversely, this stability seem not to hold for the *Az* models estimation, according to the standard deviation results of the 10º mask, compared with the 20º.

Moreover, using the 24 h adjustment as reference result in Fig. 42 and Tab. 8, a mean relative difference between the single epoch adjustment and the hereby reference, is computed for relationship evaluation for *rDCB* and *Az* estimation, under different elevation masks and geomagnetic activity. Hence, from Tab. 8, the 20 º elevation mask seems to provide higher accuracy and stability for *rDCB* estimation, despite a prevalent tendency for *Az* mis-modelling, as seen by its standard deviation results.

Tab. 8 – Mean error adjustment difference between the 5 min epoch adjustment against the 24 h, for *DOY's* 200 and 217 and elevation masks of 10 and 20º.

		$Error_{(X_{t=5min} - X_{\mu_{24h}})} = \mu \pm \sigma$	
	DOY	10º	20º
X = $rDCB_t$ [TECU]	200 (Quiet)	2.28 ± 2.44	1.68 ± 2.30
	217 (Active)	2.26 ± 2.43	0.96 ± 2.54
X = Az_t [sfu]	200 (Quiet)	-2.29 ± 17.45	-2.12 ± 18.16
	217 (Active)	-7.20 ± 16.39	-4.30 ± 21.84

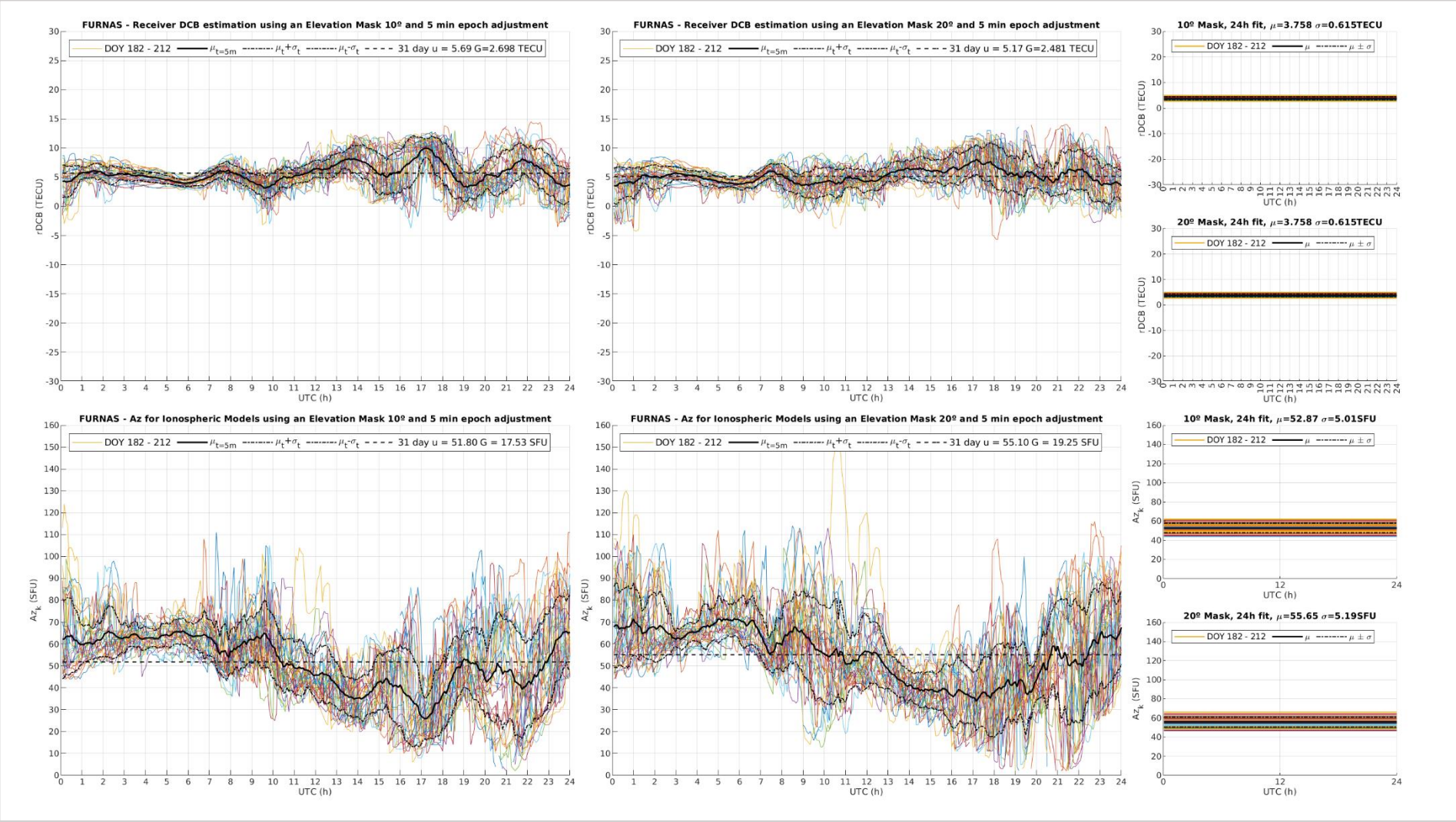

Fig. 39 – Receiver *DCB* and *Az* intra-day variation values using a 5 min epoch $\min[\chi^2(t)]$ adjustment procedure in comparison with the 24 h adjustment, for the time-series ranging from *DOY* 182 to 212 of 2019 and elevation masks of 10 and 20º.

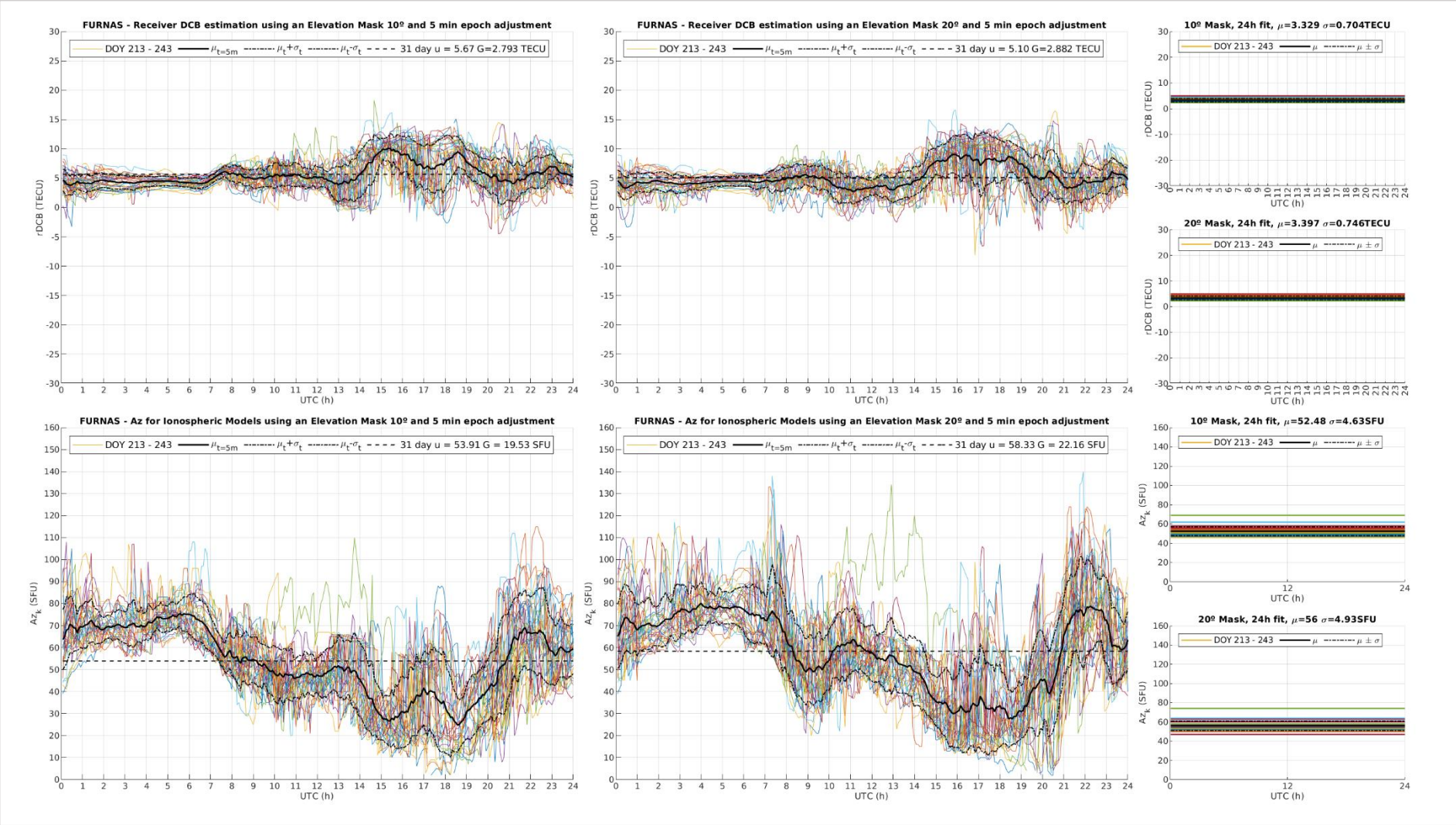

Fig. 40 – Receiver *DCB* and *Az* intra-day variation values using a 5 min epoch $\min[\chi^2(t)]$ adjustment procedure in comparison with the 24 h adjustment, for the time-series ranging from *DOY* 213 to 243 of 2019 and elevation masks of 10 and 20º.

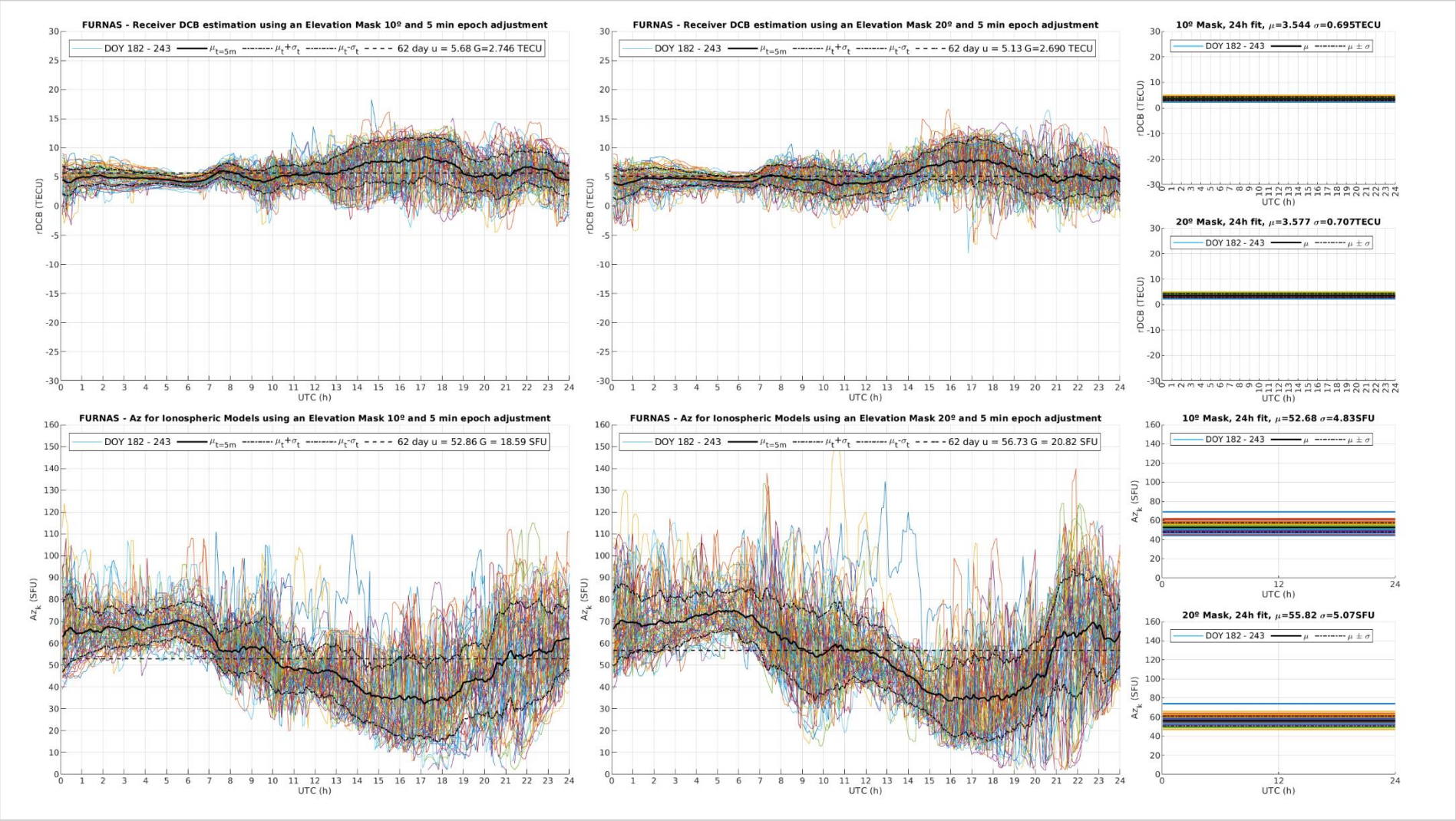

Fig. 41 – Receiver *DCB* and *Az* intra-day variation values using a 5 min epoch $\min[\chi^2(t)]$ adjustment procedure in comparison with the 24 h adjustment, for the time-series ranging from *DOY* 182 to 243 of 2019 and elevation masks of 10 and 20º.

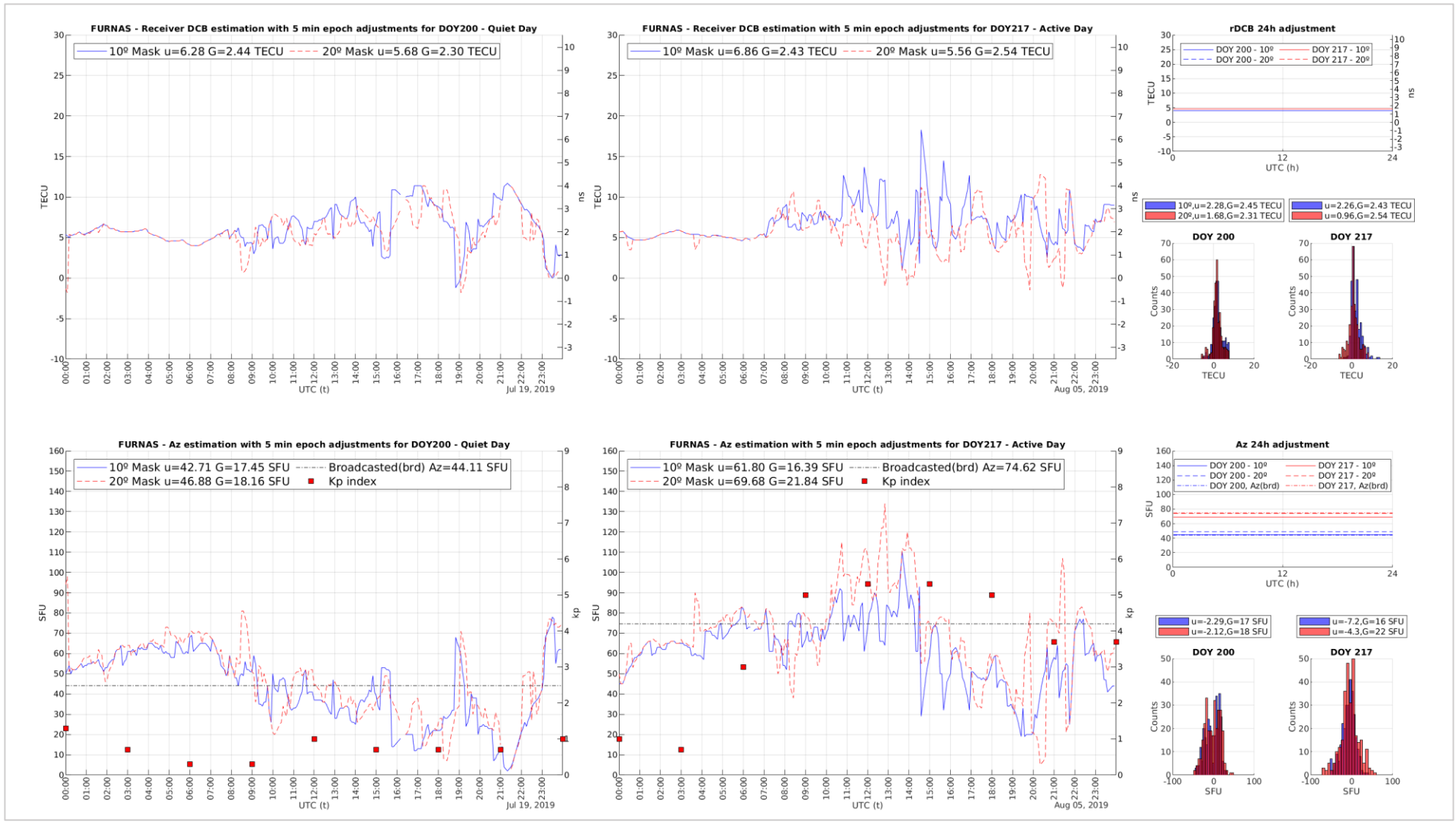

Fig. 42 – Receiver *DCB* and *Az* results for the 5 min epoch adjustment during a quiet day (1st tile column) and active day (2nd tile column). Receiver *DCB* and *Az* for the 24 h adjustment for the same *DOY's* (3rd tile column, 1st and 3rd rows). Histograms with 5 min epoch difference against 24h *rDCB* estimation (3rd column, 2nd row) and *Az* estimation (3rd column, 4th row).

7.4. ESTIMATED Az VTEC RESULTS VERSUS REFERENCE GIM VTEC

Considering the overall accuracy and precision achieved by each $\min[\chi^2(t)]$ adjustment, expressed in Fig. 37, Fig. 38, Tab. 6, and Tab. 7, the 24 h adjustment with a 20º elevation mask will be adopted for further analysis against reference values.

The following statistics are just for quality evaluation of *Az* estimation, since they are not calibrated yet. Only applying the offset of the reference station to other stations *DCB*, would improve the *Az* estimation and thus the *VTEC* results that are compared next.

Therefore, in Fig. 43, the reference *VTEC* from three *GIM's* generated by *UPC*, *COD* and *IGS* are plotted against the *VTEC* generated by the *Az* broadcast model and the estimated *Az* for *DOY* 200 (July 19th) and 234 (August 22nd) (quiet days) and *DOY* 191 (July 10th) and 217 (August 5th) (active days) of 2019.

Except from a very small difference in *DOY* 200, the broadcast and estimated *Az* models perfectly match for the selected *DOY's*. Moreover, the *Az* estimated *VTEC* results, generally under-estimates, during pre-dawn and peak solar irradiance hours (specially in active days), despite providing also, relatively close agreement with the reference during quiet days, independently of the *GIM*.

The overall estimation differences between the *Az VTEC* estimation and the reference values, are provided by four histograms in Fig. 43, where the highest amplitude differences were found to be around - 7 to 4 *TECU* (- 2.5 to 1.4 ns) for active days and around $\pm$ 4 *TECU* ($\pm$1.4 ns) for quiet days. In this sense and according to Tab. 9 the mean error difference for the worst *VTEC* adjustment, in active days, were found to be around -1.29 ± 2.75 *TECU* (-0.453±0.965 ns), whereas, in quiet days, around 1.19±1.71 *TECU* (0.417± 0.600 ns).

Tab. 9 –Mean error differences between the estimated Az VTEC and the reference GIM.

Reference AAIC's	DOY		$VTEC_{Az_{24h}} - VTEC_{REF}$		$\mu \pm \sigma$
			μ	σ	[TECU]
IGS	191	Active	-1.29	2.75	-1.29 ± 2.75
	217		-1.17	2.64	-1.17 ± 2.64
	200	Quiet	-0.71	1.20	-0.71 ± 1.20
	234		0.37	1.93	0.37 ± 1.93
UPC	191	Active	-0.58	2.11	-0.58 ± 2.11
	217		-0.35	2.10	-0.35 ± 2.10
	200	Quiet	-0.94	1.33	-0.94 ± 1.33
	234		-0.05	1.76	-0.05 ± 1.76
COD	191	Active	-0.05	2.49	-0.05 ± 2.49
	217		-0.14	2.31	-0.14 ± 2.31
	200	Quiet	0.24	1.26	0.24 ± 1.26
	234		1.19	1.71	1.19 ± 1.71

7.5. STEC FOR THE REFERENCE RECEIVER

If the *rDCB* estimation values were to be directly applied over the semi-calibrated *CCL* ionospheric measurements without any calibration adjustment procedure, as it will later be applied on other stations, the *STEC* «*calibration*» adjustment given by Fig. 44, would benefit from higher accuracy than the one presented in this example. Even though, the present exercise, provides a quality check for the 24 h adjustment strategy raw application of the *rDCB* estimation over the reference station, thus a «*pseudo-calibration*».

Therefore, considering the *VTEC* reference values extracted from *UPC, COD* and *IGS GIMs* against the «*pseudo-calibrated*» *STEC* for Furnas station, it shows that in general the *STEC* after the raw correction remained above the reference *VTEC* values, in general.

Inversely, if the estimated *Az* daily mean where to be used as *VTEC* reference*,* higher discrepancies between the «pseudo-calibrated» *STEC* and the *VTEC* from *Az* model would be seen, according to the erratic mixing of the minimum «*pseudo-calibrated*» *STEC* and the *Az* estimated *VTEC* values.

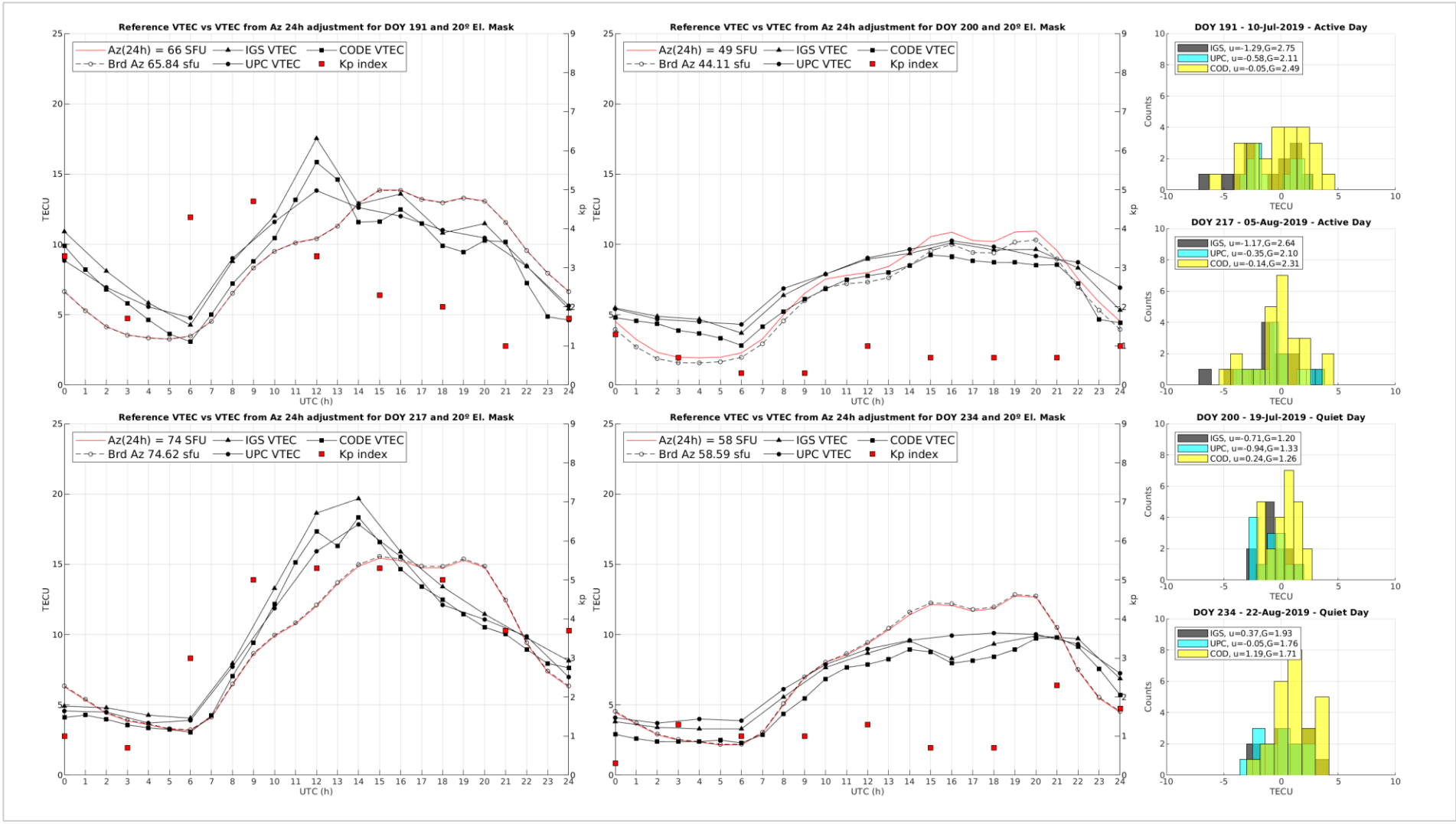

Fig. 43 –Broadcast and estimated *Az VTEC* values and reference *VTEC* according to *GIM* generated by UPC, COD and IGS, for two active days DOY 191 (July 10th) and 217 (August 5th) (1st column); and two quiet days *DOY* 200 (July 19th) and 234 (August 22nd) of 2019 (2nd column); absolute *VTEC* differences between estimated *Az VTEC* values and reference values (3rd column tiles).

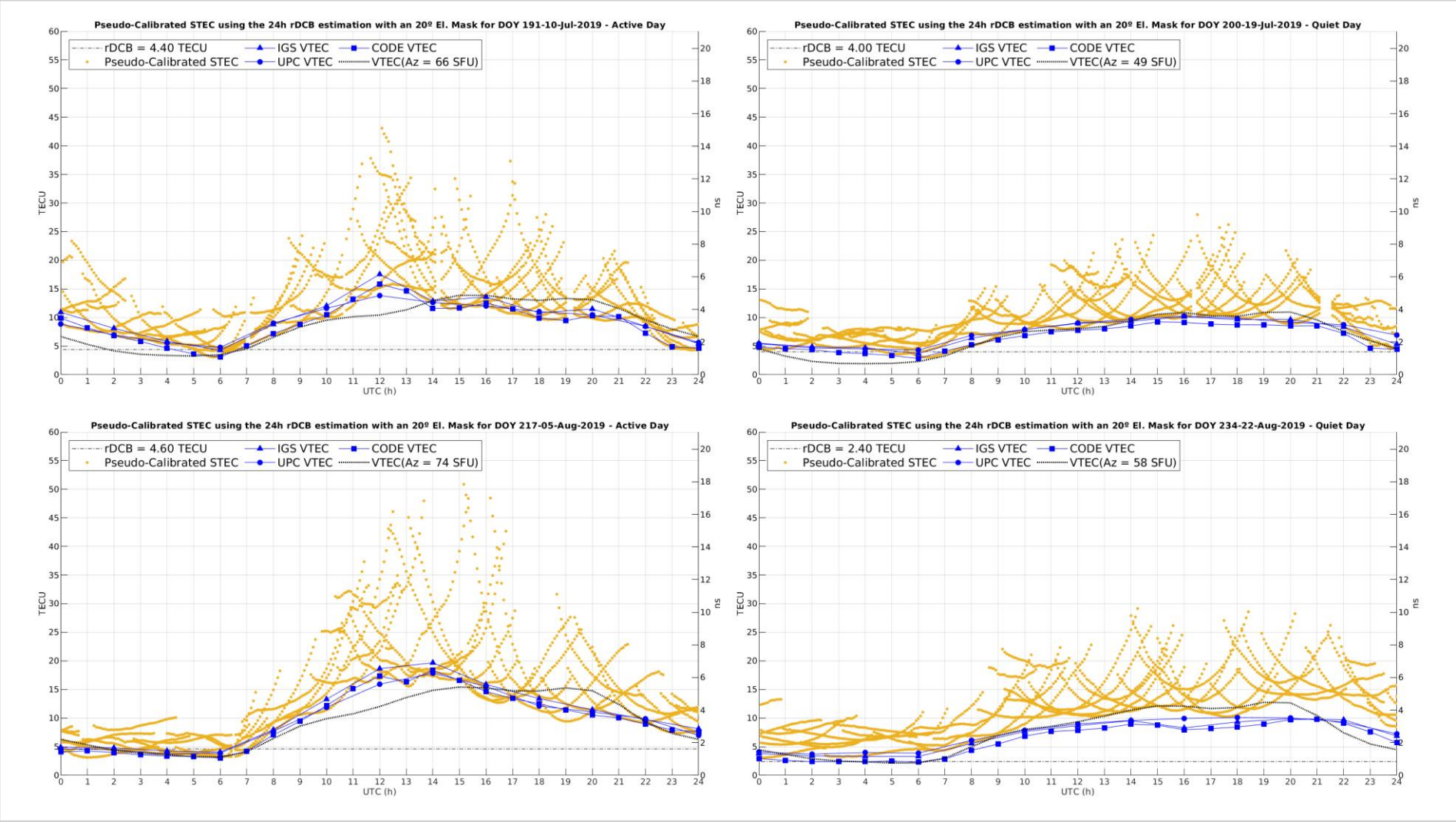

Fig. 44 – «*Pseudo-calibrated*» *STEC* results using the 24 h $\min[\chi^2(t)]$ adjustment with a 20º elevation mask, for two active days DOY 191 (July 10th) and 217 (August 5th) (1st column) and two quiet days DOY 200 (July 19th) and 234 (August 22nd) (2nd column) of 2019, against reference *VTEC* values from *UPC, COD* and *IGS GIMs*.

7.6. CALIBRATION RESULTS

After going through several $\min[\chi^2(t)]$ adjustments using distinct time strategies and elevation masks for day-to-day and intra-day variation analysis, the 20º elevation mask seems to be the most accurate candidate for achieving the best calibration results.

Hence, the *rDCB* calibration of the other ground stations referred in Tab. 3, will be estimated according to the *rDCB* offset acquired from the reference station (with a 20º mask) and different adjustment time strategies (5 min and 24h). Thus, in Tab. 10, the *rDCB* offset or mean error (Δ) is summarized.

Tab. 10 – Reference station *rDCB* mean error (Δ) according to the pre-selected elevation mask and time strategy adjustment (*N* = 62 days).

Elevation Mask 20º	Adjustment Time Strategy	rDCB Estimated μ [TECU]	rDCB Estimated σ [TECU]	rDCB Mean Error (Δ) $\mu - \sigma/\sqrt{N}$ [TECU]	rDCB Mean Error (Δ) $\mu + \sigma/\sqrt{N}$ [TECU]	True DCB [TECU]
REFERENCE	5 min	5.14	0.35	5.10	5.18	0
	24 h	3.58	0.71	3.49	3.67	

Using the same adjustment strategies applied to the reference station for *rDCB* estimation of Terceira, Flores and Funchal, the summarized results (mean μ and standard deviation σ) are reported in Tab. 11. Then, deducting the mean error (Δ) of the reference station to other stations estimated *rDCB,* predicts the mean *rDCB* of each station, according to the adjustment strategy used (Tab. 11). Thus, with before-hand knowledge of the true *rDCB* of each station, the mean prediction error for the calibration procedure can be estimated and summarized on Tab. 12.

Tab. 11 – Estimated and predicted *rDCB* results for Terceira, Flores, and Funchal ground stations, before and after applying the reference of offset from Furnas ground station, according to the $\min[\chi^2(t)]$ adjustment time strategy and elevation mask of 20º.

Elevation Mask 20º	Adjustment Time Strategy	rDCB Estimated μ [TECU]	rDCB Estimated σ [TECU]	Predicted rDCB $[\mu - \sigma/\sqrt{N}] - \Delta$ [TECU]	Predicted rDCB $[\mu + \sigma/\sqrt{N}] - \Delta$ [TECU]	True DCB [TECU]
TERCEIRA	5 min	3.92	0.92	-1.29	-1.15	0
	24 h	0.54	0.82	-3.05	-3.03	
FLORES	5 min	4.01	0.44	-1.14	-1.12	0
	24 h	2.35	0.58	-1.21	-1.25	
FUNCHAL	5 min	4.29	0.85	-0.91	-0.79	0
	24 h	2.01	0.46	-1.54	-1.60	

From Tab. 12 and according to the number of pre-calibrated stations used for the overall *rDCB* mean calibration accuracy, the 5 min epoch adjustment strategy provides higher calibration accuracy and precision than the 24 h adjustment, with a mean prediction error of -1.07 ± 0.075 *TECU* (-0.37 ± 0.026 ns) against -1.95 ± 0.351*TECU* (- 0.68 ± 0.123 ns).

Tab. 12 – Overall *rDCB* calibration accuracy and precision results, using a $\min[\chi^2(t)]$ adjustment time strategy a 20º elevation mask.

Adjustment Time Strategy	Station	Mean Prediction Error			
		[TECU]	[ns]	[TECU]	[ns]
5 min	TERCEIRA	-1.22	-0.43	-1.07 ± 0.075	-0.37 ± 0.026
	FLORES	-1.13	-0.40		
	FUNCHAL	-0.85	-0.30		
24 h	TERCEIRA	-3.04	-1.07	-1.95 ± 0.351	-0.68 ± 0.123
	FLORES	-1.23	-0.43		
	FUNCHAL	-1.57	-0.55		

Thus, exploring further the mean calibration error using only the 5 min adjustment strategy, but now assessing three elevation masks 10º, 20º and 30º, it can be seen from Tab. 13 that the 10º mask seems to be more accurate than the 20º mask, but, less precise. Inversely, the 30º mask seems to be very precise, but less accurate, in comparison.

Tab. 13 – Overall *rDCB* calibration accuracy and precision results, using the single epoch adjustment strategy with 10,20 and 30º masks.

Adjustment Time 5 min	Station	Mean Prediction Error			
		[TECU]	[ns]	[TECU]	[ns]
10º El. Mask	TERCEIRA	-1.32	-0.46	-1.04 ± 0.203	-0.36 ± 0.071
	FLORES	-1.39	-0.49		
	FUNCHAL	-0.4	-0.14		
20º El. Mask	TERCEIRA	-1.22	-0.43	-1.07 ± 0.075	-0.37 ± 0.026
	FLORES	-1.13	-0.4		
	FUNCHAL	-0.85	-0.3		
30 º El. Mask	TERCEIRA	-1.29	-0.45	-1.26 ± 0.027	-0.44 ± 0.010
	FLORES	-1.3	-0.46		
	FUNCHAL	-1.18	-0.41		

Thus, if the latter approach was replicated but in turn to include only the same receiver types, then the 20º mask provides better accuracy and precision than the 10º mask and even so, the 30º, can be more accurate than the 10º, according to Tab. 14. Hence, it may be assumed that the 20º elevation mask could potentially provide higher accuracy and precision for calibration, than the 10º mask, when using same receivers brand. Notable, is the degree of precision for the 30º mask (0.005 *TECU*).

Although, the 10º mask may offer better accuracy for a mixed receiver's network than a same type, a balanced conclusion at this point, having only three stations, should be to consider the 5 min epoch $\min[\chi^2(t)]$ adjustment strategy with a 20 º elevation mask, in any cases.

Tab. 14 – Overall *rDCB* calibration accuracy and precision results, using the single epoch adjustment strategy with 10,20 and 30º masks and same receiver type.

Adjustment Time 5 min	**Station**	**Mean Prediction Error**			
		[TECU]	[ns]	[TECU]	[ns]
10º El. Mask	TERCEIRA	-1.32	-0.46	-1.36 ± 0.021	-0.48 ± 0.007
	FLORES	-1.39	-0.49		
20º El. Mask	TERCEIRA	-1.22	-0.43	-1.18 ± 0.040	-0.41 ± 0.014
	FLORES	-1.13	-0.4		
30 º El. Mask	TERCEIRA	-1.29	-0.45	-1.30 ± 0.005	-0.45 ± 0.002
	FLORES	-1.3	-0.46		

Finally, please note that the broadcast *TGDs* values are of discrete nature (2^{-31}s = 0.47ns) due to the limited number of bits in the GPS legacy navigation message (Villiger et al., 2019) (GPS interface specification (ICC, 2019)) and that the reported accuracy of *IGS IAAC's* for receiver *DCB* estimates, are approximately 0.3-0.5 ns (Sanz et al., 2017). Meaning, that the present strategy for receiver *DCB* estimation can achieve accuracies higher than legacy satellite *TGD* updates from NAVSTAR GPS control center and it can meet the state of the art requirements for receiver DCB estimation in comparison to *IGS IAAC's.*

8. CONCLUSIONS AND FUTURE WORK

Using a single epoch $\min[\chi^2(t)]$ adjustment procedure with *Nequick-G Az* models, for *rDCB* estimation and calibration, was able to provide a mean calibration error for *GPS* legacy L_1 and L_2 frequencies of -1.07 ± 0.075 TECU (-0.37 ± 0.026 ns) at a mid-latitude region and during a solar cycle minimum.

Moreover, the hereby discussed strategy was able to provide accuracies higher than the legacy satellite *TGD* updates (0.47 ns) broadcasted by *NAVSTAR GPS* and meet the state of the art requirements for receiver *DCB* estimation as compared to *IGS IAAC's (*0.3-0.5 ns).

Simultaneously, these results, compared against direct calibration accuracy (0.1 TECU), remained within one order of degree gap, which could encourage the use of this tool for receiver network management and redundancy.

Therefore, according to the results of the proposed methodology, it can be asserted that the overall objective set for the development of this dissertation were accomplished, based on the degree of accuracy achieved in comparison to reference state-of-the-art models and operation values.

So, for future work some priority suggestions are left:

- Estimate and evaluate *rDCB* for the national network grid of GNSS receivers against direct calibration (when available);
- Estimate *rDCB* for other GPS frequencies/signals, L1C-L2C, L1-L5I, L1-L5Q, L1C-L5I and L1C-L5Q;
- Estimate *rDCB* values for other GNSS constellation (Galileo and BeiDou);
- Compare the *rDCB* differences between *IGS IAAC's rDCB* values.

While the follow up suggestions, in case the latter results provide additional proof for the results hereby achieved, namely:

- Application of the procedure at latitudes with higher complex ionospheric activity;
- Application of the procedure to the 11-year solar cycle maximum;
- Test carrier-phase measurements alone (fixed);

9. REFERENCES

Appleton, E.V., Barnett, M.A.F., 1925. Local reflection of wireless waves from the upper atmosphere. Nature 115, 333–334.

Appleton, E. V., Beynon, W.J.G., 1947. The application of ionospheric data to radio communications problems - Part II. Proc. Phys. Soc. 59, 58–76.

Aragon-angel, A., Commission, E., Agency, E.S., Pajares, M.H., 2015. Preliminary NeQuick assessment for future single frequency users of Galileo.

Arikan, F., Nayir, H., Sezen, U., Arikan, O., 2008. Estimation of single station interfrequency receiver bias using GPS-TEC. Radio Sci. 43, 1–13. https://doi.org/10.1029/2007RS003785

Bauer, S.J.., Lammer, H.., 2004. Planetary Aeronomy.

Bilitza, D., Altadill, D., Truhlik, V., Shubin, V., Galkin, I., Reinisch, B., Huang, X., 2017. International Reference Ionosphere 2016: From ionospheric climate to real-time weather predictions. Sp. Weather 15, 418–429. https://doi.org/10.1002/2016SW001593

Bilitza, D., McKinnell, L.A., Reinisch, B., Fuller-Rowell, T., 2011. The International Reference Ionosphere today and in the future. J. Geod. 85, 909–920. https://doi.org/10.1007/s00190-010-0427-x

Blewitt, G., 1990. An automatic editing algorithm for GPS data. Geophys. Res. Lett. 17, 199–202. https://doi.org/https://doi.org/10.1029/GL017i003p00199

Brunini, C., Azpilicueta, F.J., 2009. Accuracy assessment of the GPS-based slant total electron content. J. Geod. 83, 773–785. https://doi.org/10.1007/s00190-008-0296-8

Bust, G.S., Mitchell, C.N., 2008. History, current state, and future directions of ionospheric imaging. Rev. Geophys. 46, 1–23. https://doi.org/10.1029/2006RG000212

Ciraolo, L., Azpilicueta, F., Brunini, C., Meza, A., Radicella, S.M., 2007. Calibration errors on experimental slant total electron content (TEC) determined with GPS. J. Geod. 81, 111–120. https://doi.org/10.1007/s00190-006-0093-1

Dach, R., Lutz, S., Walser, P., Pierre Fridez, 2018. Bernese GNSS Software Version 5.2 Tutorial, Astronomical Institute, University of Bern. https://doi.org/10.7892/boris.72297

Dyrud, L., Jovancevic, A., Brown, A., Wilson, D., 2008. Ionospheric measurement with GPS : Receiver

techniques and methods 43, 1–11. https://doi.org/10.1029/2007RS003770

Elgered, G., Wickert, J., 2017. Monitoring of the Neutral Atmosphere, in: Teunissen, P.J.G., Montenbruck, O. (Eds.), Springer Handbook of Global Navigation Satellite Systems. Springer International Publishing, Cham, pp. 1109–1138. https://doi.org/10.1007/978-3-319-42928-1_38

ESA, S.W.S.N., 2021. Ionosphere Weather [WWW Document]. Ionos. Weather Expert Serv. Cent. URL https://swe.ssa.esa.int/ionospheric-weather (accessed 6.25.21).

Feltens, J., 2007. Development of a new three-dimensional mathematical ionosphere model at European Space Agency / European Space Operations Centre 5, 1–17. https://doi.org/10.1029/2006SW000294

GAL-OS-IONO, 2016. European GNSS (GALILEO) Open Service - Ionospheric Correction Algorithm for Galileo Single Frequency Users. https://doi.org/10.2873/685913

Georgiadou, P.Y., 1994. Modelling the ionosphere for an active control network of GPS stations, LGR - series : publications of the Delft Geodetic Computing Centre. Delft University of Technology, Netherlands.

Ghoddousi-Fard, R., Héroux, P., Danskin, D., Boteler, D., 2011. Developing a GPS TEC mapping service over Canada. Sp. Weather 9. https://doi.org/10.1029/2010SW000621

Giovanni, G. Di, Radicella, S.M., 1990. An analytical model of the electron density profile in the ionosphere 10, 27–30.

Hauschild, A., Montenbruck, O., 2016. A study on the dependency of GNSS pseudorange biases on correlator spacing. GPS Solut. 20, 159–171. https://doi.org/10.1007/s10291-014-0426-0

Heaviside, O., 1902. Telegraphy. Encycl. Br. IX 33, p.215.

Hernández-Pajares, M., Juan, J.M., Sanz, J., 1999. New approaches in global ionospheric determination using ground GPS data. J. Atmos. Solar-Terrestrial Phys. 61, 1237–1247. https://doi.org/10.1016/S1364-6826(99)00054-1

Hernández-Pajares, M., Juan, J.M., Sanz, J., Aragón-Àngel, À., García-Rigo, A., Salazar, D., Escudero, M., 2011. The ionosphere: Effects, GPS modeling and the benefits for space geodetic techniques. J. Geod. 85, 887–907. https://doi.org/10.1007/s00190-011-0508-5

Hernàndez-Pajares, M., Juan, J.M., Sanz, J., Garcia-Fernàndez, M., 2005. Towards a more realistic ionospheric mapping function. XXVIII URSI Gen. Assem. 2002, 2002–2005.

Hernández-Pajares, M., Juan, J.M., Sanz, J., Solé, J.G., 1998. Global observation of the ionospheric electronic response to solar events using ground and LEO GPS data. J. Geophys. Res. Sp. Phys. 103, 20789–20796. https://doi.org/https://doi.org/10.1029/98JA01272

Hobiger, T., Jakowski, N., 2017. Atmospheric Signal Propagation, in: Teunissen, P.J.G., Montenbruck, O. (Eds.), Springer Handbook of Global Navigation Satellite Systems. Springer International Publishing, Cham, pp. 165–193. https://doi.org/10.1007/978-3-319-42928-1_6

Hochegger, G., Nava, B., Radicella, S., Leitinger, R., 2000. A family of ionospheric models for different uses. Phys. Chem. Earth, Part C Solar, Terr. Planet. Sci. 25, 307–310. https://doi.org/10.1016/S1464-1917(00)00022-2

Hofmann-Wellenhof, B., Lichtenegger, H., Wasle, E., 2008. GNSS — Global Navigation Satellite Systems, 1st ed, Journal of Materials Processing Technology. Springer, Vienna. https://doi.org/https://doi.org/10.1007/978-3-211-73017-1

ICC, I.C.C., 2019. NAVSTAR GPS space segment / navigation user segment interfaces. GPS Directorate Space & Missile Systems Center (SMC) - LAAFB, United States.

Jin, S., Jin, R., Liu, X., 2019. GNSS Atmospheric Seismology, 1st ed, GNSS Atmospheric Seismology. Springer Singapore. https://doi.org/10.1007/978-981-10-3178-6

Kao, S., Tu, Y., Chen, W., Weng, D.J., Ji, S.Y., 2013. Factors affecting the estimation of GPS receiver instrumental biases. Surv. Rev. 45, 59–67. https://doi.org/10.1179/1752270612Y.0000000022

Kennelly, A.E., 1902. On the elevation of the electrically conducting strata of the earth's atmosphere. Elec. World Eng. 39, 473.

Klobuchar, J.A., 1987. Ionospheric time-delay algorithm for single-frequency GPS users. IEEE Trans. Aerosp. Electron. Syst. AES-23, 325–331. https://doi.org/10.1109/TAES.1987.310829

Komjathy, A., 1997. Global ionospheric total electron content mapping using the Global Positioning System. Engineering. University of New Brunswick, Fredericton, Canada.

Komjathy, A., Sparks, L., Wilson, B.D., Mannucci, A.J., 2005. Automated daily processing of more than 1000 ground-based GPS receivers for studying intense ionospheric storms. Radio Sci. 40. https://doi.org/10.1029/2005RS003279

Komjathy, A., Wilson, B.D., Runge, T.F., Boulat, B.M., Mannucci, A.J., Sparks, L., Reyes, M.J., 2002. A new ionospheric model for wide area differential GPS : The multiple shell approach. Proc. 2002

Natl. Tech. Meet. Inst. Navig. 460–466.

Langley, R.B., Teunissen, P.J.G., Montenbruck, O., 2017. Introduction to GNSS, in: Teunissen, P.J.G., Montenbruck, O. (Eds.), Springer Handbook of Global Navigation Satellite Systems. Springer International Publishing, Cham, pp. 3–23. https://doi.org/10.1007/978-3-319-42928-1_1

Lanyi, G.E., Roth, T., 1988. A comparison of mapped and measured total ionospheric electron content using global positioning system and beacon satellite observations. Radio Sci. 23, 483–492. https://doi.org/10.1029/RS023i004p00483

Leick, A., Rapoport, L., Tatarnikov, D., 2015. GPS Satellite Surveying, 4th ed. JohnWiley& Sons, Inc., Hoboken, New Jersey.

Li, B., Wang, M., Wang, Y., Guo, H., 2019. Model assessment of GNSS-based regional TEC modeling: polynomial, trigonometric series, spherical harmonic and multi-surface function. Acta Geod. Geophys. 54, 333–357. https://doi.org/10.1007/s40328-019-00262-8

Li, J., Huang, D., Zhao, Y., Hassan, A., 2021. Receiver DCB analysis and calibration in geomagnetic storm-time using IGS products. Surv. Rev. 53, 122–135. https://doi.org/10.1080/00396265.2019.1702369

Li, M., Yuan, Y., Wang, N., Li, Z., Liu, X., Zhang, X., 2018. Statistical comparison of various interpolation algorithms for reconstructing regional grid ionospheric maps over China. J. Atmos. Solar-Terrestrial Phys. 172, 129–137. https://doi.org/10.1016/j.jastp.2018.03.017

Li, Z., Yuan, Y., Wang, N., Hernandez-Pajares, M., Huo, X., 2015. SHPTS: towards a new method for generating precise global ionospheric TEC map based on spherical harmonic and generalized trigonometric series functions. J. Geod. 89, 331–345. https://doi.org/10.1007/s00190-014-0778-9

Liu, A., Li, Z., Wang, N., Yuan, C., Yuan, H., 2020. Analysis of the short-term temporal variation of differential code bias in GNSS receiver. Meas. J. Int. Meas. Confed. 153, 107448. https://doi.org/10.1016/j.measurement.2019.107448

Llewellyn, S., Bent, R., 1973. Documentation and description of the Bent ionospheric model. Tech. Rep. AFCRL-TR-73-0657. Air Force Cambridge Res. Lab., Hansom Air Force Base, Massachusetts.

Ma, G., Maruyama, T., 2003. Annales Geophysicae Derivation of TEC and estimation of instrumental biases from GEONET in Japan 2083–2093.

Mannucci, A.J., Iijima, B., Sparks, L., Pi, X., Wilson, B., Lindqwister, U., 1999. Assessment of global

TEC mapping using a three-dimensional electron density model. J. Atmos. Solar-Terrestrial Phys. 61, 1227–1236. https://doi.org/10.1016/S1364-6826(99)00053-X

Mannucci, A.J., Wilson, B.D., Yuan, D.N., Ho, C.H., Lindqwister, U.J., Runge, T.F., 1998. A global mapping technique for GPS-derived ionospheric total electron content measurements. Radio Sci. 33, 565–582. https://doi.org/10.1029/97RS02707

Materassi, M., Coster, A.J., Forte, B., Skone, S., 2020. The dynamical ionosphere: A systems approach to ionospheric irregularity, The Dynamical Ionosphere. https://doi.org/10.1016/C2017-0-01069-8

Mendillo, M., 2020. Chapter 1 - Introduction, in: Materassi, M., Forte, B., Coster, A.J., Skone, S. (Eds.), The Dynamical Ionosphere. Elsevier, pp. 3–6. https://doi.org/https://doi.org/10.1016/B978-0-12-814782-5.00001-7

Montenbruck, O., Hauschild, A., Steigenberger, P., 2014. Differential Code Bias Estimation using Multi-GNSS Observations and Global Ionosphere Maps. Navig. J. Inst. Navig. 61, 191–201. https://doi.org/10.1002/navi.64

Nava, B., Coïsson, P., Radicella, S.M., 2008. A new version of the NeQuick ionosphere electron density model. J. Atmos. Solar-Terrestrial Phys. 70, 1856–1862. https://doi.org/10.1016/j.jastp.2008.01.015

Nie, W., Xu, T., Rovira-Garcia, A., Juan Zornoza, J.M., Sanz Subirana, J., González-Casado, G., Chen, W., Xu, G., 2018. Revisit the calibration errors on experimental slant total electron content (TEC) determined with GPS. GPS Solut. 22, 1–11. https://doi.org/10.1007/s10291-018-0753-7

NOAA, 2021. Solar cycle progression [WWW Document]. Sp. Weather Predict. Cent. URL https://www.swpc.noaa.gov/products/solar-cycle-progression (accessed 6.25.21).

Radicella, S., Nava, B., Coïsson, P., 2008. Ionospheric models for GNSS single frequency range delay corrections. Física la Tierra 20, 27–39. https://doi.org/10.5209/rev_FITE.2008.v20.12311

Radicella, S.M., Leitinger, R., 2001. The evolution of the DGR approach to model electron density profiles. Adv. Sp. Res. 27, 35–40. https://doi.org/10.1016/S0273-1177(00)00138-1

Radicella, S.M., Nava, B., 2020. Chapter 6 - Empirical ionospheric models, in: Materassi, M., Forte, B., Coster, A.J., Skone, S. (Eds.), The Dynamical Ionosphere. Elsevier, pp. 39–53. https://doi.org/https://doi.org/10.1016/B978-0-12-814782-5.00006-6

Radicella, S.M., Radicella, S.M., Zhang, M.L., 1995. The improved DGR analytical model of electron

density height profile and total electron content in the ionosphere. Ann. Geophys. 38. https://doi.org/10.4401/ag-4130

Rawer, K., 1963. Propagation of decameter waves (HF-band), Landmark. ed, Meteorological and Astronomical Inuences on Radio Wave Propagation. Pergamon Press, B., New York.

Rawer, K., Bilitza, D., Ramakrishnan, S., 1978. Goals and status of the International Reference Ionosphere. Rev. Geophys. 16, 177–181. https://doi.org/10.1029/RG016i002p00177

Rius, A., Ruffini, G., Cucurull, L., 1997. Improving the vertical resolution of ionospheric tomography with GPS occultations. Geophys. Res. Lett. 24, 2291–2294. https://doi.org/10.1029/97GL52283

Roma-Dollase, D., Hernández-Pajares, M., Krankowski, A., Kotulak, K., Ghoddousi-Fard, R., Yuan, Y., Li, Z., Zhang, H., Shi, C., Wang, C., Feltens, J., Vergados, P., Komjathy, A., Schaer, S., García-Rigo, A., Gómez-Cama, J.M., 2018. Consistency of seven different GNSS global ionospheric mapping techniques during one solar cycle. J. Geod. 92, 691–706. https://doi.org/10.1007/s00190-017-1088-9

Rovira-Garcia, A., Juan, J.M., Sanz, J., González-Casado, G., Ibáñez, D., 2016. Accuracy of ionospheric models used in GNSS and SBAS: methodology and analysis. J. Geod. 90, 229–240. https://doi.org/10.1007/s00190-015-0868-3

Sanz, J., Miguel Juan, J., Rovira-Garcia, A., González-Casado, G., 2017. GPS differential code biases determination: methodology and analysis. GPS Solut. 21, 1549–1561. https://doi.org/10.1007/s10291-017-0634-5

Schaer, S., 1999. Mapping and predicting the earth's ionosphere using the Global Positioning System. Diss. Astron. Inst. 205.

Subirana, J., Zornoza, J., Hernández-Pajares, M., 2013. GNNS Data Processing - Volume I: Fundamentals and algorithms. European Space Agency.

Teunissen;, P.J.G., Montenbruck, O., 2017. Springer Handbook of Global Navigation Satellite Systems. Springer International Publishing. https://doi.org/10.1007/978-3-319-42928-1

VectorNav, 2021. Inertial Navigation Primer [WWW Document]. Educ. Mater. https://doi.org/10.1017/s036839310007067x

Villiger, A., Schaer, S., Dach, R., Prange, L., Sušnik, A., Jäggi, A., 2019. Determination of GNSS pseudo-absolute code biases and their long-term combination. J. Geod. 93, 1487–1500.

https://doi.org/10.1007/s00190-019-01262-w

Wielgosz, P., Milanowska, B., Krypiak-Gregorczyk, A., Jarmołowski, W., 2021. Validation of GNSS-derived global ionosphere maps for different solar activity levels: case studies for years 2014 and 2018. GPS Solut. 25, 1–15. https://doi.org/10.1007/s10291-021-01142-x

Yasyukevich, Y. V., Mylnikova, A.A., Kunitsyn, V.E., Padokhin, A.M., 2015. Influence of GPS/GLONASS differential code biases on the determination accuracy of the absolute total electron content in the ionosphere. Geomagn. Aeron. 55, 763–769. https://doi.org/10.1134/S001679321506016X

Yuan, Y., Ou, J., 2004. Generalized trigonometric series function model for determining ionospheric delay. Prog. Nat. Sci. 14, 1010–1014. https://doi.org/10.1080/10020070412331344711

Zhang, H., Xu, P., Han, W., Ge, M., Shi, C., 2013. Eliminating negative VTEC in global ionosphere maps using inequality-constrained least squares. Adv. Sp. Res. 51, 988–1000. https://doi.org/10.1016/j.asr.2012.06.026

10. APPENDIX – TERCEIRA GROUND STATION RESULTS – AÇORES

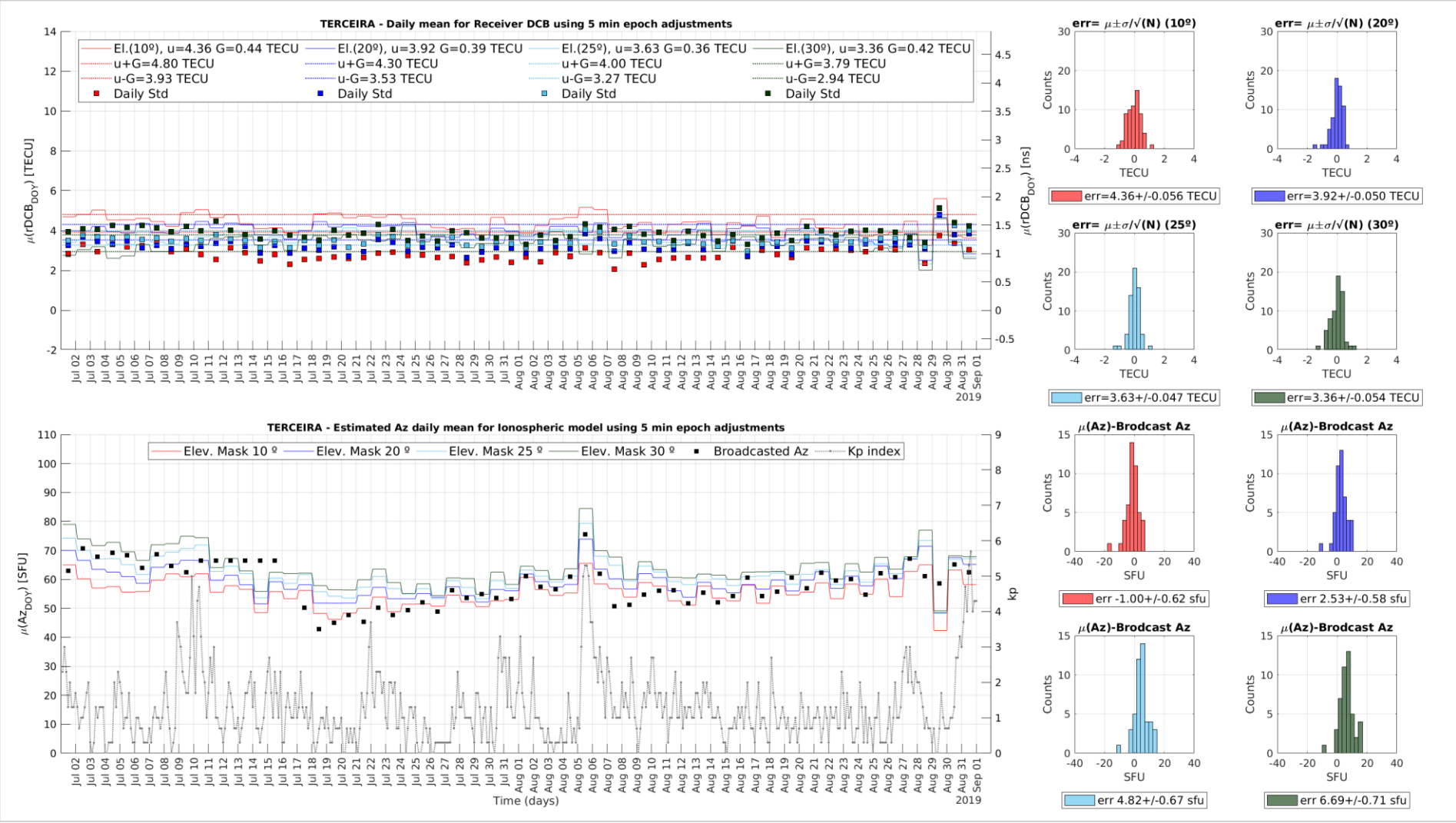

Terceira day-to-day results for the $\min[\chi^2(t)]$ adjustment procedure (using single 5 minute epochs) with identical description for the plots meaning, according to Fig. 37.

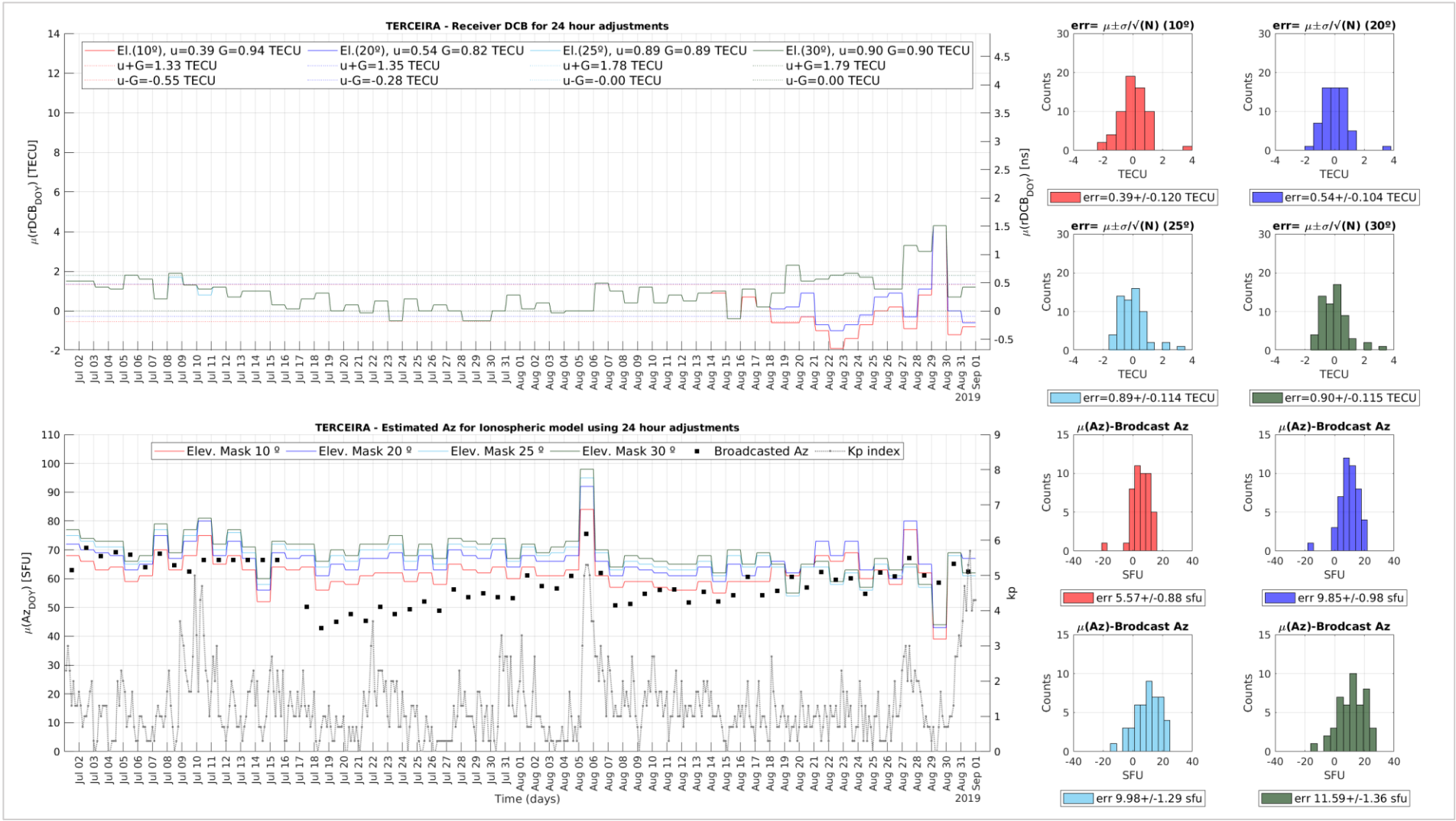

Terceira day-to-day results for the $\min[\chi^2(t)]$ adjustment procedure (using the 24 hour sum of epochs) with identical description for the plots meaning, according to Fig. 37.

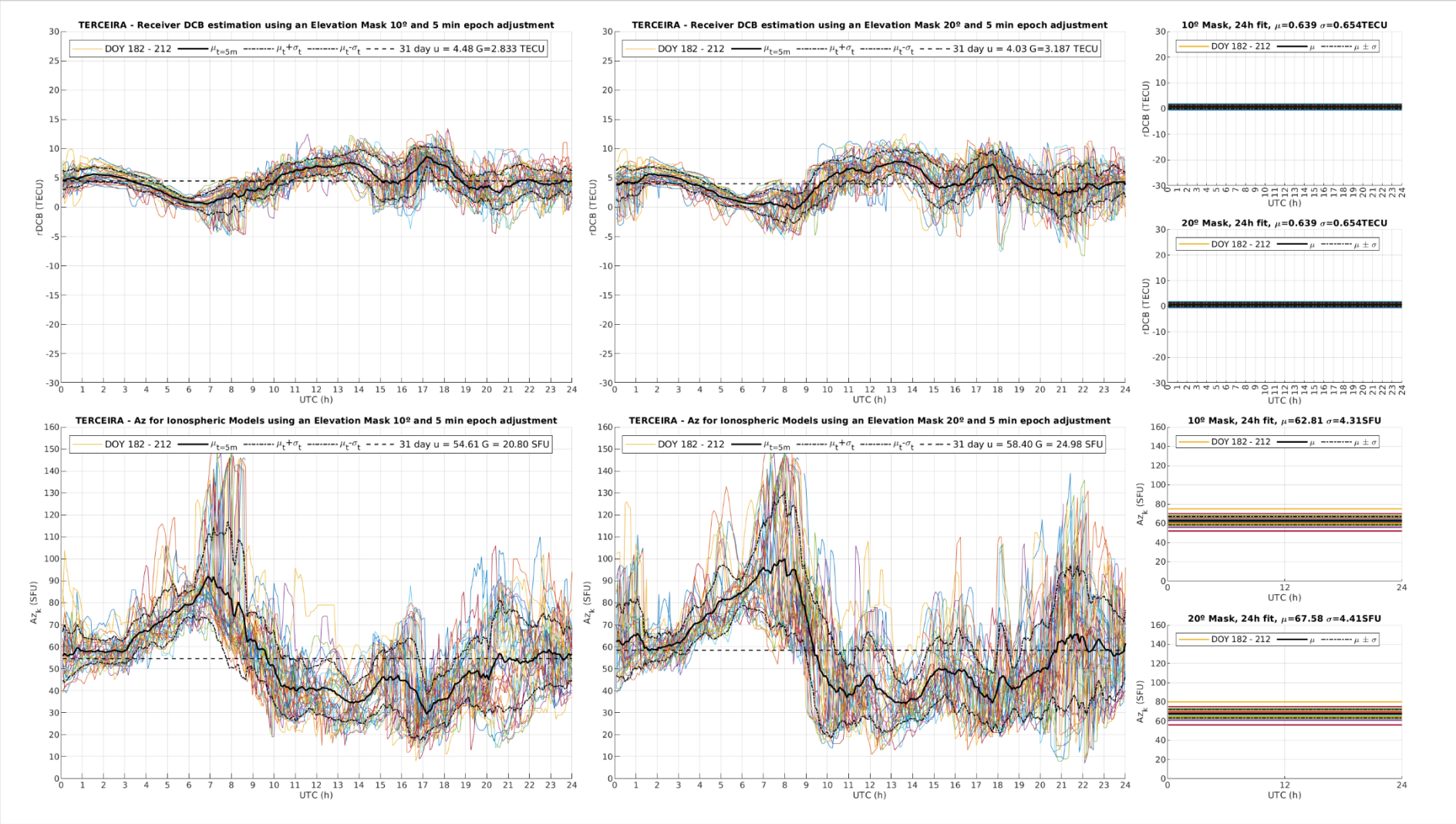

TERCEIRA Receiver *DCB* and *Az* intra-day variation values, using a 5 min epoch $\min[\chi^2(t)]$ adjustment procedure, in comparison with the 24 hr adjustment, for the time-series ranging from DOY182 to 212 of 2019 and elevation masks of 10 and 20º.

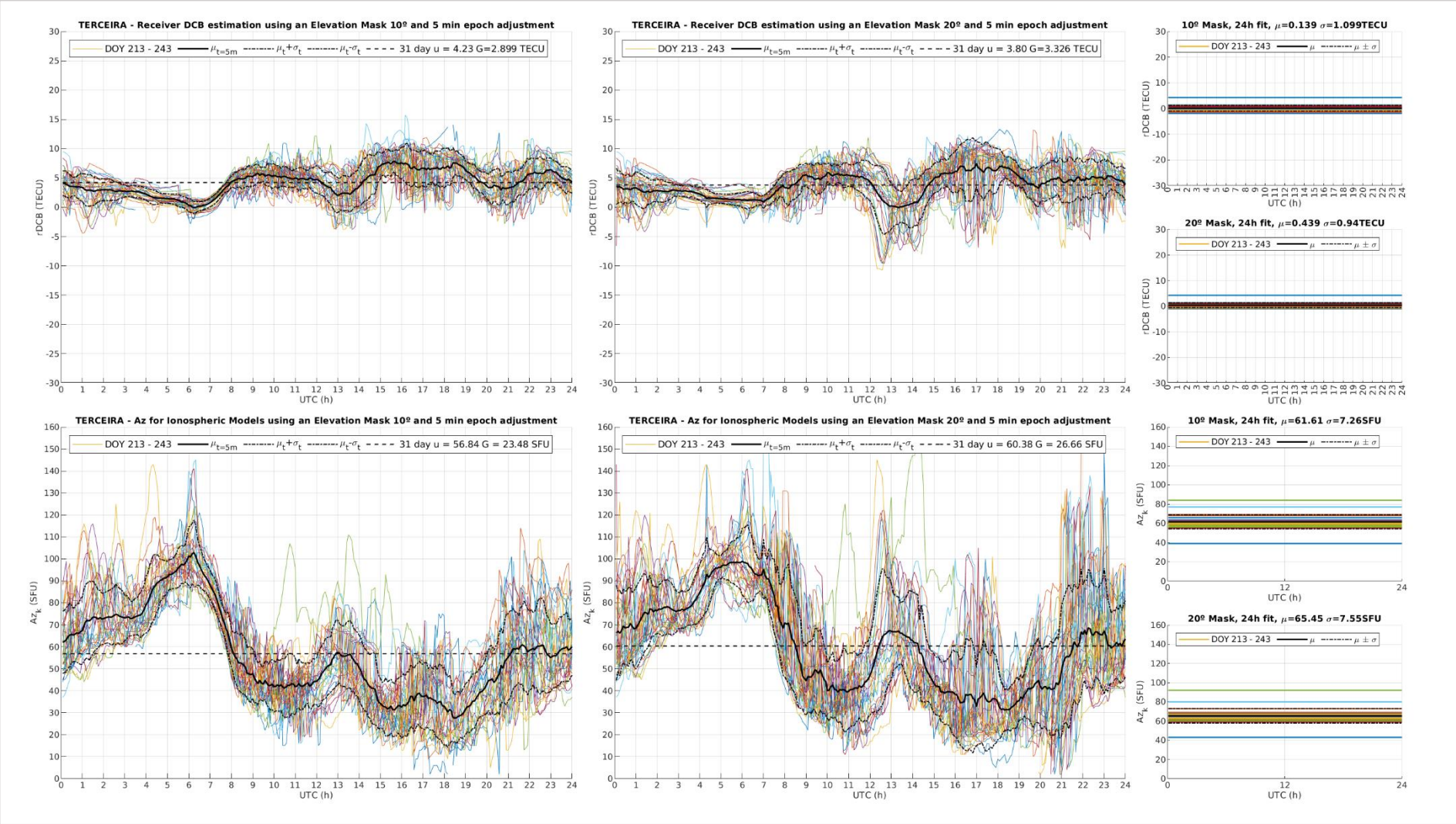

TERCEIRA Receiver *DCB* and *Az* intra-day variation values, using a 5 min epoch $\min[\chi^2(t)]$ adjustment procedure, in comparison with the 24 hr adjustment, for the time-series ranging from DOY 213 to 243 of 2019 and elevation masks of 10 and 20º.

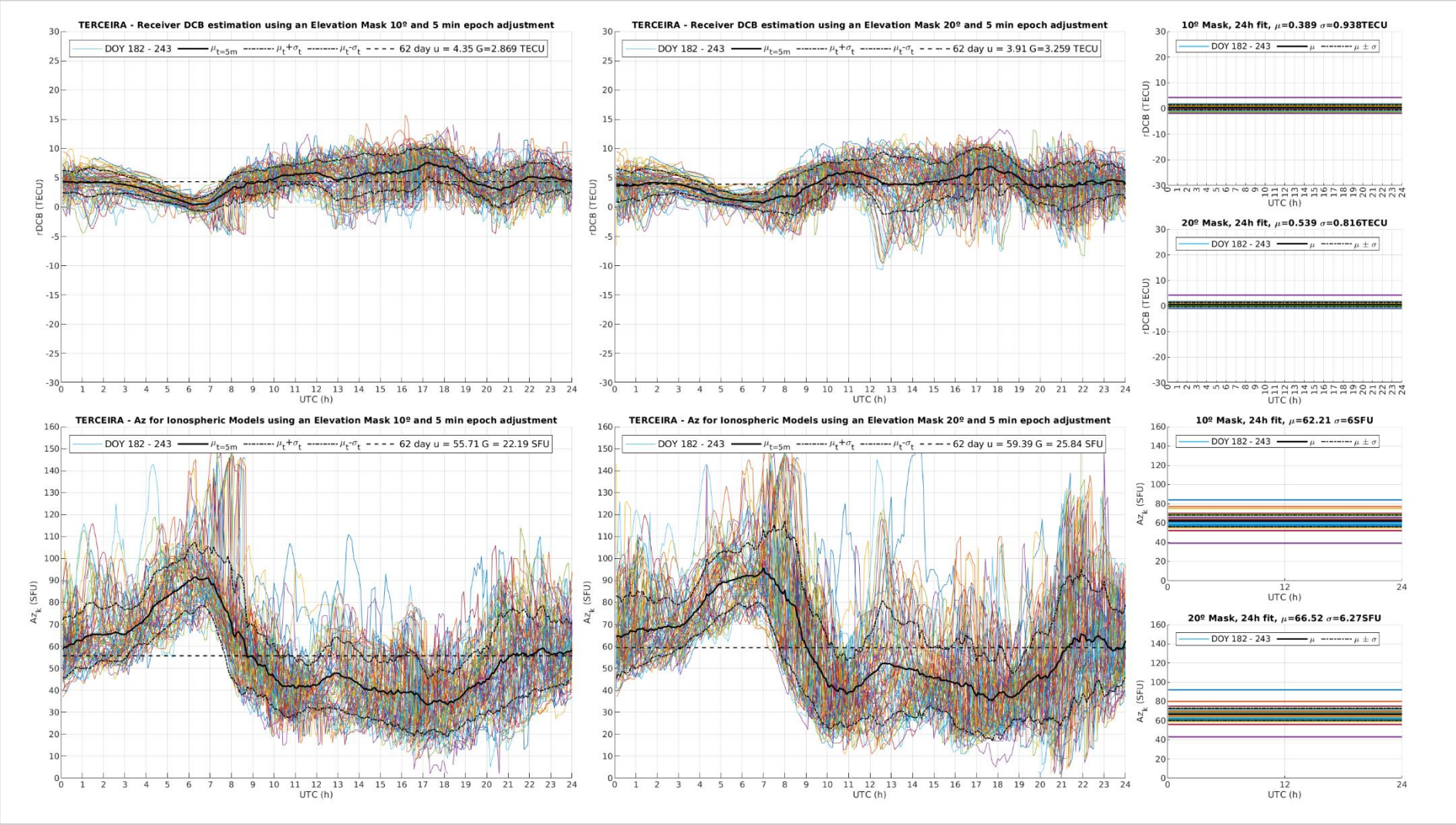

TERCEIRA Receiver *DCB* and *Az* intra-day variation values, using a 5 min epoch $\min[\chi^2(t)]$ adjustment procedure, in comparison with the 24 hr adjustment, for the time-series ranging from DOY182 to 243 of 2019 and elevation masks of 10 and 20º.

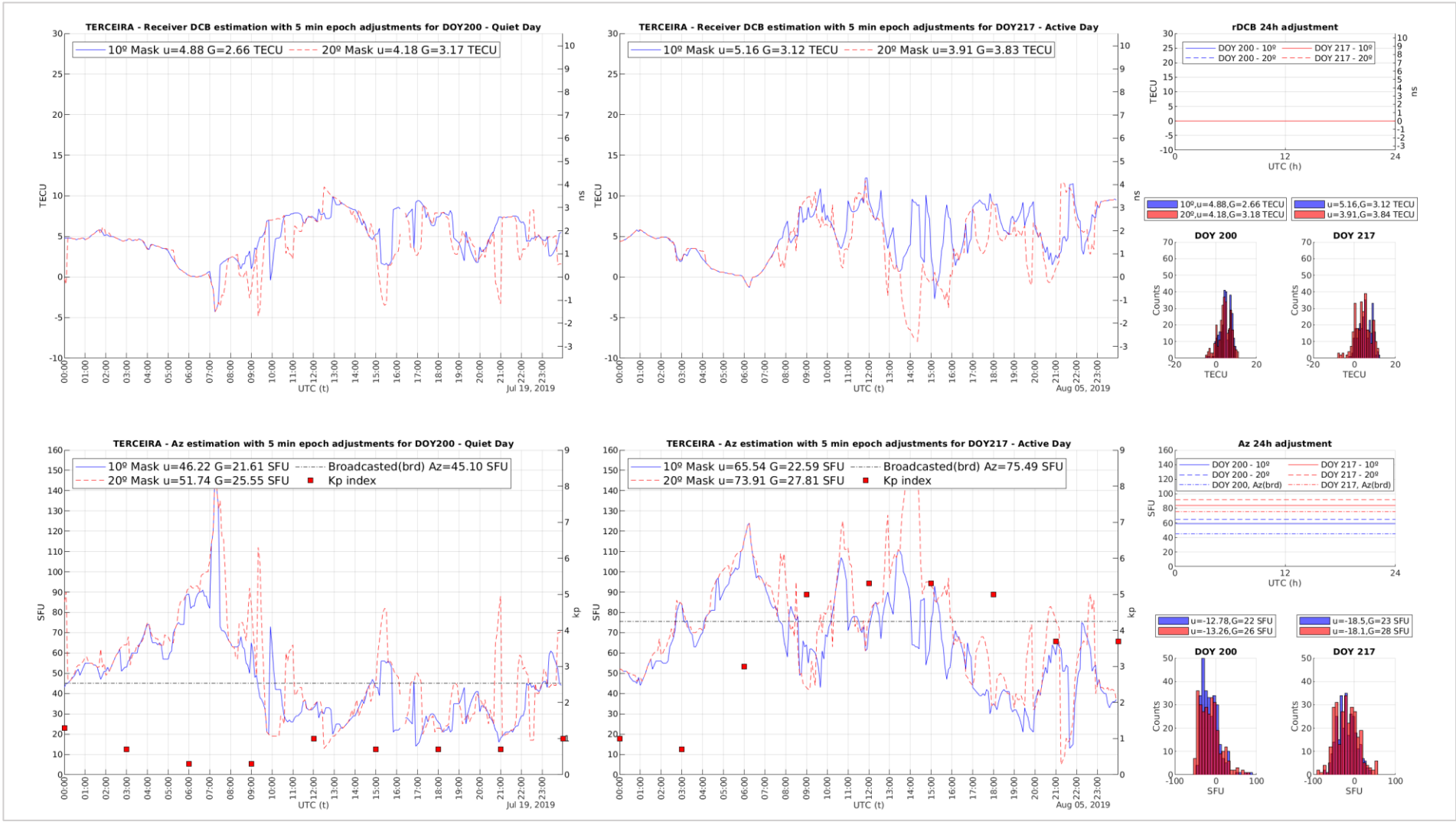

TERCEIRA Receiver DCB and Az results for the 5 min epoch $\min[\chi^2(t)]$ adjustment during a quiet day DOY 200 – July 19th of 2019 (1st tile column) and an active day DOY 217 – August 5th of 2019 (2nd tile column). Receiver DCB and Az results for the 24 hr $\min[\chi^2(t)]$ adjustment for the same DOY's(3rd tile column). Histograms with 5 min epoch difference against 24hr rDCB estimation for the respective DOY (3rd column top). Histograms with 5 min epoch difference against 24hr Az estimation for the respective DOY (3rd column bottom).

11. APPENDIX – FLORES GROUND STATION RESULTS – AÇORES

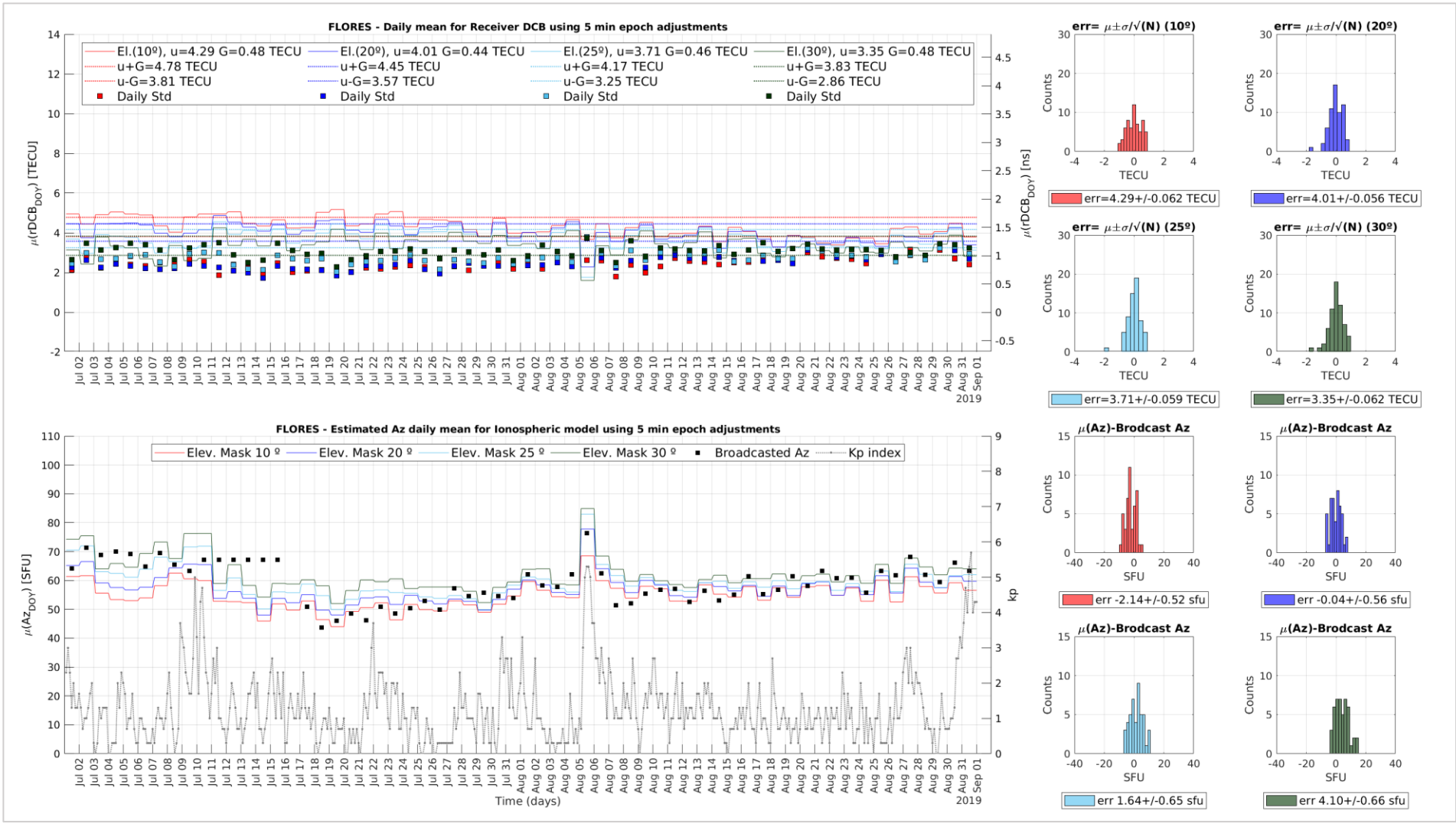

Flores day-to-day results for the $\min[\chi^2(t)]$ adjustment procedure (using single 5 minute epochs) with identical description for the plots meaning, according to Fig. 37.

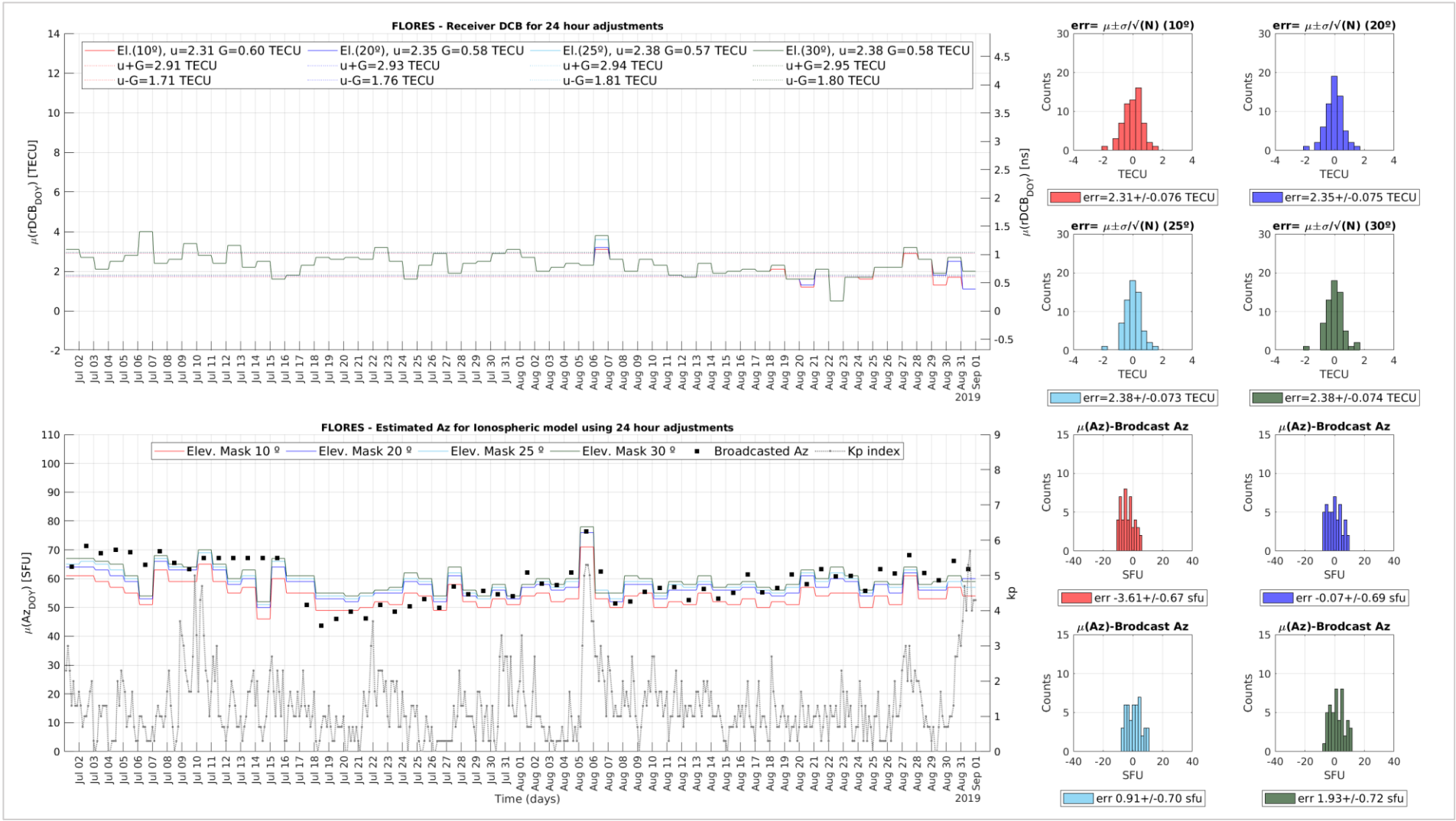

Flores day-to-day results for the $\min[\chi^2(t)]$ adjustment procedure (using the 24 hour sum of epochs) with identical description for the plots meaning, according to Fig. 37.

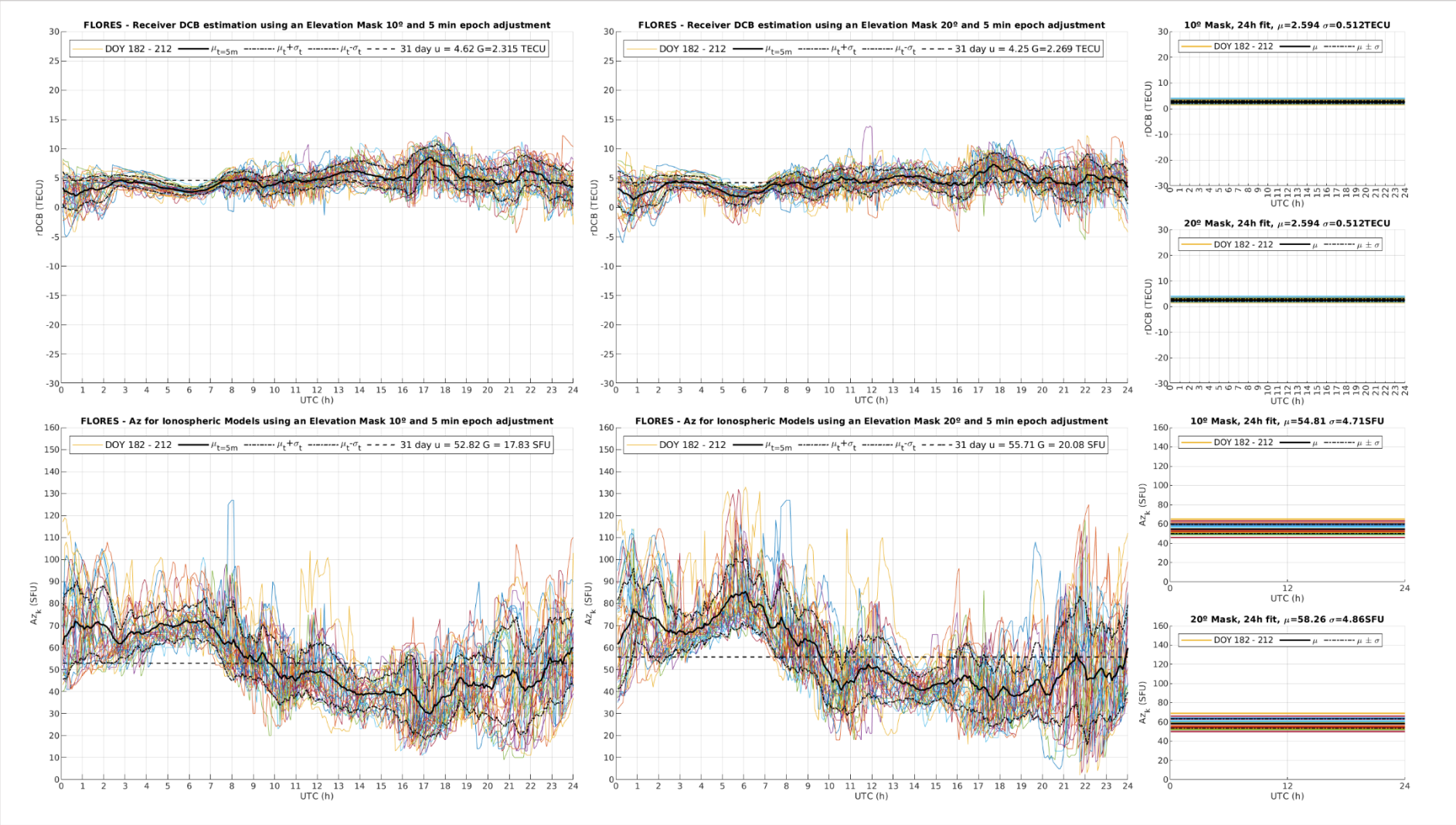

FLORES Receiver *DCB* and *Az* intra-day variation values, using a 5 min epoch $\min[\chi^2(t)]$ adjustment procedure, in comparison with the 24 hr adjustment, for the time-series ranging from DOY182 to 212 of 2019 and elevation masks of 10 and 20º.

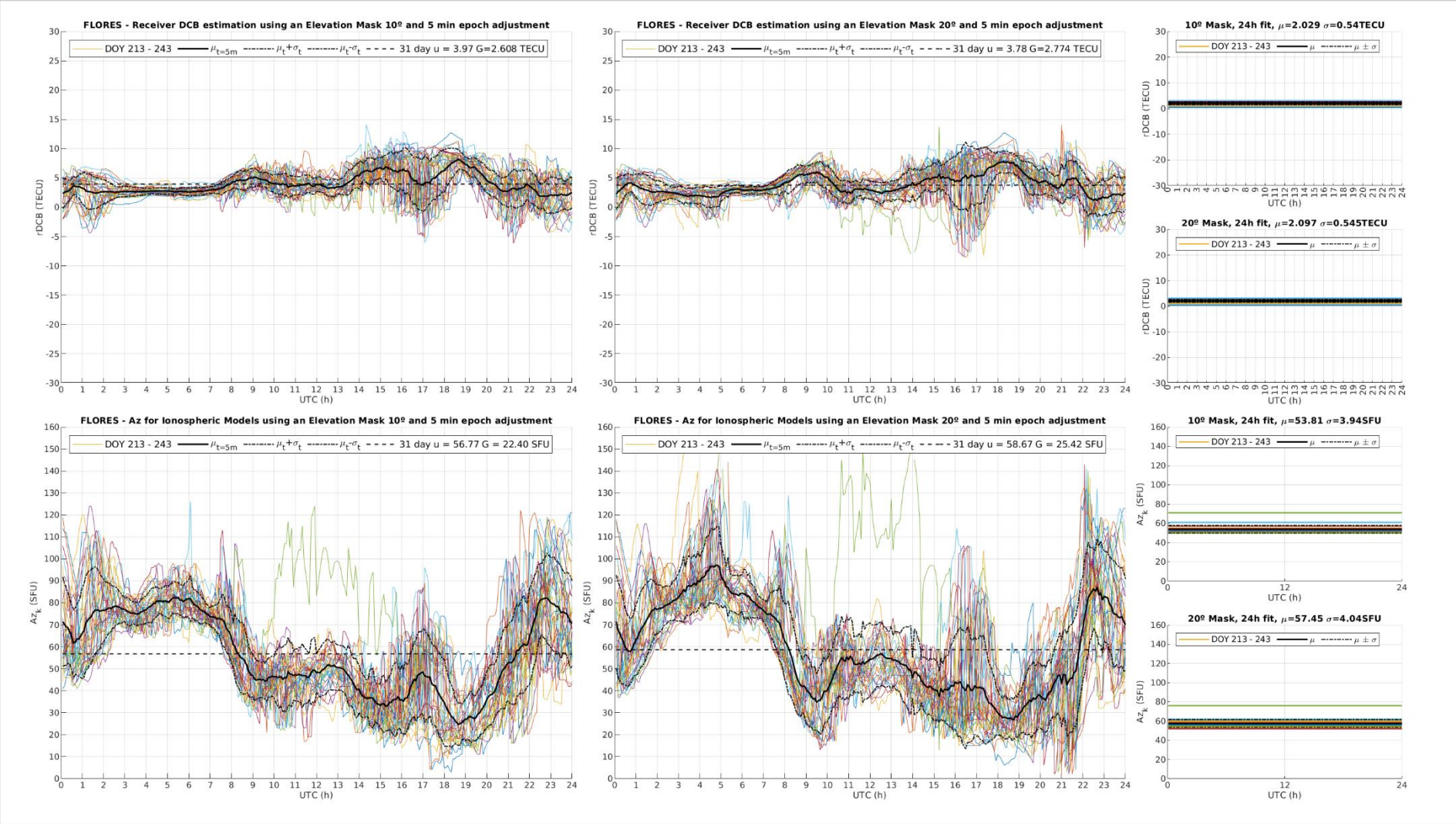

FLORES Receiver *DCB* and *Az* intra-day variation values, using a 5 min epoch $\min[\chi^2(t)]$ adjustment procedure, in comparison with the 24 hr adjustment, for the time-series ranging from DOY 213 to 243 of 2019 and elevation masks of 10 and 20º.

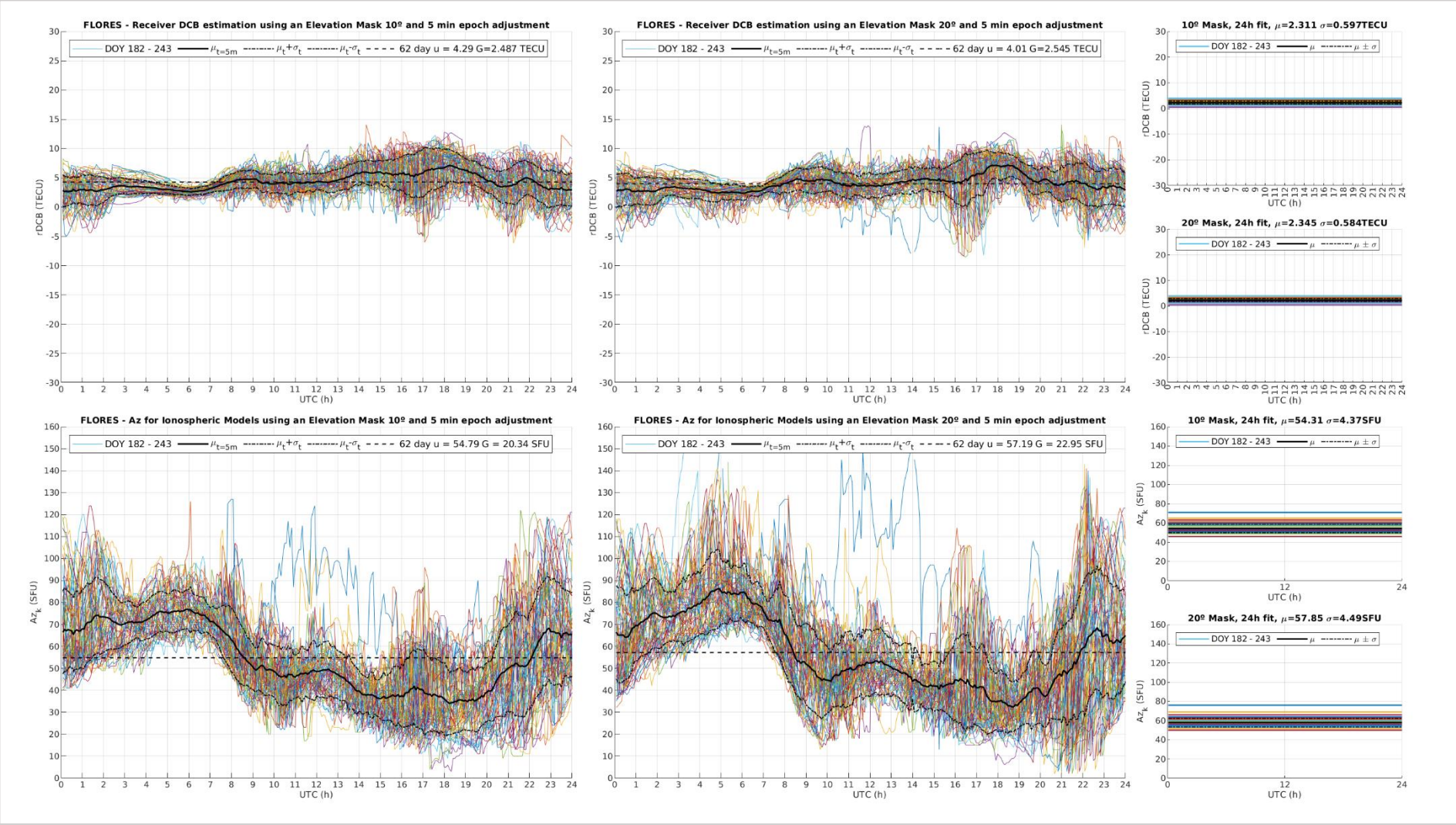

FLORES Receiver *DCB* and *Az* intra-day variation values, using a 5 min epoch $\min[\chi^2(t)]$ adjustment procedure, in comparison with the 24 hr adjustment, for the time-series ranging from DOY182 to 243 of 2019 and elevation masks of 10 and 20º.

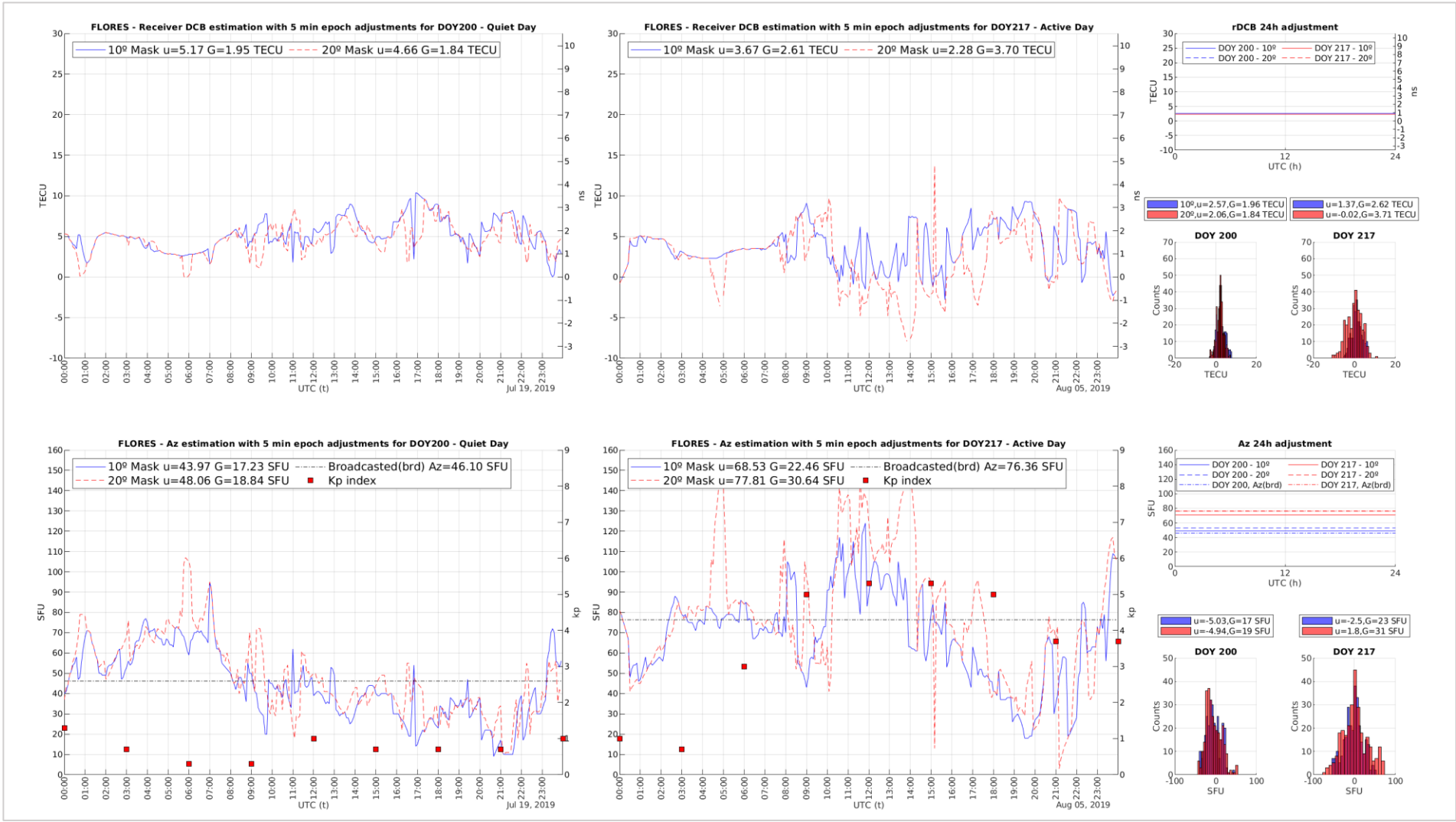

FLORES Receiver DCB and Az results for the 5 min epoch $\min[\chi^2(t)]$ adjustment during a quiet day DOY 200 – July 19th of 2019 (1st tile column) and an active day DOY 217 – August 5th of 2019 (2nd tile column). Receiver DCB and Az results for the 24 hr $\min[\chi^2(t)]$ adjustment for the same DOY's(3rd tile column). Histograms with 5 min epoch difference against 24hr rDCB estimation for the respective DOY (3rd column top). Histograms with 5 min epoch difference against 24hr Az estimation for the respective DOY (3rd column bottom).

12. APPENDIX – FUNCHAL GROUND STATION RESULTS – MADEIRA

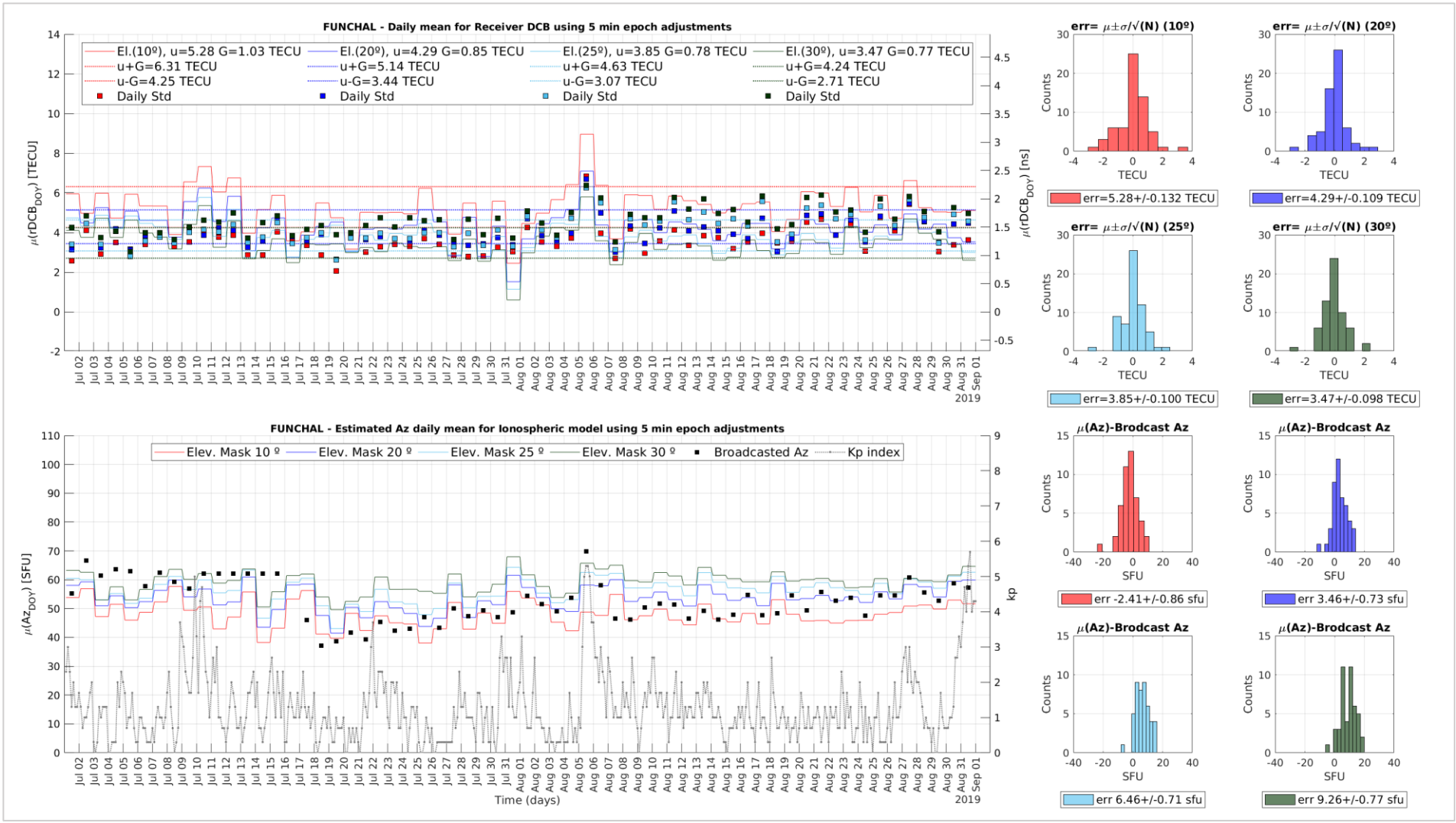

Funchal day-to-day results for the $\min[\chi^2(t)]$ adjustment procedure (using single 5 minute epochs) with identical description for the plots meaning, according to Fig. 37.

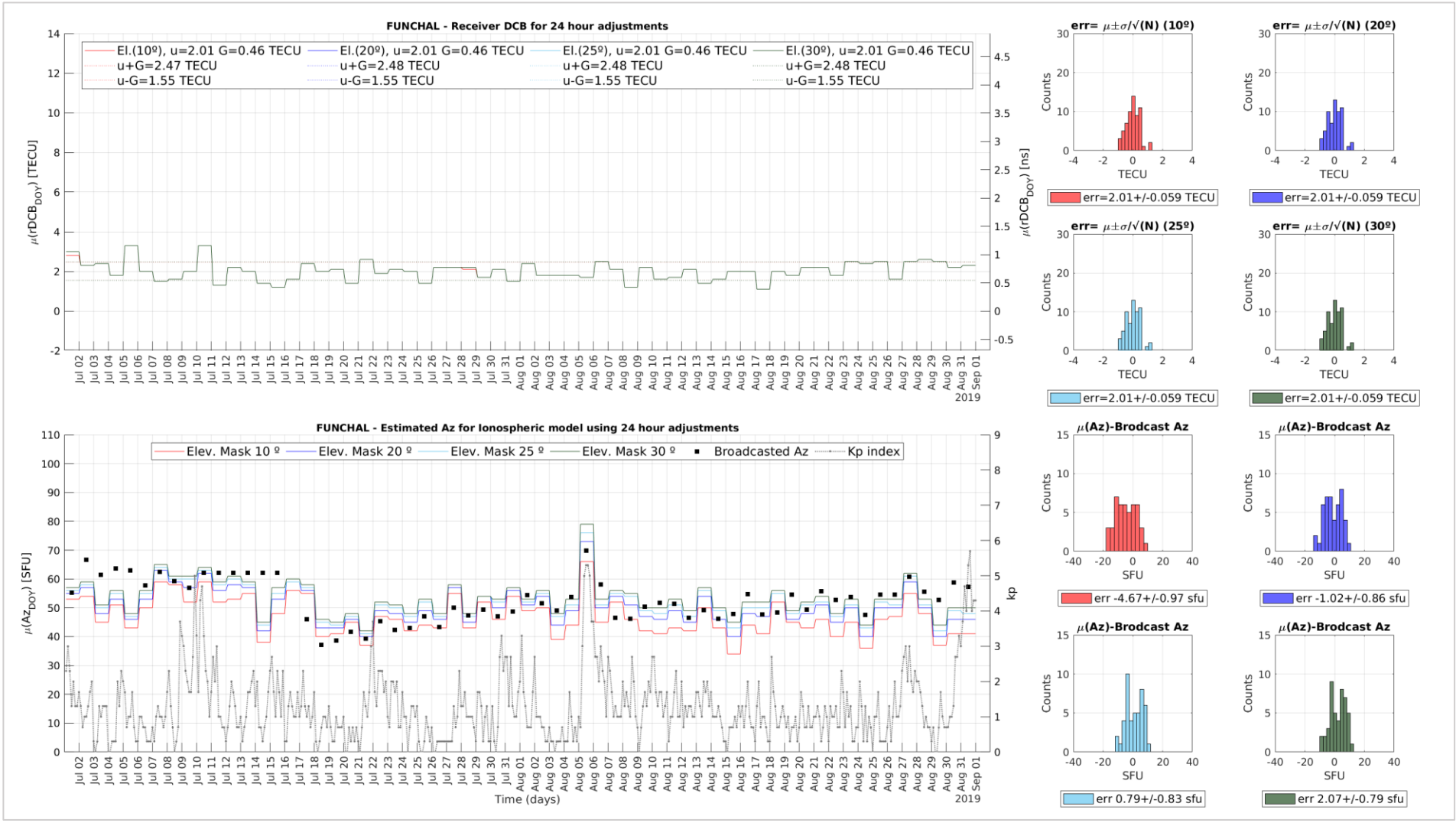

Funchal day-to-day results for the $\min[\chi^2(t)]$ adjustment procedure (using the 24 hour sum of epochs) with identical description for the plots meaning, according to Fig. 37.

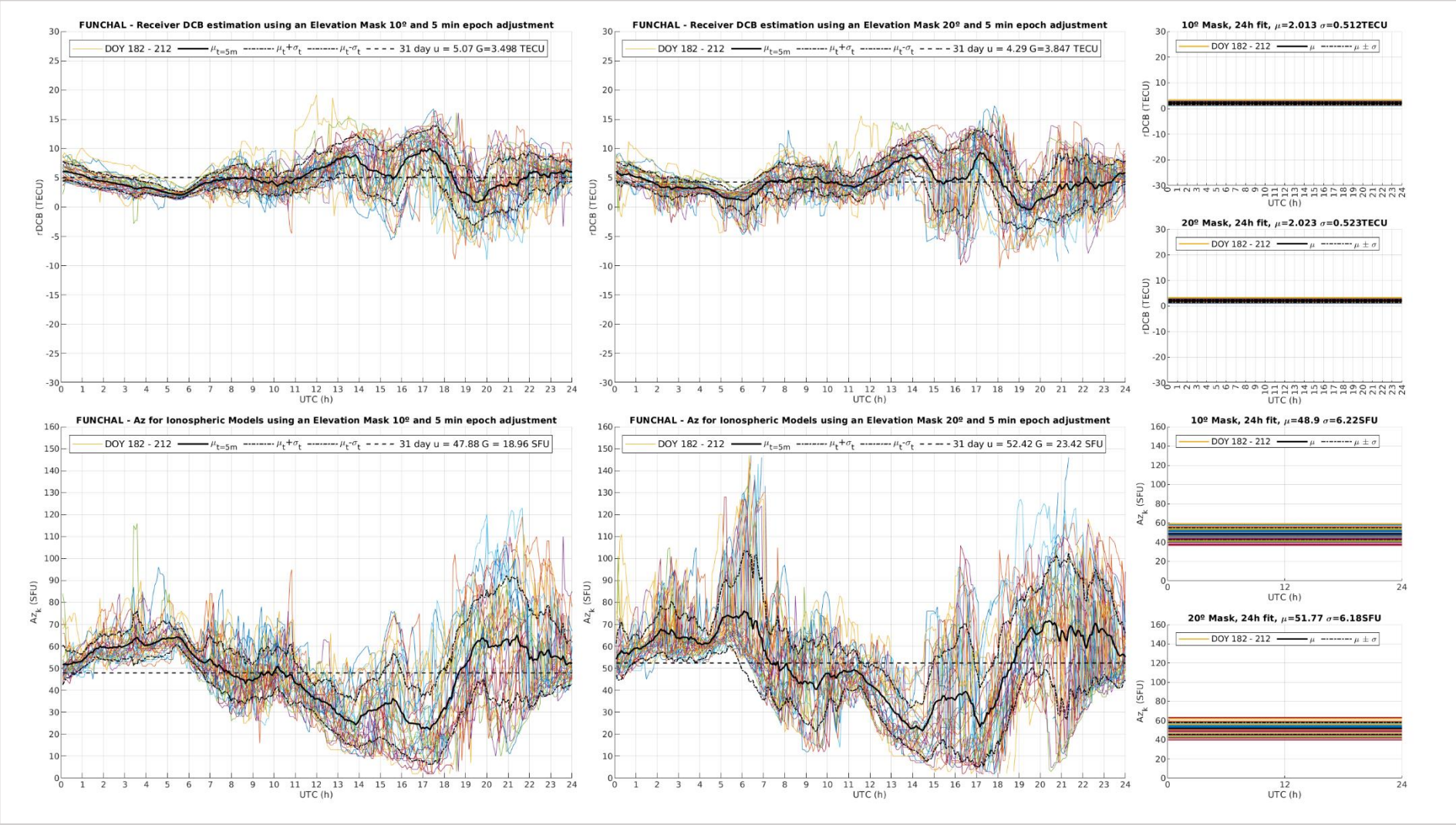

FUNCHAL Receiver *DCB* and *Az* intra-day variation values, using a 5 min epoch $\min[\chi^2(t)]$ adjustment procedure, in comparison with the 24 hr adjustment, for the time-series ranging from DOY182 to 212 of 2019 and elevation masks of 10 and 20º.

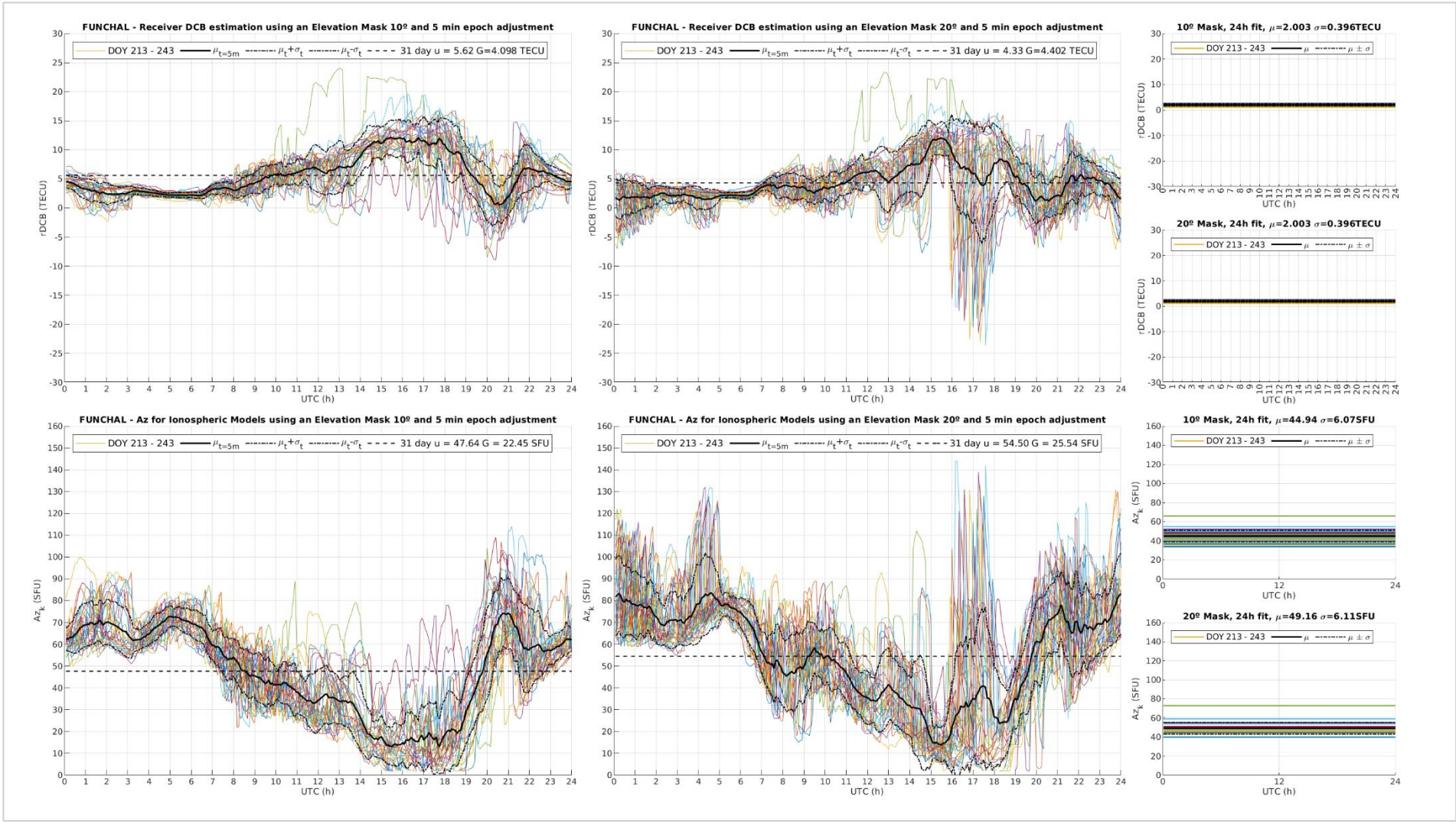

FUNCHAL Receiver *DCB* and *Az* intra-day variation values, using a 5 min epoch $\min[\chi^2(t)]$ adjustment procedure, in comparison with the 24 hr adjustment, for the time-series ranging from DOY 213 to 243 of 2019 and elevation masks of 10 and 20º.

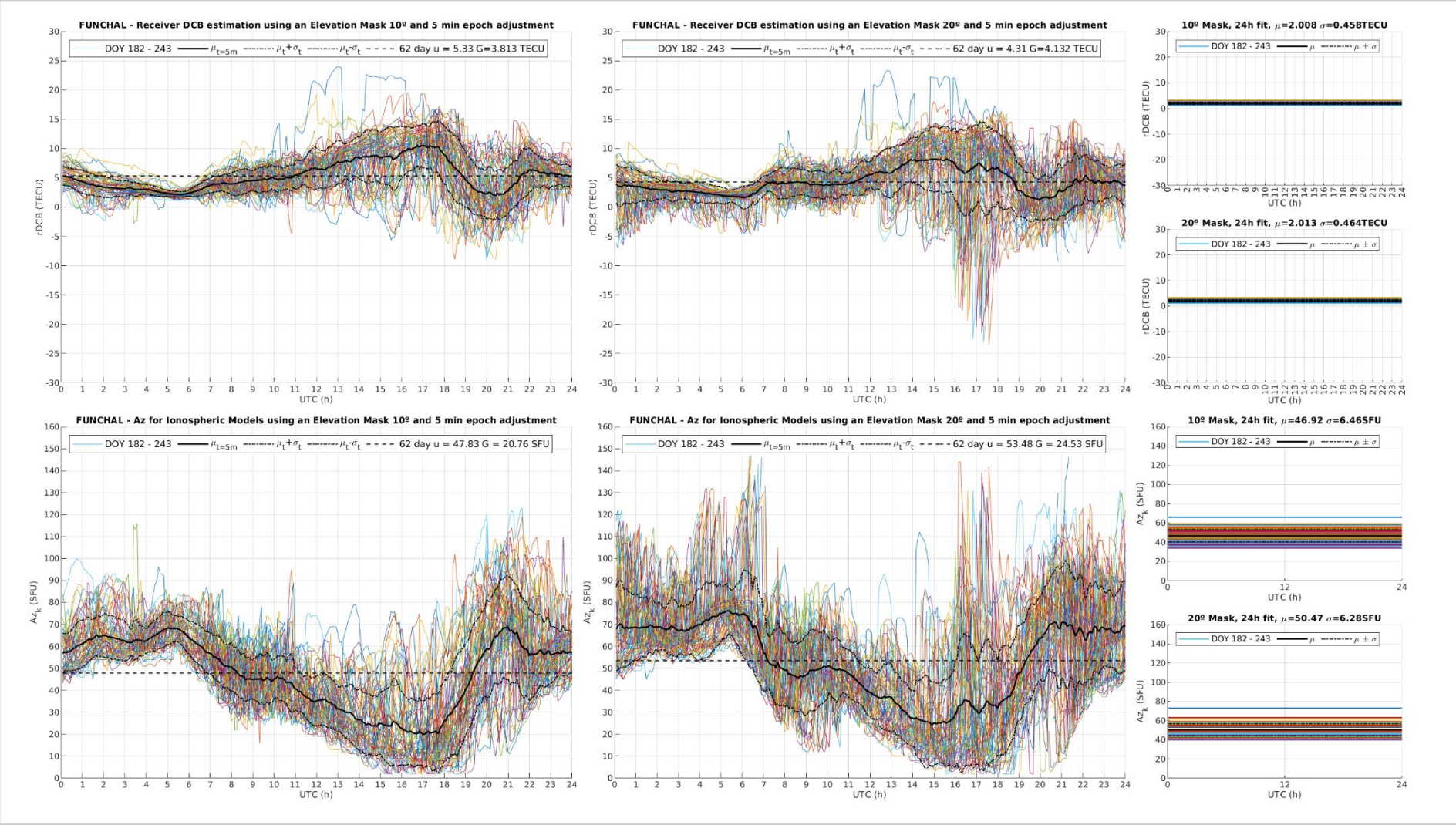

FUNCHAL Receiver *DCB* and *Az* intra-day variation values, using a 5 min epoch $\min[\chi^2(t)]$ adjustment procedure, in comparison with the 24 hr adjustment, for the time-series ranging from DOY182 to 243 of 2019 and elevation masks of 10 and 20º.

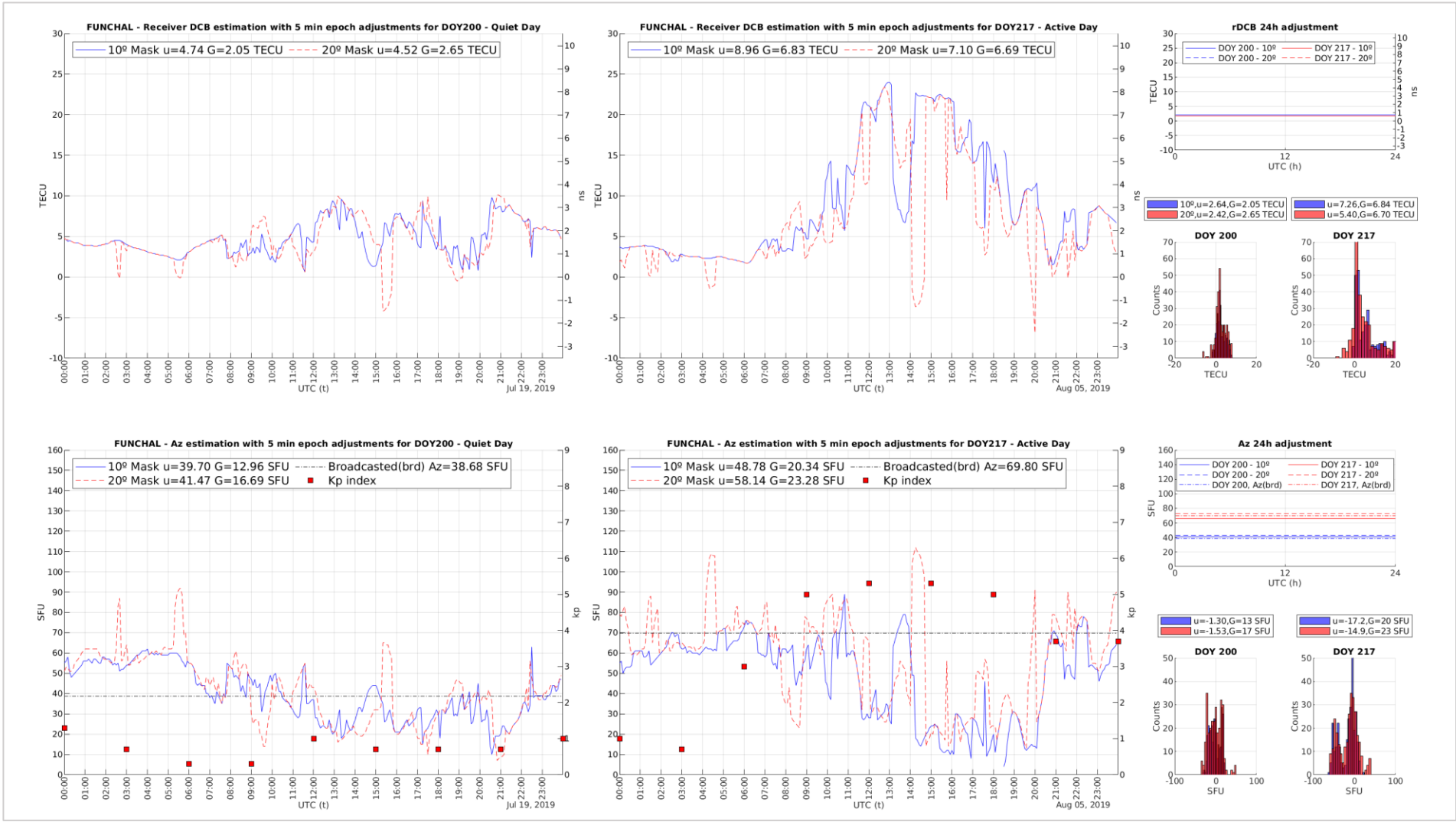

FUNCHAL Receiver DCB and Az results for the 5 min epoch $\min[\chi^2(t)]$ adjustment during a quiet day DOY 200 – July 19th of 2019 (1st tile column) and an active day DOY 217 – August 5th of 2019 (2nd tile column). Receiver DCB and Az results for the 24 hr $\min[\chi^2(t)]$ adjustment for the same DOY's(3rd tile column). Histograms with 5 min epoch difference against 24hr rDCB estimation for the respective DOY (3rd column top). Histograms with 5 min epoch difference against 24hr Az estimation for the respective DOY (3rd column bottom).